Dissertations and Theses

10-2012

Development of a Supervisory Control Unit for a Series Plug-in Hybrid Electric Vehicle

Brian Neal Harries
Embry-Riddle Aeronautical University - Daytona Beach

Follow this and additional works at: https://commons.erau.edu/edt

Part of the Automotive Engineering Commons, and the Mechanical Engineering Commons

DEVELOPMENT OF A SUPERVISORY CONTROL UNIT FOR A SERIES PLUG-IN

HYBRID ELECTRIC VEHICLE

By

Brian Neal Harries

A Thesis Submitted to the College of Engineering Department of Mechanical
Engineering in Partial Fulfillment of the Requirements for the Degree of
Master of Science in Mechanical Engineering

Embry-Riddle Aeronautical University
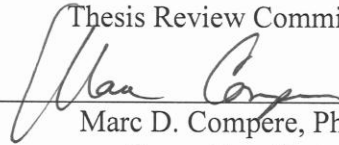
Daytona Beach, Florida

October 2012

DEVELOPMENT OF A SUPERVISORY CONTROL UNIT FOR A SERIES PLUG-IN
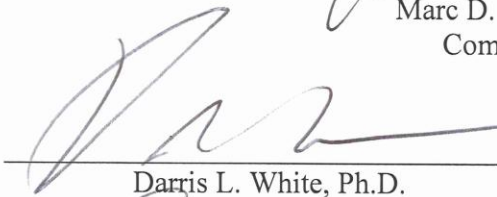HYBRID ELECTRIC VEHICLE

by

Brian Neal Harries

This thesis was prepared under the direction of the candidate's Thesis Committee Chair,
Dr. Marc D. Compere, Assistant Professor, Daytona Beach Campus, and Thesis
Committee Members Dr. Darris L., White, Professor, Daytona Beach Campus,
and Dr. Yan Tang, Assistant Professor, Daytona Beach Campus, and
has been approved by the Thesis Committee. It was submitted to the
Department of Mechanical Engineering in partial
fulfillment of the requirements for the degree of
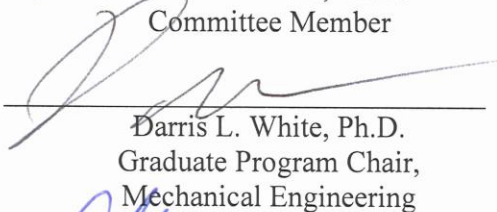Master of Science in Mechanical Engineering

Thesis Review Committee:

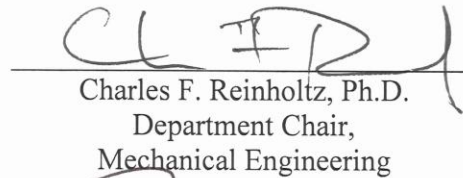_____
Marc D. Compere, Ph.D.
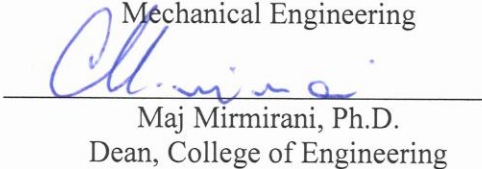Committee Chair

_____   _____
Darris L. White, Ph.D.   Yan Tang, Ph.D.
Committee Member   Committee Member
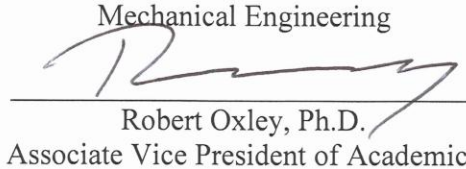
_____   _____
Darris L. White, Ph.D.   Charles F. Reinholtz, Ph.D.
Graduate Program Chair,   Department Chair,
Mechanical Engineering   Mechanical Engineering

_____   _____
Maj Mirmirani, Ph.D.   Robert Oxley, Ph.D.
Dean, College of Engineering   Associate Vice President of Academics

                                                                        12-11-12
                                                                  _____
                                                                        Date

iii

Acknowledgements

Acknowledgements

Abstract

Researcher: Brian Neal Harries

Title: Development of a supervisory control unit for a series plug-in hybrid electric vehicle

Institution: Embry-Riddle Aeronautical University

Degree: Master of Science in Mechanical Engineering

Year: 2012

A Series PHEV was chosen, as ERAU's entry into EcoCAR2 through a multidisciplinary architecture selection process. The series architecture was chosen for its mechanical feasibility, consumer acceptability and its performance on energy consumption simulations. The Series PHEV architecture was modeled using Matlab, Simulink, and dSPACE ASM tools, to create a plant model for controller development. A supervisory controller was developed to safely control the interactions between powertrain components. The supervisory control unit was tested using SIL and HIL methodologies. The supervisory controller was developed with an emphasis on fault detection and mitigation for safety critical systems. A power management control algorithm was developed to efficiently control the vehicle during charge sustaining operation. The first controller implemented was a simplified bang-bang controller to operate at the global minimum BSFC. A power-tracking controller was then developed to minimize powertrain losses. The power-tracking controller substantially reduced the vehicles energy consumption on simulated EPA drive cycles.

Table of Contents

Table of Figures

Table of Tables

Table Of Abreviations

AER	All Electric Range
ANL	Argonne National Lab
ASM	Automotive Simulation Models
AWD	All-Wheel Drive
BCM	Battery Control Module
BEV	Battery Electric Vehicle
BSFC	Brake Specific Fuel Consumption
CAN	Controller Area Network
CARB	California Air Resources Board
CD	Charge Depleting
CS	Charge Sustaining
d	Direct Axis
DC	Direct Current
DFMEA	Design Failure Mode Effects Analysis
DTC	Diagnostic Trouble Codes
ECM	Engine Control Module
ECU	Engine Control Unit
EEC	Emissions and Energy Consumption
EREV	Extended Range Electric Vehicle
ESS	Energy Storage System
FTA	Fault Tree Analysis
GCM	Generator Control Module
GHG	Green House Gas
GREET	Greenhouse Gases, Regulated Emissions, and Energy Use In Transportation
GWP	Global Warming Potential
HEV	Hybrid Electric Vehicle
HIL	Hardware in the Loop
li-ion	Lithium Ion
MABX	Micro Auto box
MCM	Motor Control Module
NiMH	Nickel Medal Hydride
NVH	Noise Vibration and Harshness
OPEC	Organization of Petroleum Exporting Countries
PEM,	Polymer Electrolyte Membrane
PHEV	Plug-in Hybrid Electric Vehicle
PID	Proportional Integral Derivative
PRNDL	Park Reverse Neutral Drive
q	Quadrature axis
Regen	Regenerative Braking
RPN	Risk Priority Number
SCU	Supervisory Controller

SIL	Software in the Loop
SOC	State of Charge
TCM	Transmission Control Module
UF	Utility Factor
VDP	Vehicle Design Process
WOT	Wide Open Throttle
WTW	Well to Wheel

1 Advanced Vehicle Technology Review

The contemporary automobile provides transportation, comfort, entertainment, and safety to 199 million drivers in the United States and over a billion worldwide (1) (2) . The energy consumed by these vehicles has a large impact on the environment. In order to understand the relevance of advanced vehicle technologies, the environmental impact of transportation and technologies reduce this impact will be reviewed.

1.1 Understanding the Impact of Transportation

The wide spread adoption of personal transportation has environmental, economic, and political impacts. The greenhouse gas emissions from the transportation industry are a major contributor to global warming (3). The oil industry and the cost of petroleum to the consumer have a direct and profound impact on the U.S. economy (4). The price and location of these limited petroleum resources are also the root cause of world-wide political turmoil (5). The impact of transportation is becoming increasingly relevant to the public as the worldwide energy consumption is expected to increase by over 50% by 2030 (6).

1.1.1 Green House Gas Emissions

The EPA defines a green-house gas as any gas that has the ability to trap heat inside the atmosphere (7). It is believed that these gases absorb longer wave length light that has had its energy reduced by interactions at or near the earth's surface (7). It is also believed that this absorption is responsible for the earth's temperature rising more than one degree over the last hundred years (8). The absolute magnitude of the earth's temperature change is slight, however it appears that there are high environmental sensitivities to this

change. Current research shows that in 2012 the summer ice in the Arctic Ocean is at its

all-time lowest retention rate (8). This year only 24% of the winter ice was retained

during the summer (8). The reduced retention of ice accelerates the warming of the planet

and disrupts world eco systems (9).

The EPA has classified the most abundant green-house gasses, carbon dioxide, methane,

nitrous oxide, and fluorinated gases. The contribution of each of these gases to the total

GHG emissions in the U.S. can be seen in Figure 1.
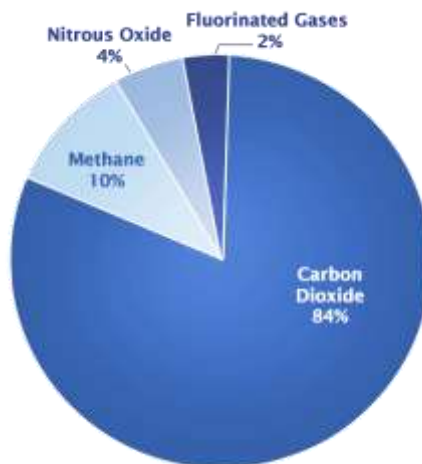
Figure 1: U.S. Green House Gas Emissions (7)

Carbon dioxide is the most emitted GHG; it is responsible for 84% of all U.S. GHG

emissions (7). U.S. carbon dioxide emissions were the most of any country in 2008 (6).

In 2010 the US produced total GHG emissions equivalent to 6.8 million metric tons of

carbon dioxide (7). These emissions levels are not sustainable because they are much

higher than the GHG emissions that can be offset. The United States land-use and

forestry are only able to offset approximately 2.5 million metric tons of carbon dioxide (7).

Carbon dioxide is the most abundant GHG but it does not necessarily have the largest impact on global warming. In order to normalize each gases impact on global warming the EPA also assigns a Global Warming Potential (GWP) to each GHG. The GWP represents that gasses ability to absorb energy over 100 years (7). Nitrous oxide has a GWP 300 times greater than that of carbon dioxide (7). That is largely because nitrous oxide has the potential to stay in the atmosphere for 100 years (10).

Transportation is second only to electricity production in total GHG emissions in the U.S. as can be seen in Figure 2.
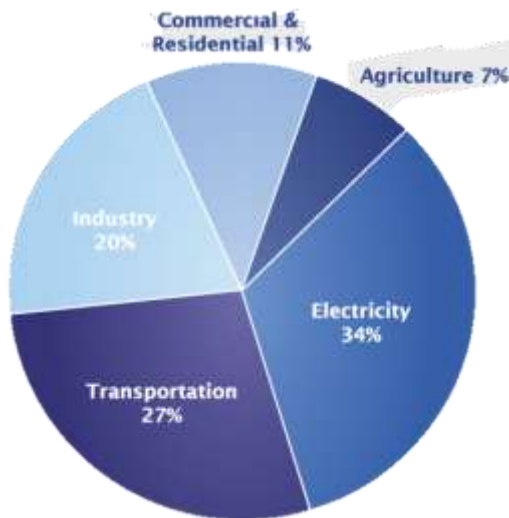
Figure 2: U.S. Green House Gas Emissions by Sector (7)

The transportation industry was responsible for 27% of the U.S. GHG emissions in 2010 (7). Emissions from the transportation sector are mostly from petroleum consumption,

therefore using alternative fuels and advanced technologies that increase vehicle

efficiency have the potential to largely reduce total GHG emissions. (7).

1.1.2 Petroleum Energy Usage

Petroleum energy usage is a major contributor to GHG emissions and is also the focus of

political and economic turmoil. There are 87.28 million barrels of petroleum consumed

every day (11). Out of that total petroleum consumption the US is responsible for 21.6%

of the daily usage (6). This daily usage is 2.4 times the amount of petroleum that is

produced in the U.S. daily (12). This high consumption causes the U.S. to be reliant on

imported oil. U.S. oil imports come from largely from Latin America, Canada, and the

Persian Gulf, and Africa (13). Many of the countries that export their oil to the U.S. are

part of the Organization of petroleum exporting countries (OPEC). Countries that are part

of OPEC have 71% of the world's oil reserves as shown in Figure 3 (6).
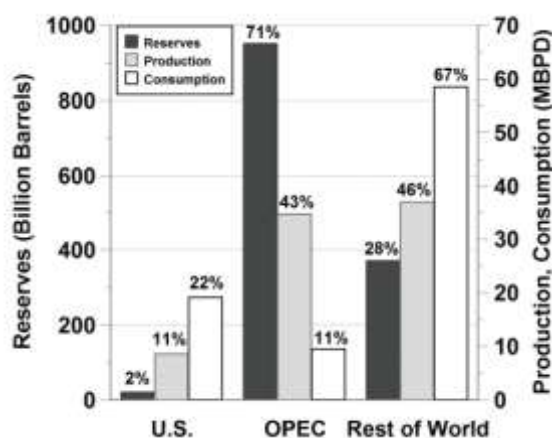
Figure 3: Oil Reserves, Production, and Consumption (11)

OPEC was founded by Iran, Iraq, Kuwait, Saudi Arabia and Venezuela and has since

grown to include 12 member countries. (14) This causes the price of imported petroleum

to be subject to foreign social, political, and economic influences. Increases in oil prices greatly affect the U.S. Economy, as the price of petroleum has been inversely correlated to the gross domestic product (12). Oil prices, which are currently $100/barrel, have been projected to continue rising to $155/barrel by 2035 (15).

The transportation sector is responsible for the majority of the petroleum energy usage. The U.S. was able has not been able to sustain the petroleum needs of the transportation sector alone since 1988/1989 (12). However, even in 1988/1989 the production was still short of satisfying the total need, including industrial, residential and commercial, and electrical utilities as can be seen in Figure 4 (12).
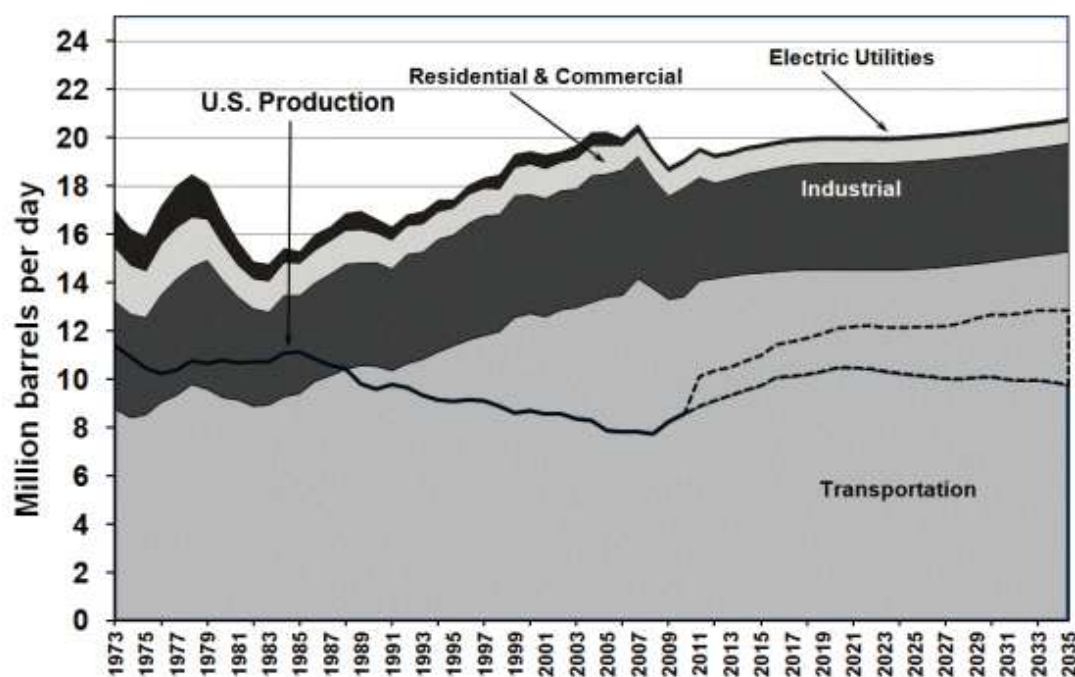
Figure 4: History of U.S. Oil Production and Consumption by Sector (11)

Current petroleum production is even lower than it was in 1973 but consumption continues to increase (12). This gap between consumption and production is expected to increase to at least 8 million barrels per day by 2035 if natural gas production is also included (12). If only conventional petroleum sources are used the gap has been projected to be as large as 11.1 million barrels per day by 2035 (12).

1.1.3 Government Regulations

In order to reduce the GHG emissions and reduce the U.S. dependence on foreign oil the government has implemented several regulations. The first fuel economy regulations were implemented in the 1970s in response to the Oil embargo (16). The Electric and Hybrid Vehicle act of 1976 was aimed at aiding the development of advanced battery technologies in response to the earlier oil embargo (17). In 2009 the Obama administration and the automakers agreed to increase the Corporate Average Fuel Economy (CAFE) to 35.5 mpg by 2016 (16). More recently the Obama administration passed a regulation to force auto makers to increase their CAFE to over 50 mpg by 2025 (16). It is hoped that this regulation will save the consumer money, reduce dependence on foreign oil and cut the GHG emissions in half. States governments have also been implementing their own regulations on automakers in order to lessen the impact of transportation. The California Air and Resources Board (CARB) have mandated that by 2025 15% of all cars sold annually in the state must be zero-emission vehicles (18). In response to CARB's mandate at least 10 additional states are also planning on reducing GHG emissions by implementing a similar law (18).

1.2   Advanced Vehicle Technologies

In order to reduce the environmental impact of transportation and to comply with government regulations, the automotive industry is actively pursuing many advanced vehicle technologies to improve vehicle efficiency and reduce GHG emissions. These vehicles decrease emissions by reducing energy consumption and using alternative fuels. GHG emissions are directly proportional to energy consumption so increasing overall vehicle efficiency through electrification decreases tail-pipe emissions (19). Alternative energy sources are being used to displace petroleum usage and reduce up-stream emissions. Many of these advanced vehicle technologies are old ideas that are finally becoming a practical reality thanks to modern advancements in solid-state electronics (17). The first electric cars were developed in 1882 (17). The first production electric car, the Electrobat, went into service in 1897 on the streets of New York City. (17). The Electrobat had a 5 kWhr battery pack and a claimed range of 25 miles, but eventually was replaced by the internal combustion engine (17). Now due to the combination of technological advancements and government regulations the number of zero emissions vehicles could double by 2025 (18). The National Research Council thinks wide spread adoption could still be several decades away but automakers are developing a wide array of vehicle technologies for early adopters in the current market (20). These technologies include different classes of electrified vehicles in several powertrian configurations, advanced fuel sources, and with different methods of energy storage.

1.2.1 Vehicle Classifications

Advanced vehicle powertrains can be classified by their level of electrification. SAE

recognizes hybrid electric vehicles (HEV), Plug-in hybrid electric vehicles (PHEV), and

battery electric vehicles (BEV). It is believed that with increased powertrain

electrification green-house gas emissions could be reduced by almost 50% (19).

However, this significant reduction in emissions comes at a cost that increases with the

level of electrification as shown in Figure 5 (19).
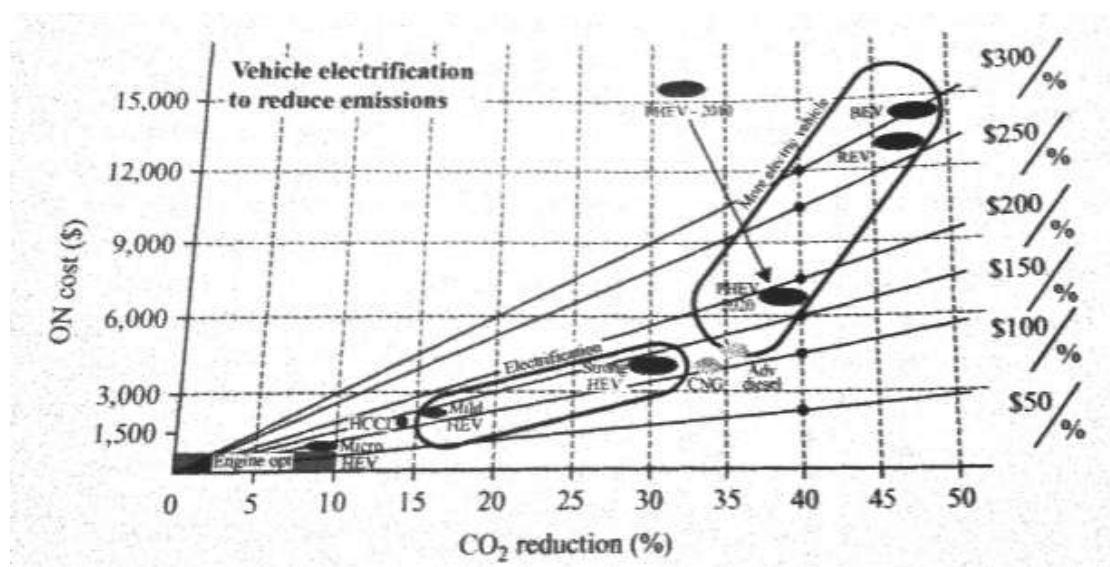
Figure 5: CO$_2$ Reduction and Cost of Electrification (19)

A BEV achieves the lowest CO$_2$ emissions but has the highest cost due to its larger

energy storage system.

1.2.1.1 HEV

A HEV is a vehicle that has multiple methods for energy storage, and propulsion power

(21). While having multiple methods of propulsion these vehicles have only a single

liquid fuel source (19) . HEV's reduce GHG emissions, and displace petroleum energy by

utilizing both powertrains to increase vehicle efficiency (22). The HEV engine is typically sized to meet high power demands, while the electric powertrain is sized to enable engine start/stops, recapture energy during braking, and in some cases enable low speed electric only operation (22). The current best-selling HEV on the market is the Toyota Prius, which is also the best-selling car in California (23) (24). Over two million Prius have been sold world-wide by Toyota (25). Approximately half of those have been sold in the United States (26). It is estimated that the Prius fleet has successfully offset 12.4 million tons of CO_2 emissions since 2000 (25). The HEV represents the first step in wide spread vehicle electrification. In order to make more significant reductions in emissions and petroleum energy usage vehicle architectures also need to support diversified fuel sources (22).

1.2.1.2 PHEV

A PHEV is a vehicle that has multiple methods of propulsion power, and also has the ability to store electrical energy generated outside of the vehicle in a rechargeable energy storage system (21). PHEV's can also be further defined by their operating strategy and their all electric range (AER). A PHEV can operate in a charge depleting (CD), and charge sustaining (CS) mode. During CD operation the battery is used as the primary energy source until a target state of charge (SOC) is reached in the battery. At that time the additional onboard fuel source is used to deliver power to the road while maintaining the battery SOC over the drive cycle.
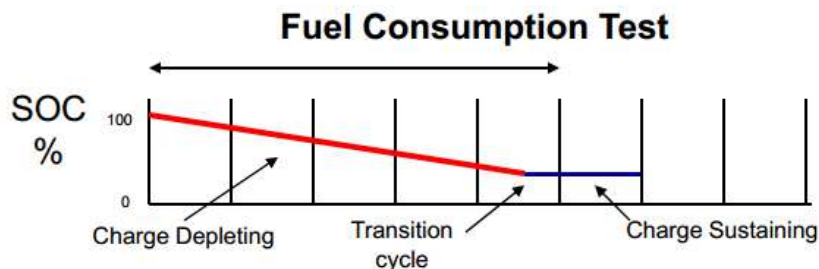
Figure 6: Charge Depleting and Charge Sustaining (27)

In order to utilize the PHEV's ability to displace large amounts of petroleum, an electric

powertrain sized to meet peak power demands is required to enable full CD operation

(22). This concept is the basis for GM's extended rang electric vehicle (EREV). An

EREV is PHEV that can achieve full vehicle performance during electric only operation

and also has a small engine to extend the vehicles range beyond the AER. PHEV's that

adopt a blended strategy must rely on the engine to deliver full vehicle performance and

will be limited in their ability to displace fuel and GHG emissions (19). Research

conducted by General Motors shows that an 8 kWhr E-REV can displace 80% of fuel

usage assuming a driver can charge at home and work (19). This strategy can achieve a

25% reduction in GHG emissions when compared to conventional blended PHEV (19). It

is also believed that these emissions will continue to be reduced as the grid electricity

production becomes cleaner (28). Other companies have chosen to adopt a blended

strategy in order to achieve their fuel economy targets. Toyota favors a blended PHEV

strategy to reduce powertrain cost and complexity while still meeting driver power

demands (29) . Toyota determined that an increased battery capacity and the associated

reduction in GHG emissions, does not outweigh the cost of increased mass, volume, and

price (29).

Current PHEVs sold in America include the Chevy Volt, Fisker Karma, and Toyota Prius

Plug-in. These vehicles price and fuel economy are shown in the table below. Prices

shown do not include the 7,500 federal tax credit that is available for electric vehicles.

The cost and performance of the PHEV's that are currently available in the U.S. are

summarized in Table 1.

Table 1: Current PHEVs on Sale in the U.S. (30)

	Chevy Volt	Fisker Karma	Toyota Prius
Price [$]	39,145	95,900	32,000
AER [mi]	40	33	11
CD Fuel Economy [mpgge]	93	53	95
CS Fuel Economy [mpgge]	37	20	50

1.2.1.3 BEV

A BEV is a vehicle whose only on board energy source is stored grid electricity. The

fully electric powertrain in a BEV can achieve vehicle efficiencies greater than 60%

while a conventional vehicle can achieve around 20% (31). A BEV also has much lower

system level complexity than that of a PHEV, which greatly reduces the control effort

required. The electric powertrain is also simpler than that of an internal combustion

engine. An electric motor has only a single moving part, while an internal combustion

motor can have over 100. A BEV can also achieve complete reduction of petroleum

usage and GHG emissions when charged with renewable energy sources (32). Despite

their huge potential for GHG emissions reduction, BEVs are limited by current battery

technology. Customers are very concerned about current battery characteristics including

range, cost, and charge time. Potential consumers suffer from "range anxiety" when

considering a BEV which is slowing the adoption by the market (33). Conquering "range

anxiety" requires increasing the vehicles range, expanding the charging infrastructure and

reducing charge times. Increasing the vehicles range greatly increases cost, and mass

which can increase energy consumption.

1.2.2 Hybrid Powertrain Classifications

Hybrid vehicles can be further classified by the lay-out of the powertrain components and

methods for power delivery.

1.2.2.1 Series

A series hybrid is one in which the primary propulsion power comes from an electric

motor only. An onboard generator is used to maintain the charge in the battery after the

AER is exceeded (21). A powertrain diagram of a series hybrid can be seen in Figure 7
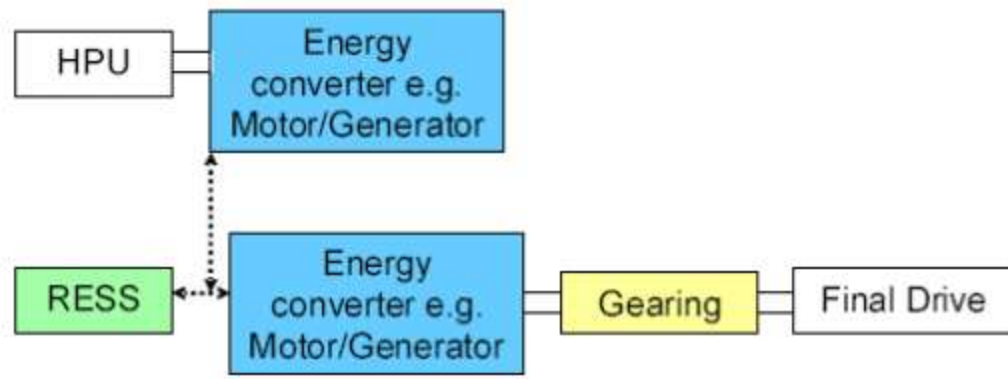
Figure 7: Series Hybrid Diagram (21)

The advantage of the series hybrid configuration is that the engine is completely

decoupled from the road, allowing for precise control of the engine during charge

sustaining operation. The efficiency gains through precise engine control are limited by

the additional conversion losses between the engine, the generator, and the motor (34).

The series hybrid architecture has a fully sized electric powertrain, and an internal

combustion engine sized to meet the vehicles continuous power demands (35).

1.2.2.2 Parallel

A parallel hybrid vehicle has two independent power systems that can also be operated

together. A powertrain diagram for a parallel hybrid split at the input to the gearbox can

be seen in Figure 8.
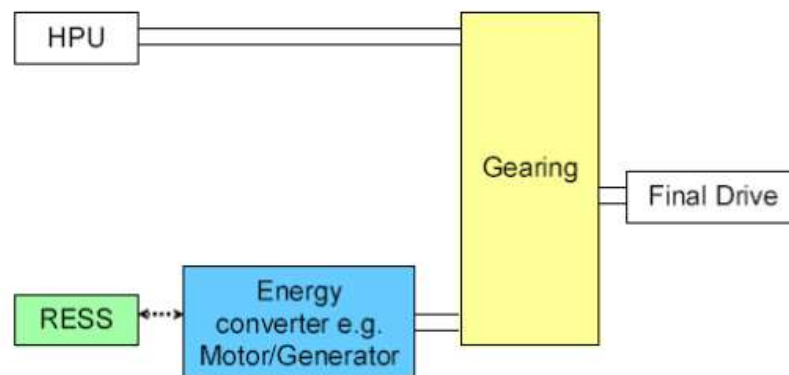
Figure 8: Parallel Hybrid Diagram (21)

Parallel hybrid systems can be configured in several different ways. SAE defines the P1,

P2, belted alternator starter, crank shaft motor generator (also the integrated motor

generator or flywheel assist), and the through the road configurations. The P1 is one in

which the engine and generator are directly coupled and this unit can be isolated from the

transmission by a clutch. The P2 system has a similar clutch between the electric motor

and the transmission but also has a clutch between the engine and generator.

The crankshaft motor generator system has an eelctric motor directly coupled to the

engine crank shaft.
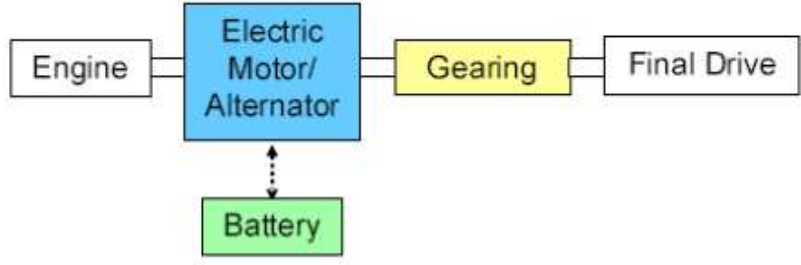
Figure 9: Crankshaft Motor Generator Diagram (21)

The belt-alternator-startor system uses an electric machine connected to the engine
through a belted connection. This motor can provide the functionality of a starter, and an
alternator to implement engine start stops and energy regeneration (21).
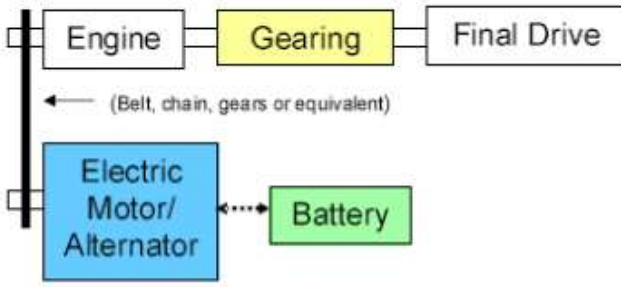
Figure 10: Belt Alternator Starter Diagram (21)

Another common parallel configuration is the parallel thorugh the road. The through the
road structure is an all-wheel drive (AWD) configuration . In this configuration each
power train is connected to an axel independently as shown in Figure 11.
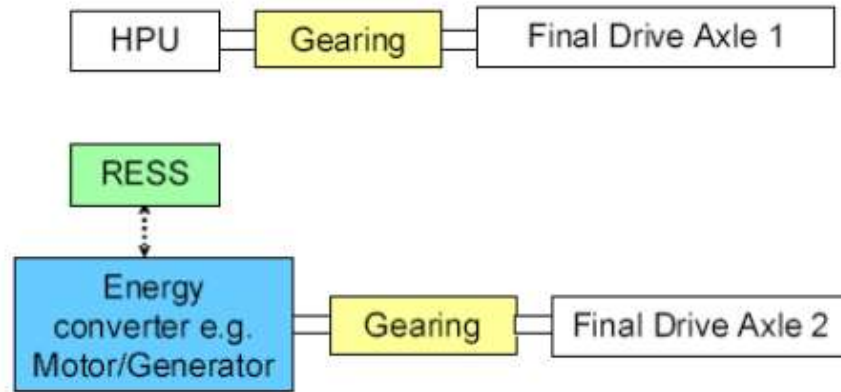
Figure 11: Parallel Through the Road Diagram (21)

1.2.2.3 Power-split

The power-split configuration is a parallel configuration that allows for engine power to be delivered through either electrical or mechanical power (21). These configurations can be further divided by the manner in which the split occurs. Input split, and output split configurations are shown in Figure 12.
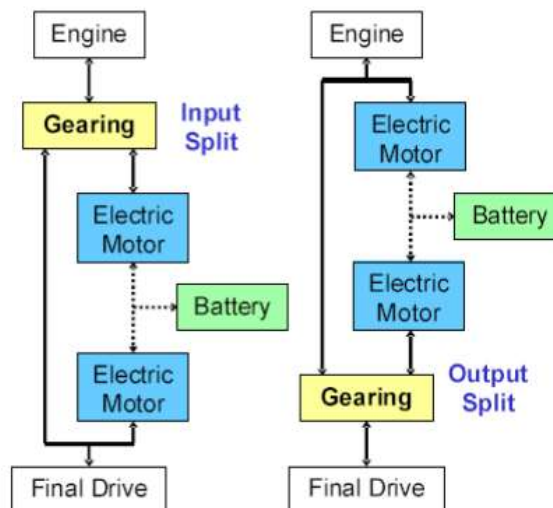
Figure 12: Output and Input Split Diagram (21)

The difference between the two is the location of the differential gearing. An input split

has both the engine and electric motor connected separately through the differential

gearing (21). The output split configuration couples the motor and engine before the

differential through a gear assembly (21). The third power-split configuration combines

both the output and input split configurations. The compound split has a differential

gearing at both the input and the output of the transmission (21).
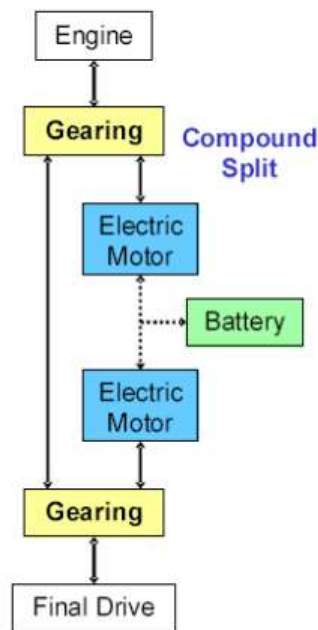
Figure 13: Compound Split Diagram (21)

1.2.3 Alternative Fuel Sources

GHG emissions can only be offset marginally by increased efficiency, for greater impact

drastic changes in the fuel source need to be made. (19) (22). Alternative fuels are often

sold as blends, and are characterized by the amount of bio-fuel in the blend. For example,

E85 contains 85% bio-fuel and 15% petroleum based fuel.

1.2.3.1 Ethanol

Ethanol is an alternative fuel source made from the fermentation of the biological feed, and was regarded by Henry Ford as the fuel of the future (36). Ethanol has the potential to significantly reduce GHG emissions and slow the depletion of petroleum resources. Studies conducted by Argonne National Labs show that a HEV using corn based E85 can achieve a 40% reduction in GHG emissions, and a 70% reduction in petroleum energy usage relative to a conventional gasoline vehicle (37).
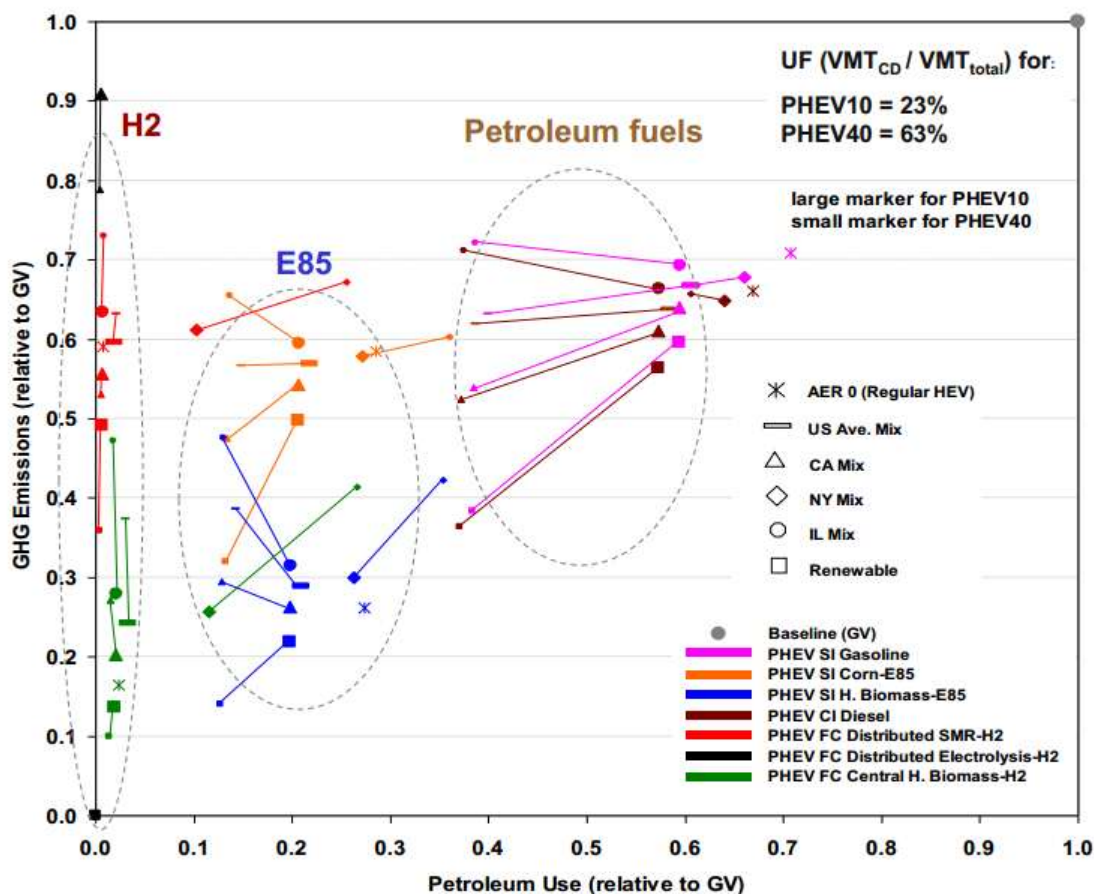
Figure 14: GHG Emissions and Petroleum Energy Usage Relative to a Conventional Gasoline Vehicle (37)

Ethanol feed stocks include, molasses, sugarcane, and starch. There is a growing concern that, with increased dependence on ethanol, it would become more profitable for farmers to focus their efforts on growing crops as a feed stock for fuel, rather than a food source (38). Ethanol now consumes 15% of the world corn supply; the recent increase is projected to cause a 2%-3% increase in corn prices (39). In Brazil 45% of sugar cane production is used for food while the other 55% is used to produce ethanol (36). Sugar cane and biomass have the largest potential to reduce GHG emissions. E85 is the most wide spread alternative fuel with over 2,000 public fueling stations around the country (40). E85 is also 30 cents cheaper per gallon than conventional gasoline (41).

1.2.3.2 Bio-diesel

Bio-diesel is an alternative fuel that is created from vegetable oil, animal fats, or recycled cooking oil and can be used in compression ignition engines (42). Bio-diesel can be produced from soybeans, jatropha, cottonseed, rubber seed, algae, and mustard seed (36). No engine modifications are required to run B20, however higher percentage blends such as B100 do require changes to fuel lines and gaskets (43). It is estimated that B100 can achieve 75% reduction in CO_2 emissions however NOx emissions can increase with the amount of bio-diesel in a blend (44). Some of the drawbacks of bio-diesel include, cost, lower energy density, higher NO_x emissions, and potential for increased engine wear when made from low-grade vegetable oil (43). Bio-diesel is slightly more expensive than regular diesel. B20 prices were 5 cents more expensive than conventional diesel in 2011, and required government subsidies to keep the price competitive. (45). The bio-diesel fueling infrastructure is not as large as the E85 infrastructure, with only 294 public B20 fueling stations in the United States (46).

1.2.3.3 Hydrogen

Hydrogen is an attractive fuel source it is both clean and seemingly abundant. A hydrogen car using a fuel cell produces electricity from stored hydrogen and oxygen while emitting only heat and water (47). The most common type of fuel cell is the Polymer Electrolyte Membrane (PEM), which is also commonly called the Proton Exchange Membrane (48). The PEM works by first separating the electrons from the hydrogen at the anode using a platinum catalyst (49). Then the positively charged hydrogen ions are allowed to pass through the membrane to the cathode while the

electrons are forced to go through an electrical circuit (49). At the cathode the hydrogen

ions and the electrons react to form water (49).
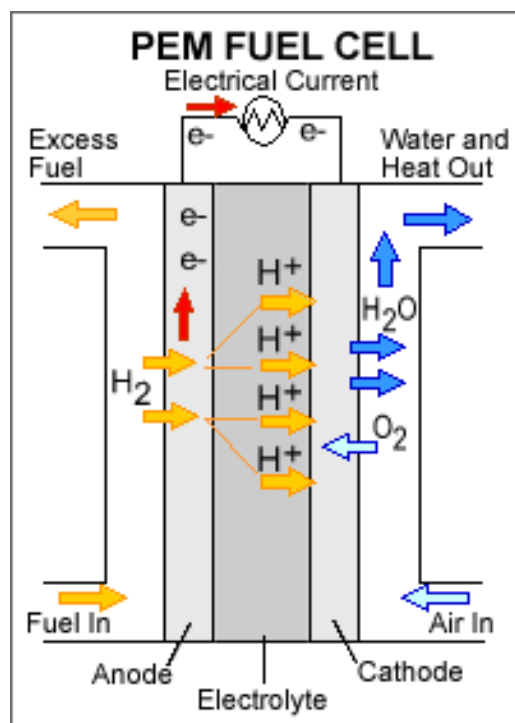
Figure 15: PEM Fuel Cell Diagram (50)

There are several engineering challenges associated with making hydrogen a viable fuel

source including, the energy density, energy required to produce the fuel, fuel cell cost,

and fuel cell power output. Due to the low energy density of hydrogen large pressure

vessels are required to achieve a range that is competitive with a conventional vehicle

(49). Although hydrogen is a common element the pure gas form is not so abundant,

requiring hydrogen to be extracted from other compounds (49). The most common

process for extracting hydrogen in the U.S. is steam reforming methane. Extracting and

compressing the hydrogen from natural gas has a high energy cost and adversely effects

the upstream emissions (37). Argonne national laboratory found that a hydrogen fueled

HEV could achieve a 40% reduction in GHG emissions and nearly 100% reduction in

petroleum usage even with the high energy cost required to produce the fuel (37). Fuel

cells are better suited to constant power applications, in order to meet the peak power

demands of a vehicle an additional energy storage system is typically required (49).

Adding a battery to provide peak power output adds to the total vehicle cost, mass, and

further reduces the available space.

1.2.3.4 Grid Electricity

Grid electricity is an alternative fuel source that can be stored onboard PHEVs and BEVs

using chemical and electrical energy storage methods. Vehicles powered by only grid

electricity can reduce tail-pipe emissions completely and greatly reduce energy

consumption by utilizing high efficiency electric powertrains. There are no tail-pipe

emissions associated with grid electricity, however the emissions associated the

production of electricity are significant. The severity of the upstream emissions depends

directly on how the energy was produced (51). The break-down of U.S. electricity

production methods are shown in Figure 16.

Coal (42%)
Natural Gas (25%)
Nuclear (19%)
Renewable (13%)
Petroleum (<1%)
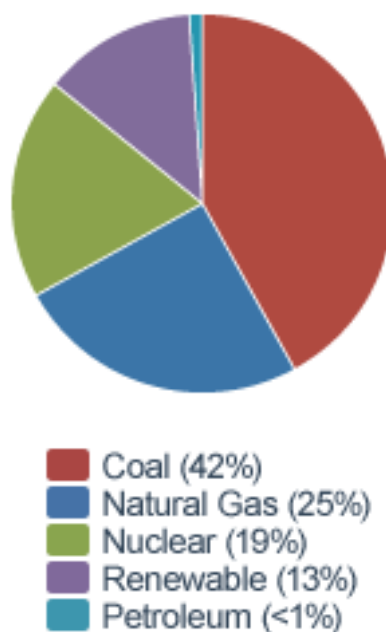
Figure 16: 2011 Relative U.S. Electricity Production (51)

In the U.S. 42% of grid electricity comes from coal which emits a large amount of green-

house gasses (51). Based on national average production methods a vehicle powered by

grid electricity can reduce GHG emissions by over 40% when compared to a

conventional vehicle (52). The cost of grid electricity is approximately ¼ the price of

gasoline (52). The electrical grid is an already established infrastructure that can easily

handle the charging demands of wide spread electric vehicle adoption (52). Due to the

availability of electricity charging stations can be easily installed at home, work, and in

public areas (52). Wide spread adoption of grid electricity as a primary fuel source is

greatly hampered by current energy storage system limitations and the cross-country

charging infrastructure.

1.2.4 Energy Storage

One of the biggest challenges preventing the adoption of electrified vehicles is creating

cost effective energy storage systems. Energy can be stored chemically, electrically, and

mechanically. Chemical energy storage in a battery is currently the only energy storage method in production.

1.2.4.1 Chemical

Nickel metal-hydride (NiMH) and Lithium ion (Li-ion) are the two most common chemistries used in the modern electrified vehicle. Li-ion batteries have several advantages over the NiMH packs and are used primarily in PHEV and BEV applications (53). Li-ion batteries have a higher specific power, a higher specific energy, and a higher efficiency than NiMH packs (53). Li-ion batteries have an average of 5% greater efficiency than NiMH, which causes less heat generation and reduces cooling requirements (53). Li-ion batteries also have a more constant voltage across the entire charge range. NiMH batteries have a limited depth of discharge due to the memory effects that are not present in Li-ion packs (53).

Recent crash test fires have increased concerns over li-ion safety (54). Li-ion cells can go into thermal runaway in abuse tests causing a large discharge of energy; however improvements in materials and chemistry variations have reduced the severity of these failures (55). Li-ion batteries are also very sensitive to cold temperatures. Low temperatures greatly reduce the power output of Li-ion cells due to the increase in internal resistance (56). At freezing temperatures the AER range could be reduced by up to 10.7% and some BEV's may even be inoperable (56). Low temperatures also cause a drastic increase in the energy consumption for BEVs due to their reliance on resistive heaters for cabin warmth. There are also realistic concerns about the long term viability of Li-ion batteries, as lithium is a limited resource. The largest lithium reserves are

located in Bolivia, Chile, and China, mass production of Li-ion energy storage could cause an increased dependence on foreign resources. (57). Several companies are working on cost-effective recycling methods for li-ion batteries; however extracting the lithium remains a challenge.

1.2.4.2 Electrical

Ultra-capacitors are used to store electrical energy similarly to a conventional capacitor. Ultra-capacitors, which are also known as super capacitors or double –layer capacitors, store electrical charge between two electrodes immersed in an electrolyte (58). An ultra-capacitor has a very high power output because no chemical reaction is required to charge and discharged (59). Ultra capacitors also perform much better than batteries in cold weather, and life cycles tests (59). Although they have a high power density ultra-capacitors have a very low energy density compared to batteries (59). Nano-technology is expected to improve ultra-capacitor energy density to be within 50% of a Li-ion battery energy density (60).

1.2.4.3 Mechanical

Energy can also be stored mechanically. The only mechanical storage method used in vehicles is a flywheel energy storage system. A flywheel energy storage system stores rotational energy by accelerating a rotor to a very high angular velocity (20,000 RPM or greater) (61). In order to reduce losses the flywheel must be inside a vacuum and often uses magnetic bearings (61). Flywheel hybrids, also known as Flybrids, have been implemented in racing application and OEM concept cars (62). The most notable is the Formula 1 kinetic energy recovery system that utilizes a flybrid design to store energy

during breaking and then use it during accelerations (62). Flybrid systems have significant parasitic losses, and create inertial effects that must be considered to maintain desirable vehicle dynamics.

1.2.5 Importance of control systems for HEV's

Model based control system design is critical to the modern Vehicle Development Process (VDP) due to the high level of system complexity and short production cycles. In order to meet production deadlines automakers are adopting the latest tools, for modeling and simulation to facilitate controls development earlier in the VDP. Two examples of these tools are Hardware in the Loop (HIL) testing hardware, and automatic code generation using Matlab and Simulink. DSPACE hardware in the loop systems were critical to the development and testing of more than100 electronic control units (ECU) inside the Chevy volt (63). These systems accelerated the testing process and increased test coverage by providing a safe and repeatable platform for testing software. The majority of control system development for GM is now being done using Matlab and Simulink auto code generation, rather than traditional hand-code (63). Nearly all of the volts code was automatically generated by Simulink from the original block diagram models (63). GM feels that automatic code generation increases the efficiency of the development process by 30-35% resulting in the earlier development of vehicle test mules (63). Before algorithm engineers would develop the models and control algorithms in Simulink and then manually translate the algorithm into hand code (63).

PHEV's require sophisticated supervisory controllers to manage their modes of operation and ensure that powertrain components are working harmoniously. The amount of

software development necessary to control all of these subsystems is evident in the amount of code required by the vehicle. The Volt has 10 million lines of code, which is more than the Boeing 787 and an F-35, which have 8 million and 5.7 million lines of code respectively (63).

1.2.6 Thesis Definition

This thesis details the architecture selection process, and the development of a supervisory control unit for a series plug-in hybrid electric vehicle as part of Embry-Riddle Aeronautical University's involvement in EcoCAR2: Plugging into the Future. In order to achieve the competition goals a supervisory controller was developed to safely control the series PHEV powertrain. The supervisory controller was designed to operate the vehicle safely and efficiently in all modes of operation.

1.2.6.1 Thesis Scope

1. Architecture Selection Process

   A multidisciplinary architecture selection process was conducted to choose the most viable vehicle architecture for ERAU's entry into EcoCAR2.

2. Plant Model Development

   A real-time capable mathematical model was developed simulate the selected vehicle architecture for controller development. The vehicle model was developed using Matlab, Simulink, and dSPACE tools.

3. SCU Development

   A supervisory control unit was developed to interpret driver commands and control the interaction between powertrain components. The controller structure

was designed to be intuitive, and scalable. This structure incorporated a fault

detection module for safety critical algorithms.

4. Power Management Strategy

A power management algorithm was developed to control the vehicles engine and

generator unit during charge sustaining operation. This algorithm was designed to

reduce engine losses.

2   Architecture Selection Process

With increased regulations on fuel economy, and a growing effort to reduce the environmental impact of transportation many manufacturers are offering hybrid electric vehicles, plug-in hybrid electric vehicles, and battery electric vehicles. To save cost manufacturers often choose to integrate electrified powertrains into conventional vehicles. Reducing vehicles environmental impact can be achieved by using several different hybrid vehicle architectures (64). Due to the complex system interactions of a PHEV's powertrain vehicle performance also depends on the vehicles control strategy (65) (66). These challenges being solved by the automotive industry are the same ones that are presented to students involved in the EcoCAR 2: *Plugging into the future* competition. EcoCAR2 is a three year collegiate engineering competition that challenges students to reduce the environmental impact of a donated 2013 Chevrolet Malibu. The goals of the competition are to minimize GHG emissions and petroleum energy consumption, while never compromising safety and maintaining high levels of performance and consumer acceptability. This section details the process used to assess the viability of three vehicle architectures. The architecture determined to be the most viable was submitted as ERAU's vehicle for EcoCAR2.

In order to evaluate the architectures performance, a fuel source and components must be selected. Fuels were analyzed using GREET, to determine the Well to Wheel (WTW) GHG impact of each fuel selection. GREET is a life-cycle model developed by Argonne National Laboratory (ANL) that takes into account all processes involved in the manufacture, distribution, and consumption of a fuel (67). B20 bio-diesel was determined

to be the most viable fuel source for Embry-Riddle Aeronautical University. B20 was the most viable because of on-campus bio-diesel facilities even though it did not have the lowest WTW GHG emissions.

After the fuel was selected a point-mass simulation was used to establish minimum mobility requirements to complete the EPA drive cycles while meeting performance targets. These requirements were used to select powertrain components for architecture simulations using Autonomie. Autonomie is a simulation tool developed by ANL to quickly evaluate vehicle architectures. The three PHEV architectures that were studied in detail were a Series PHEV, a series-parallel through the road PHEV, and a Pre-transmission PHEV. A utility-factor (UF) corrected four cycle blend of EPA highway and city cycles was used to evaluate energy consumption and emissions. Vehicle performance was measured using 0-60 acceleration and grade-ability metrics.

Architectures were also evaluated from a mechanical integration perspective. A space claim analysis was conducted by William Townsend Hyatt to determine the feasibility of packaging the proposed power-trains in the Malibu and potential impacts on consumer acceptability. Each aspect of the study was weighted to determine the most effective architecture for ERAU, a FWD Series PHEV using B20 bio-diesel.

2.1   Fuel Analysis

To analyze WTW impacts of selected fuels Greenhouse Gases, Regulated Emissions and Energy Used in Transportation (GREET) 1.8 was used. The WTW impact on energy consumption and emissions in a PHEV was evaluated using three different fuel sources: E85, B20 and Gaseous Hydrogen. The study conducted by William Townsend Hyatt

looked at the energy consumption and emissions for all electric ranges (AER) from 20 to 40 miles. The results for the 40 mile AER are summarized in Table 2.

Table 2: 40 mi AER GREET Results

	H2	E85	B20
GHG Emissions [g/mi]	277.29	300.44	301.88

The hydrogen fuel cell car uses less energy and released fewer GHGs than either E85 or B20. Unfortunately the university does not have the facilities to make hydrogen a viable fuel source. The next best fuel selection based on GREET data is B20. B20 had similar GHG production as E85 at the 40 mile AER, but uses less energy due to the higher efficiency of the diesel engine. ERAU also has an on-site bio-diesel production facility that uses recycled vegetable oil from the campus cafeteria which makes it the most available fuel source to the team.

2.2 Point Mass Mobility Model

A point-mass vehicle model was constructed using MATLAB and Simulink. This model was used to generate initial component requirements before constructing the Autonomie power train models. This model was also used to evaluate the energy consumption and losses on the drive cycles. The component requirements were generated from the simulated power demands at the wheels during 1-Hz UDDS, US06, and HWFET drive cycles (68).The model was initialized with parameters that represented the team's potential Malibu. The mass was calculated using an estimated weight of potential powertrain components. The vehicle parameters are summarized in Table 3.

Table 3: Estimated Vehicle Parameters

Vehicle Mass (kg)	Frontal Area(m²)	C_d	C_{rr}
1790	2.295	.25	.00683

The tractive force at the wheels required to meet the drive cycle was calculated at each

time step using the road load equation shown in Equation 1 (69). The road load equation

sums the forces on the vehicle during driving. These forces are the inertial force,

aerodynamic drag force, rolling resistance forces, and normal force of gravity on a grade.

The coefficient of rolling resistance was assumed to be constant when velocity was non-

zero.

Equation 1

$$F_{tractive} = F_{inertial} + \frac{\rho v^2 A_f C_d}{2} + mg C_{rr} sign(v) + mg sin(\theta)$$

The power at the wheels during each time interval was found by multiplying the tractive

force and the current vehicle velocity.

Equation 2

$$P_i = F_{tractive} * V_i$$

The power was integrated using a left Riemann sum to calculate the energy required to

meet the drive cycle. Only powers where force was positive were summed.

Equation 3

$$w = \sum_{i=1}^{n} P_i(t_{i+1} - t_i)c_i, \text{ where } C_i = \begin{cases} 0 \text{ when } P_i < 0 \\ 1 \text{ when } P_i > 0 \end{cases}$$

The average tractive power required by the drive cycle was found by summing the

positive power demand and dividing by the number of instances where positive power

occurred.

Equation 4

$$P_{avg} = \frac{\sum_{i=1}^{n} P_i c_i}{\sum_{i=1}^{n} (t_{i+1} - t_i)c_i}, \text{ where } C_i = \begin{cases} 0 \text{ when } P_i < 0 \\ 1 \text{ when } P_i > 0 \end{cases}$$

The results from the point mass simulation are summarized in Table 4.

Table 4: EPA Drive Cycle Power and Energy Results

	UDDS	US06	HWFET
Peak Power [kW]	39.465	98.5	31.99
Average Power [kW]	7.77	23.953	10.759
Energy [kWh]	1.6314	2.7567	2.0129

The peak power demands on each drive cycle were used as minimum requirements for

traction motor peak power. In order to follow the US06 velocity trace a vehicle would

require 98.5 kW of available tractive power. The average power required during each

drive cycle was analyzed to find requirements for charge sustaining power. In order to

charge sustain on the US06 drive cycle it was determined that a 24 kW generator would be required.

In order to further understand drive cycle mobility requirements, the contribution of each portion of the road load was analyzed. The energy required to accelerate the vehicles mass was compared to the energy required to overcome aerodynamic losses, and rolling resistance. The energy for each of these categories was summed during the drive cycle for all positive tractive forces. The UDDS drive cycle is a lower speed drive cycle and the majority of the drive cycle energy is used to accelerate the mass of the vehicle. On the Us06 and HWFET, the higher speed drive cycles, the aero losses were much more significant as can be seen in Figure 17.
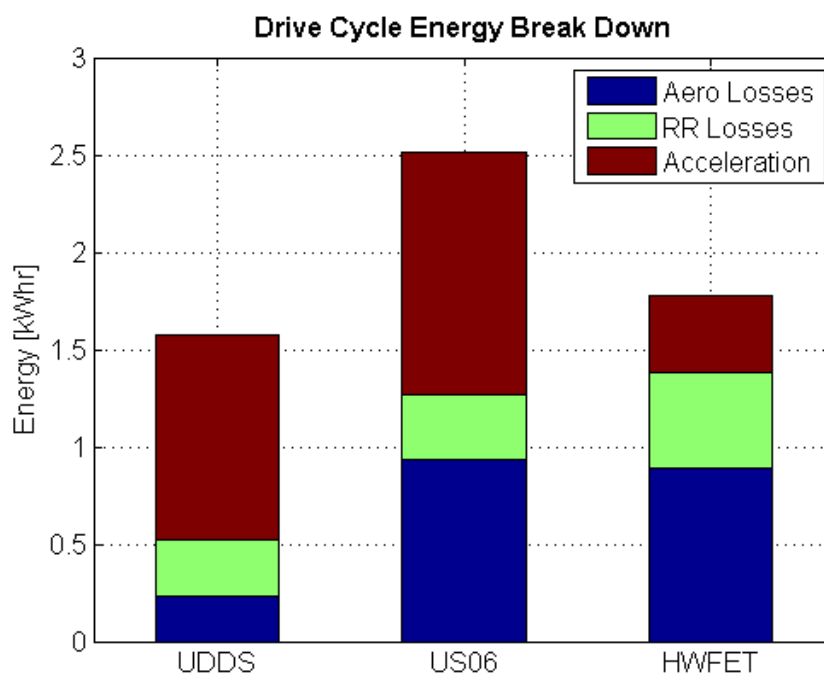
Figure 17: Drive Cycle Energy Break Down

A road load sensitivity analysis was conducted to quantify the equivalent impact of changes in mass, rolling resistance and aerodynamic drag. This study analyzed the sensitivity of the combined energy consumption from all three drive cycles. Mass, Crr, and CD, were all varied by 10% each. As expected, from the earlier analysis, the change in mass resulted in the largest change in energy consumption. A 10% change in vehicle mass resulted in a 6.47% change in energy consumption. The results of the sensitivity study are summarized in Table 5.

Table 5: Energy Consumption Sensitivity to 10% Change in Vehicle Parameters

	10% Mass Delta	10% Crr Delta	10% CD Delta
Energy Consumption [%]	6.47	1.91	3.49

These sensitivities were then related back to the original values to find absolute equivalence between each quantity. The change in CD and Crr that achieves the same change in energy consumption as a given change in mass are summarized in Table 6.

Table 6: Equivalent Energy Consumption Sensetivities to Vehicle Parameters

Equivalent Sensitivities	Mass	Crr * 1000	CD * 100	Energy Consumption [%]
Mass	50 kg	.64	1.53	1.81
CD	32.76	.42	1	1.18
CRR	7.74	.1	.24	.2797

A change in of .01 in the coefficient of drag is equivalent to removing 32.76 kg of vehicle mass or a .42 change in CRR. These sensitivities can be used to evaluate the feasibility of future modifications.

The aerodynamic losses and rolling resistance losses were then assessed at varying speeds. At velocities greater than 18 m/s (40 mph) the non-linear aero dynamic losses becomes greater than the losses due to rolling resistance as can be seen in Figure 18.
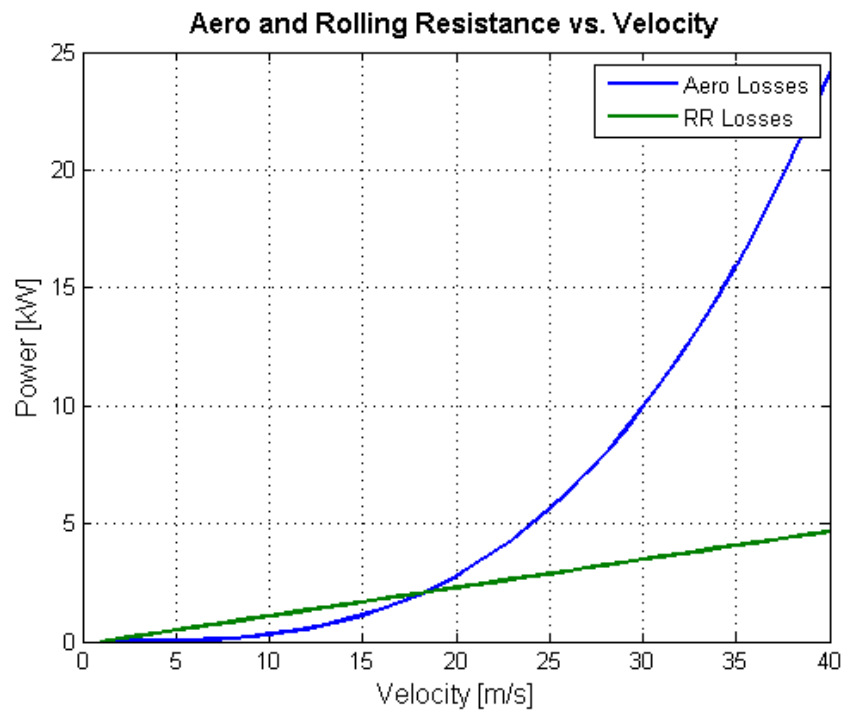
Figure 18: Aero and Rolling Resistance Forces as a Function of Velocity

The idle time on the EPA drive cycles was also analyzed. Idling results in significant losses for conventional internal combustion vehicles during city driving. The UDDS

drive cycle contains 18.9% idle time, but with engine start/stop abilities idling losses could be mitigated. The idle time on each drive cycle can be seen in Table 7.

Table 7: Percent Idle Time on EPA Drive Cycles

	UDDS	US06	HWFET
Idle Time [%]	18.9	7.4875	.5236

The power required to maintain a grade at highway speeds was also analyzed to supplement the continuous power requirements from the drive cycle analysis. It was found that in order to maintain a 10% grade at 60 mph required nearly 60 kW; the results are summarized in Table 8. This was used for the continuous vehicle power requirement because it was much greater than the continuous power required over the EPA cycles.

Table 8: Tractive Power Required to Maintain 60 mph up a Grade

	3.5% Grade at 60 mph	10% Grade at 60 mph
Power [kW]	29.57	59.96

The power required to accelerate from 0 to 60mph was used in addition to the drive cycle analysis to create peak power requirements. The power demand was calculated using Equation 5 (70).

Equation 5

$$P_t = \frac{M}{2t_a}\left(V_f{}^2 + V_b{}^2\right) + \frac{2}{3}Mgf_rV_f + \frac{1}{5}p_aC_DA_fV_f{}^3$$

The first term represents the power used to accelerate the vehicle while the second and third terms represent the power used to overcome the tire rolling resistance and

aerodynamic drag. The V_b term represents the initial speed and was zero for these tests.

The target time for 0-60mph acceleration was 9 seconds. The power required to achieve 9

second 0-60 time with varying vehicle masses are shown in Figure 19.
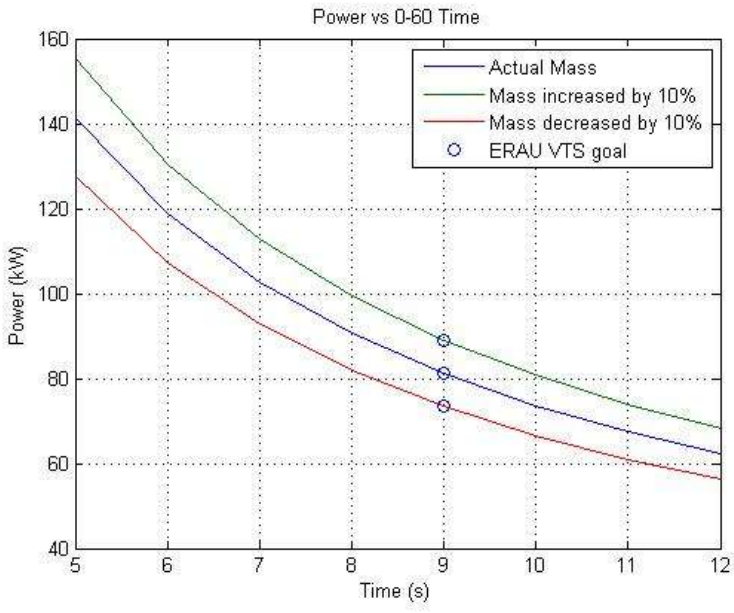
Figure 19: Power Required for (0-60) mph Accelerations

From the acceleration simulations it was determined that 83 kW of peak power would be

required to achieve the 9 second acceleration goal. From the results of the point mass

analysis final peak and continuous power requirements were developed. The

requirements are summarized in Table 9.

Table 9: Initial Power Requirements

PEAK POWER (KW)	100
CONTINUOUS POWER (KW)	60

2.3 Autonomie Simulations

Autonomie was used as the primary simulation tool to evaluate the proposed vehicle

architectures. For these simulations a common set of powertrain components were

selected to meet all of the initial requirements from the point mass simulation. The

selected components are summarized in Table 10 and were chosen from components that

were available commercially or through donations from competition sponsors.

Table 10: Powertrain Components

Engine	Trans	Traction Motor	Generator	Battery
GM 1.7LCI	GKN ETrans	Remy HVH 250-90P	Remy HVH 250-90S	A123 12-15P-6S

These components were added to the Autonomie framework so they could be used in the

vehicle simulations. The three PHEV architectures selected for simulations were Series,

Series-Parallel through the Road, and Pre-Transmission Parallel.

A series PHEV is one in which the engine never drives the wheels. The engine is instead

coupled to a generator to sustain charge in the battery after the AER is exceeded.

The Autonomie powertrain diagram for the series PHEV can be seen in Figure 20.

Figure 20: Series PHEV Autonomie Diagram

The Pre-Transmission Parallel PHEV uses an electric motor and an engine that can both drive the wheels through the transmission. The engine can also be decoupled from the system for full charge depleting operation. The Autonomie powertrain diagram can be seen in Figure 21.

Figure 21: Pre-TX PHEV Autonomie Diagram

The Series /Parallel through the road architecture uses an electric traction motor to drive the rear wheels and the diesel engine to drive the front wheels, while also having an electric motor to be used for engine start/stops and mild charging. This powertrain can be seen in Figure 22.

Figure 22: Series/Parallel Through the Road Autonomie Diagram

The energy consumption and emissions of these architectures was evaluated in both charge sustaining and charge depleting operation over the EcoCAR 2 four-cycle test. The four-cycle test includes the 505 and the HWFET, and the US06 drive cycle that has been split into city and highway components. The specific weighting for each drive cycle can be found in Table 11.

Table 11: EcoCAR 2 Four Cycle Blend Weighting Factors

Drive Cycle	505	HWFET	US06 City	US06 HW
Weight	.29	.12	.14	.45

The EcoCAR 2 four-cycle test is weighted 57/43 highway driving to city driving. This differs from the Corporate Average Fuel Economy (Cafe) standard, which is weighted 45/55 highway to city driving. This blend also weights the US06 driving schedule more than the HWFET, which more accurately represents modern highway driving.

In order to evaluate energy consumption, a UF correction was used in accordance with the Society of Automotive Engineers (SAE) J1711 standard (71). The UF is based on

collected data that represents national driving trends, and it is used to account for the

usability of various charge depleting ranges (71). The relationship between UF and

charge depleting range can be seen in Figure 23.
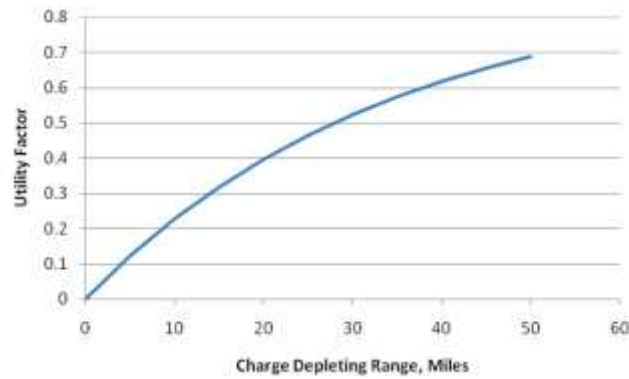
Figure 23: Utility Factor VS charge depleting range (72)

The energy consumed in the charge depleting mode was calculated using Equation 6.

Equation 6

$$EC_{CD} = EC_{fuel_{CD}} + EC_{elec_{CD}}$$

Charge sustaining energy consumption was corrected to account for any additional

depletion of the battery during the drive cycle Equation 7;

Equation 7

$$FC_{corr_{SOC}} = \frac{m_{fuel} + ((\Delta SOC/_{0.25})/LHV_{fuel})}{dist_{cycle}}$$

The corrected charge sustaining energy consumption was calculated using equation 8.

Equation 8

$$EC_{CS} = FC_{corr_{SOC}} * LHV_{fuel}$$

Then all of the weighted charge depleting and charge sustaining energy consumptions were weighted and summed. These final sums were used in equation 9 to determine the UF corrected energy consumption of each vehicle.

Equation 9

$$EC_{UF} = EC_{CD_w} * UF + EC_{CS_w} * (1 - UF)$$

The results from the Autonomie simulations are summarized in Table 12. The pre-transmission architecture was determined to have the lowest Energy consumption and GHG emissions. All of the powertrains have similar mass and CD range, the largest difference in energy consumption comes from fuel use during charge sustaining operation.

Table 12: Autonomie Powertrain Architecture Simulation Results

Metric	Series	S/PTTR	PRTX
EC (Whr/km)	339.91	421.03	334.36
0-60 mph (s)	8.5	7.3	7.6
Gradability	10% @ 60mph	10% @ 60mph	10% @ 60mph

The pre-transmission and the series PHEV had very similar energy consumptions on the 4 cycle Autonomie simulations. Having the engine decoupled from the road allows for the series to have two-degrees of freedom in engine operation. Both engine speed and torque can be controlled independently to achieve a desired power. This allows the engine to operate along the minimum brake specific fuel consumption (BSFC) line. However the PRTX does not have the added conversion losses between the generator and the engine. Engine operation of the series PHEV during the HWFET drive cycle can be seen in Figure 24.
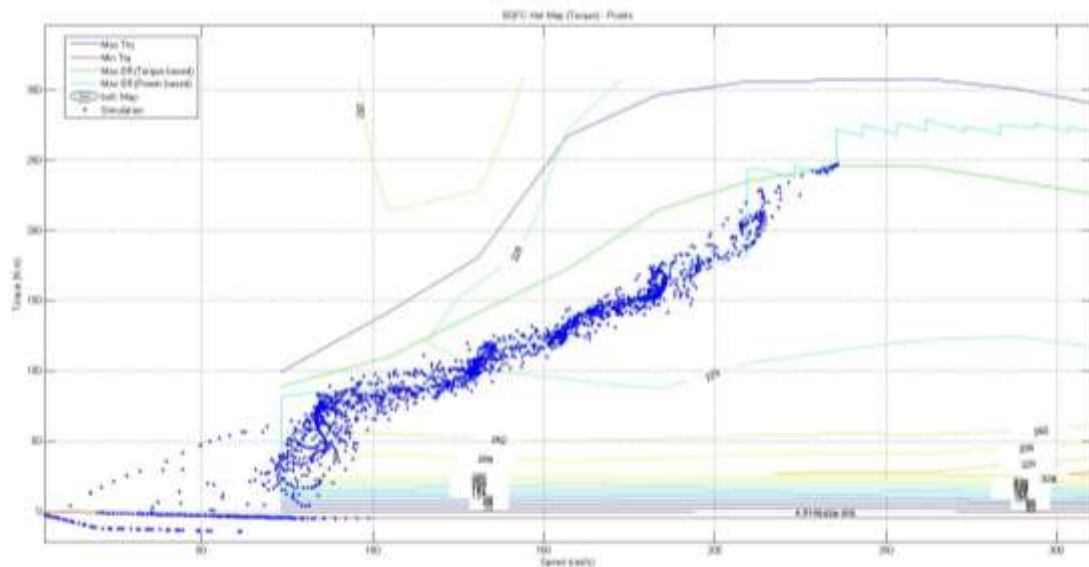
Figure 24: Series PHEV Engine Use

The engine is coupled to the wheels in the other two vehicle architectures and engine operation cannot be controlled. The engine operating points used by the S/PTTR architecture is shown in Figure 25. The addition of an e-CVT to the pre-transmission

architecture could greatly reduce engine losses and could further improve its vehicle level efficiency (73).
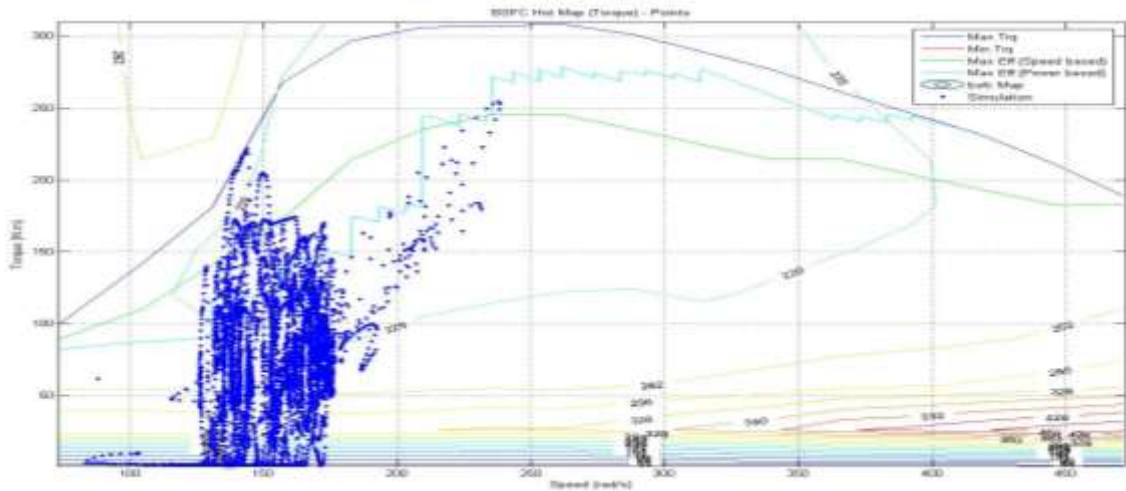
Figure 25: P/STTR PHEV Engine Use

2.4   Mechanical Integration

 A space claim analysis was conducted by William Townsend Hyatt to assess the mechanical feasibility of integrating each PHEV powertrain into the Malibu chassis. The space claim analysis evaluated the required mechanical modifications and the effects of these modifications on consumer acceptability.

The series and pre-transmission architectures (Figure 26, Figure 27) were able to have their full powertrain located in the engine bay.
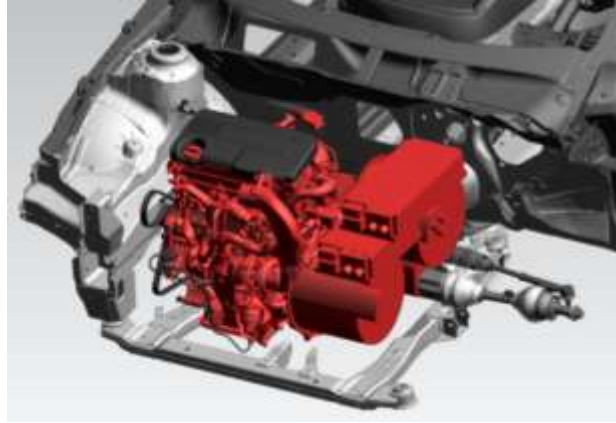
Figure 26: Series Powertrain (74)

The series powertrain has the generator, traction motor power electronics, engine and transmission located in the engine bay. The engine and generator set, as well as the traction motor and transmission are collinear to each other allowing for robust mechanical couplings.
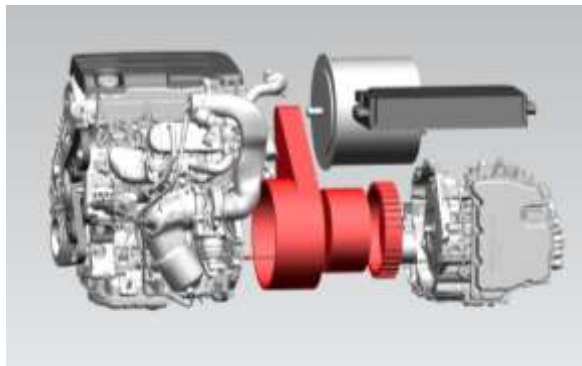
Figure 27: Pre-Transmission Powertrain (74)

The pre-transmission architecture has the least number of components to package in the engine bay. The pre-transmission architecture requires the separation of the engine and transmission in order to fit the clutch and belt assembly. This separation causes a high

risk for mechanical interference with the limited lateral space in the engine bay. The pre-transmission architecture also requires the motor to be offset from the engine and transmission. Transferring torque from the offset mounting location relies on a high-torque belt or chain drive system.

Keeping the powertrain inside the engine bay allows for the energy storage system (ESS) to be located below the cargo space as shown in Figure 28. This mounting location retains the stock cargo space while keeping the center of mass low.

Figure 28: Series & Pre-Transmission ESS (74)

The traction motor for the through the road architecture is mounted to the rear sub-frame as shown in Figure 29.
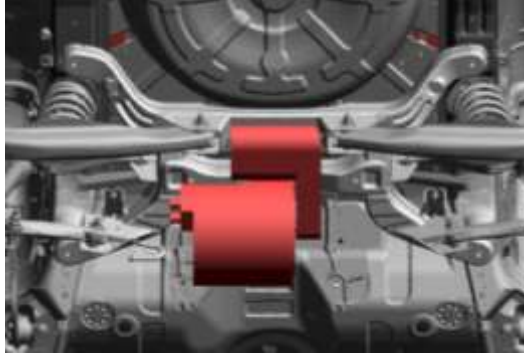
Figure 29: Through the Road Rear Drive Unit (74)

This mounting location reduces the underbody space available for the ESS. As a result the ESS is located inside the cargo space as shown in Figure 30. This causes a severe reduction in cargo space, and consumer acceptability.
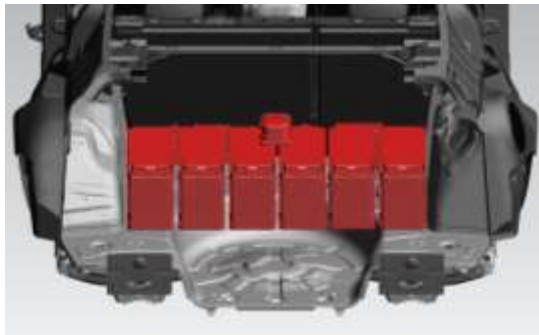
Figure 30: Through the Road ESS (74)

2.5   Final Selection

From the results of the emissions, energy consumption, and space claim analysis the series architecture was chosen to be favorable over both the pre-transmission and series/parallel through the road configurations presented in this paper. The series

architecture uses a Remy HVH 250-90P traction motor coupled to a GKN fixed gear

transaxle to drive the wheels at all times. A HVH 250 90S generator is coupled to a 1.7L

GM diesel engine using B20 bio-diesel to generate electricity to maintain the battery

SOC. Energy is stored on board the series PHEV using an A123 15s X 3p Li-ion battery

pack. The final Series PHEV architecture can be seen in Figure 31.
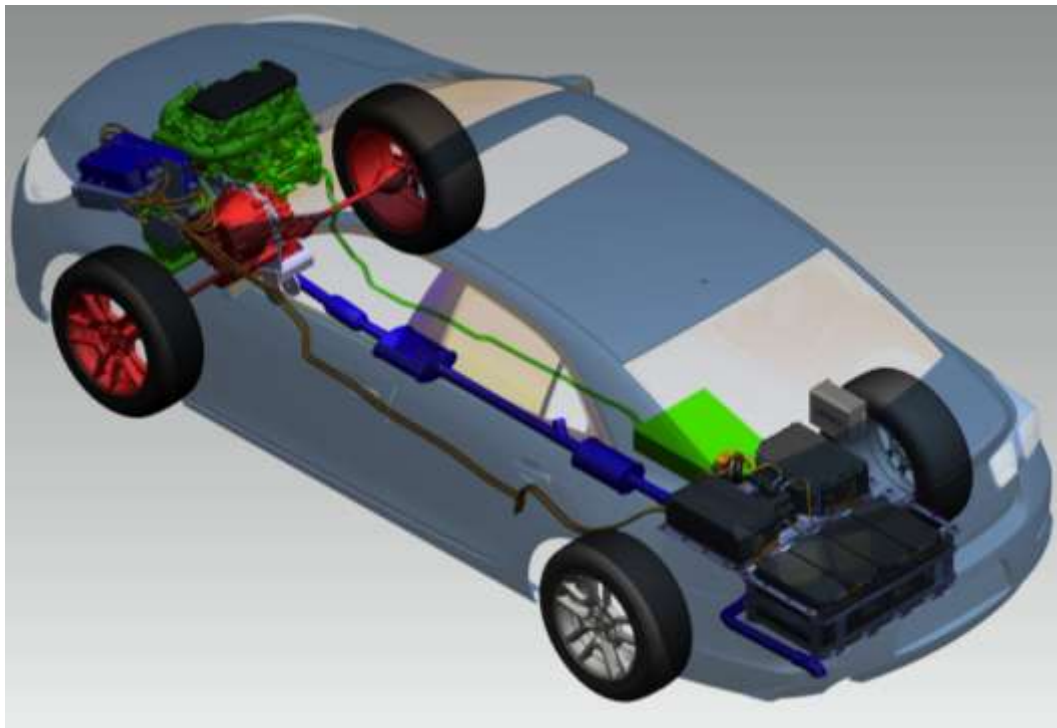
Figure 31: Final Series PHEV Architecture

The series architecture and PRTX energy consumptions were weighted equally because

the results were deemed to be with-in the modeling uncertainty of Autonomie. This

uncertainty is due to the variations in control parameters between the two architectures.

The additional mass and rotational inertia with the series/parallel through the road

architecture caused it to have the highest energy consumption. The series architecture had

the most feasible space claim analysis due the powertrain being located entirely in the engine bay, the robust torque couplings, and minimal interference between the energy storage system and cargo space. The series architecture was also selected due to its ability to maintain the same levels of drivability and performance during both charge sustaining and charge depleting operation. These results are summarized in Table 13.

Table 13: Powertrain Architecture Decision Matrix

Metric	Series	PRTX	PTTR
Consumer acceptability	1	2	3
Energy consumption	1	1	2
Mech. Integration	1	3	2
Performance	3	2	1
WTW GHG	1	1	2
Total	7	9	10

These results represent a small subset of possible vehicle configurations and hardware. Due to the sensitivity of PHEV energy consumption to control strategies a more in depth study would need to be conducted to make broader conclusions about PHEV architecture performance. Autonomie is not suited for this type of simulation, as more control over vehicle and control parameters are required to fully optimize each design.

3 HIL Development

The series PHEV architecture was selected using Autonomie simulations but it was
necessary to develop a higher fidelity, real time capable, vehicle plant model for
controller development. While Autonomie has the capability to generate real-time
capable vehicle models, the fidelity of these models is better suited for high-level
powertrain evaluation rather than detailed controller design. The model will be tested in
Software in the Loop (SIL), and Hardware in the Loop (HIL) environments to ensure its
future functionality with the vehicle.

3.1 Hardware Overview

The plant model was executed on a dSPACE simulator system. The HIL testing used the
dSPACE midsized simulator, a dSPACE MicroAutoboxII (MABX), and a dSPACE
RapidPro system. The hardware used for HIL development is summarized in Table 14.

Table 14: HIL Hardware Overview

Supervisory Controller	Power Staging	HIL
dSPACE MicroAutobox II 1401/1505/1507	dSPACE RapidPRO	dSPACE midsize Simulator ds1006/ds2202/ds4302

The dSPACE midsized simulator was the primary hardware tool used to simulate the vehicle. The midsized simulator is a rack that houses the processor and I/O boards. This rack has a ds1006 processor board, a ds2202 I/O board, and was upgraded with a ds4302 CAN board. This rack has quad core processor capable of running computationally intensive models in real time. With the two I/O boards the HIL can simulate 6 CAN channels, serial communication, digital signals, and analog signals.

A MABX was chosen as the primary hardware for the supervisory controller. The MABX will act as the primary controller hardware inside the ERAU vehicle. All control algorithms run in real time on the MABX were tested using the HIL system, and will later be validated on the vehicle. The dSPACE RapidPro is used in conjunction with the MABX to control relays and high current devices. The hardware interaction between components is shown in Figure 32: HIL Diagram.
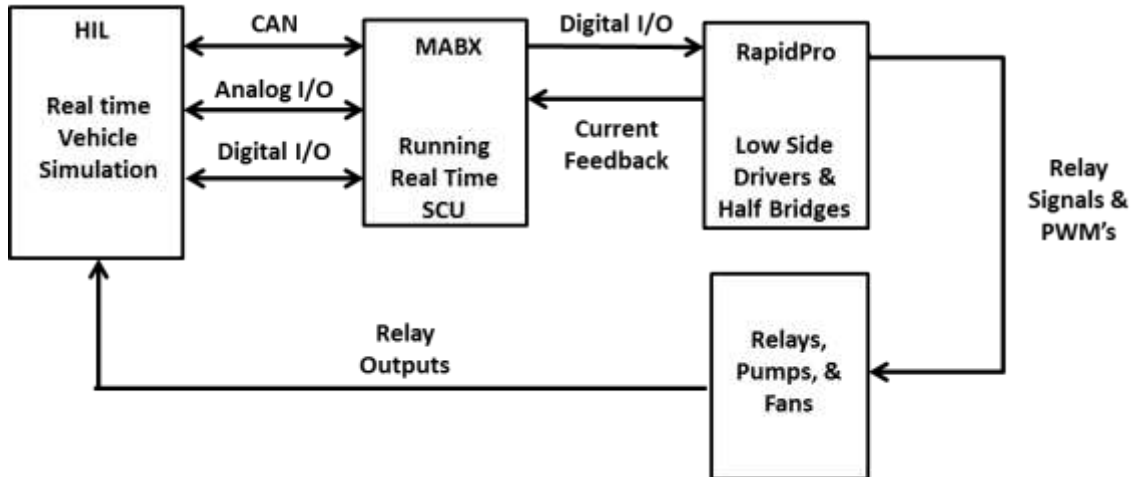
Figure 32: HIL Diagram

3.2 Plant Model Development

In order to reduce the development time of higher fidelity models the dSPACE

Automotive Simulation Models (ASM) were used. The ASM library contains Simulink

block-sets for standard automotive powertrain components. These block-sets are

generalized models with configurable parameters. The parameters are configured using

the dSPACE Model Desk GUI, which manages the initialization files for the model.

GM and dSPACE developed a parameter set that represented the GM LUD engine that

was chosen for the series PHEV. This model was donated as part of the universities

involvement in EcoCAR2: *Plugging into the Future*. The donated LUD model was used

as the base model for the development of the series PHEV model. The donated model

included a parameterized diesel engine model, longitudinal vehicle dynamics, and

environment parameters including a PI driver controller. The ASM electric component

library was used to add the hybrid components into the stock diesel vehicle model. The

individual components and library block sets are summarized in Table 15: Plant Model

Components.

Table 15: Plant Model Components and Source

Component	ERAU Function	Source
GM LUD Diesel	Engine	dSPACE Donated ASM Model
Remy HVH 250 90p	Traction motor	ASM Electrical Library PMSM Motor
Remy HVH 250 90s	Generator	ASM Electrical Library PMSM Motor
RMS PM 150	Inverter for traction motor	ASM Electrical Library 3 Phase Inverter
RMS PM 100	Inverter for generator	ASM Electrical Library 3 Phase Inverter
A123 15s-3p x6	Energy Storage System	dSPACE Donated ASM Model 3 Phase Inverter
GKN fixed gear transaxle	Transmission for traction motor	ASM Library Transmission
SCR Catalyst	Exhaust After-treatment	EcoEagles based on research from (Nieuwstadt & Upadhyay, 2002)

Each component was first parameterized in Model Desk from manufacture data sheets.

Then component level functionality was validated before being integrated into the full

PHEV model.

3.2.1 Modeling Remy HVH Motors

In order to have a model that accurately represents vehicle performance the Remy HVH

250-P model must be an accurate representation of motor performance. The ASM

Permanent Magnet Synchronous Machine (PMSM) block-set was used as the basis for

the motor models. The analytical PMSM model uses the Park-Clark transformation to

convert the three phase voltages from the a,b,c frame to the orthogonal, quadrature (q),

direct (d), reference frame. Using the flux linkage and voltage functions (Equation 10

Equation 11 (75)) the d and q currents can be found.

Equation 10

$$U_d = \frac{d\emptyset_d}{dt} - \omega * p * \emptyset_q + R_s * i_d$$

Equation 11

$$U_q = \frac{d\emptyset_q}{dt} - \omega * p * \emptyset_d + R_s * i_q$$

The flux linkage function relates the inductance current to the magnetic flux through the stator coils. The flux linkage functions are shown in Equation 12 and Equation 13. For the linear inductance model the d and q inductances are constant. The d and q inductance chosen for the linear model represent the inductance at nominal d and q currents.

Equation 12 (75)

$$\emptyset_d = L_d * i_d + \emptyset_f$$

Equation 13 (75)

$$\emptyset_q = L_q * i_q$$

The electromagnetic torque is found by using the torque equation shown in Equation 14 (75). The torque of the motor is a function of the number of pole pairs, rotor flux, inductances, and current.

Equation 14

$$T = m * p(\emptyset_d * i_q - \emptyset_q * i_d) = m * p(\emptyset_f * i_q + (L_d - L_q)i_d * i_q)$$

The d and q current can be solved for by substituting the flux linkage functions into the voltage equation as shown in Equation 15 and Equation 16. The model uses a mixed Tustin-Euler discrete integration to solve for the current.

Equation 15

$$\frac{di_d}{dt} = \frac{U_d - \frac{dL_d}{dt} * i_d + \omega * p * \emptyset_q - R_s * i_d}{L_d}$$

Equation 16

$$\frac{di_q}{dt} = \frac{U_q - \frac{dL_q}{dt} * i_q - \omega * p * \emptyset_d - R_s * i_q}{L_q}$$

The PMSM motor was parameterized using the test data provided by Remy as can be seen in Table 16.

Table 16: PMSM Parameters

Ld [H]	Lq [H]	Rs [Ω]	Nominal Current [A]	Pole Pairs	Φf [Wb]
15 E^{-5}	15 E^{-5}	0.01	180	5	0.12

Motor functionality was initially tested decoupled from the vehicle using only the rotor inertia, and a constant voltage supply. Maximum power curves were generated using a simulated speed ramp. By applying the maximum *Iq* command to the PMSM controller with a constant load torque of 100 Nm, the motor model was accelerated to maximum speed at maximum torque. This test was used to benchmark key model behavior such as; base speed, maximum torque, continuous torque, peak power, and continuous power. Base speed occurs when the amplitude of the phase voltage is equal to the bus voltage.

Motor speed is extended beyond the base speed by using a flux weakening motor control algorithm, and increasing current in the direct axis. The results from the ramp-up test can be seen in Figure 33, and Figure 34.
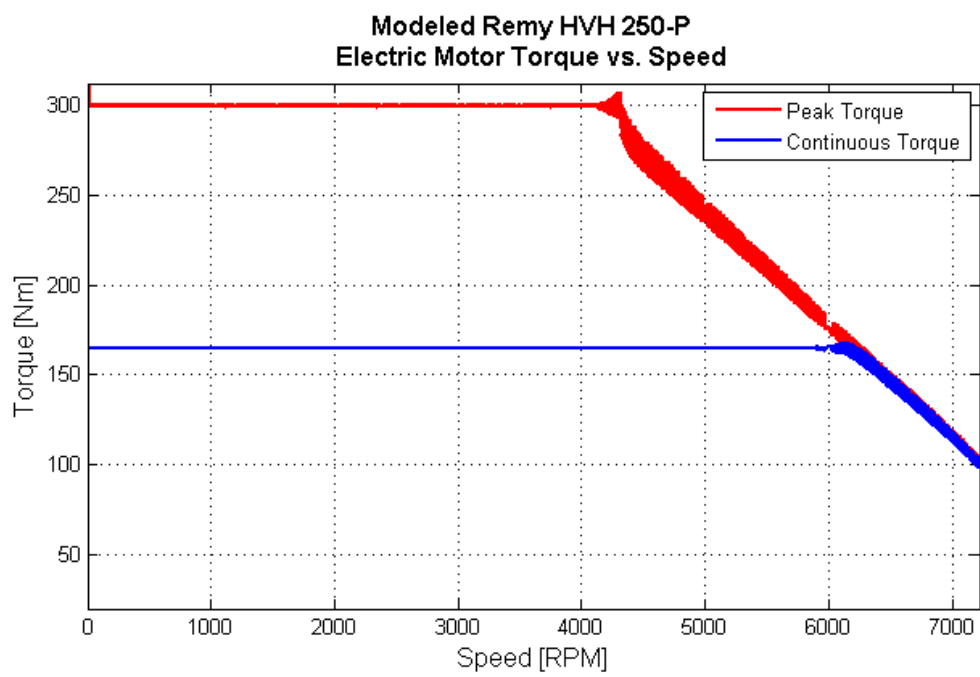
Figure 33: Remy HVH 250-9 Modeled Torque vs. Speed
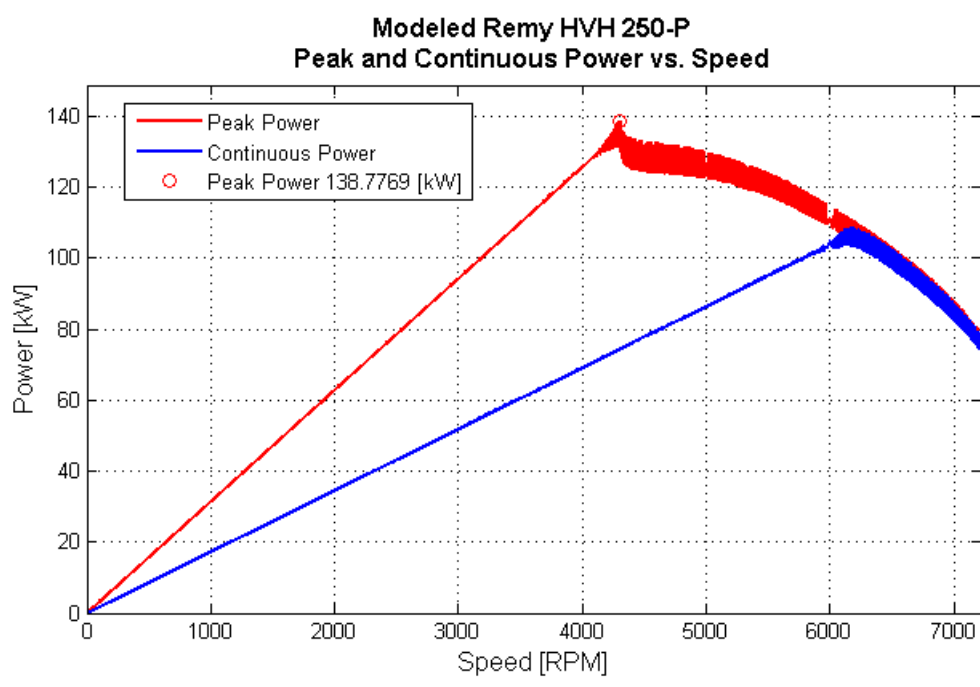
Figure 34: Remy HVH 250-P Modeled Power vs. Speed

The modeled bus voltage was 8.75% less than the bus voltage used in by Remy. This

reduced bus voltage should result in a linear reduction in motor performance. The speed

characteristics of the motor are much lower than expected, but motor torque is higher

than expected. Motor performance is especially inaccurate during flux-weakening. The

modeled motor performance is summarized in Table 17.

Table 17: Modeled Motor Performance Results

Performance Characteristic	Modeled at 292V	Actual at 320V	Percent Diff [%]
Base Speed [RPM]	4200	5000	16
Maximum Speed [RPM]	7200	10000	28
Peak Torque [Nm]	300	311	3.5
Continuous Torque[Nm]	165	165	0
Peak Power [kW]	139	145	4.1
Continuous Power[kW] @ 5000-1000 RPM	N/A	85	N/A

The reduced motor torque and top speed adversely affects the vehicles top speed

performance. This limited performance makes the model incapable of completing the

high velocity (greater than 100 km/h) portions of US06 drive cycle.
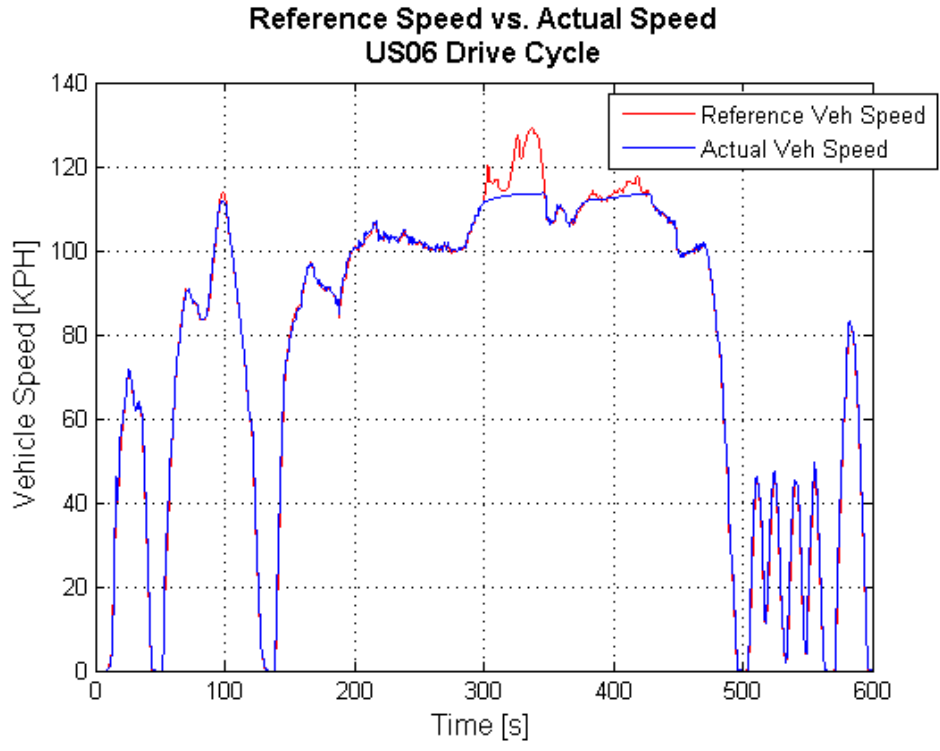
Figure 35: Vehicle Velocity on US06 Drive Cycle

At the motors rated maximum speed of 10,000 RPM the vehicle should be able to achieve

the speed required by the US06 drive schedule. The top speed of the vehicle was

calculated using Equation 17.

Equation 17

$$Speed_{max} = \frac{RPM_{mot} * 2 * \pi}{G_r * 60}$$

The theoretical top speed top speed was determined to be 132.08 kph, slightly greater

than the top speed of the US06 driving schedule.

Table 18: Theoretical Vehicle Top Speed

Vehicle Top Speed [kph]	US06 Top Speed [kph]
132.08	129.23

The trends of the motor performance during flux weakening are inaccurate. During flux-weakening the continuous torque vs. speed curve is too steep, and has the wrong inflection. The slope of the continuous torque vs. speed curve should be approximately linear after the base speed. Instead the slope of the torque-speed curve is almost identical to the peak torque-speed curve. The non-linear slope of the continuous torque-speed curve causes the modeled motor to have no continuous power region. The high torque oscillations during flux weakening are also an indication that the model is not operating properly. It was determined that the model represented the general motor characteristics well enough to integrate it into the full vehicle model but needs refinement. The same model was used represent the HVH 250-90S generator. The current limits were scaled to represent the generators torque capabilities.

The motor inaccuracies could be caused by the linear inductance assumptions or control errors during flux weakening. The models accuracy could be improved by using a non-linear inductance model. The non-linear ASM model uses, generic, normalized inductance tables that were generated from finite element models. The normalized ASM inductance can be seen in Figure 36 and Figure 38.
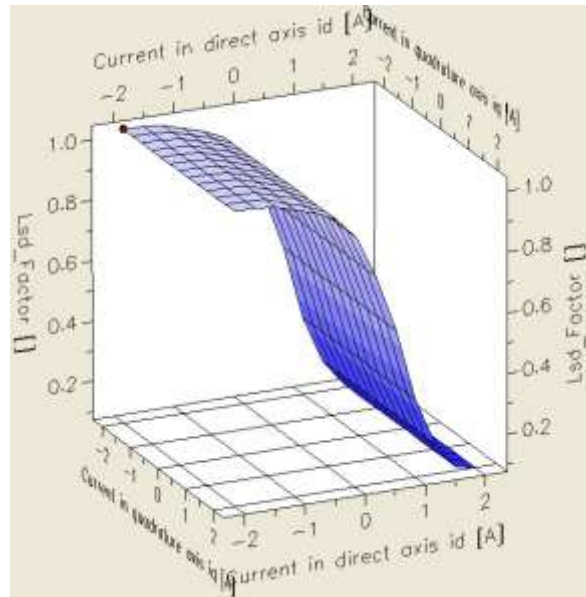
Figure 36: ASM Direct Axis Non-Linear Inductance

The ASM tables are based on the input values for the nominal current and inductance.

The ASM tables are based on the assumption that the inductance for a given primary axis

current is constant for all currents in the orthogonal axis. For example d axis inductance

is constant for all q axis currents. This differs from the trends in the data provided by the

manufacturer as shown in Figure 37 and Figure 39.
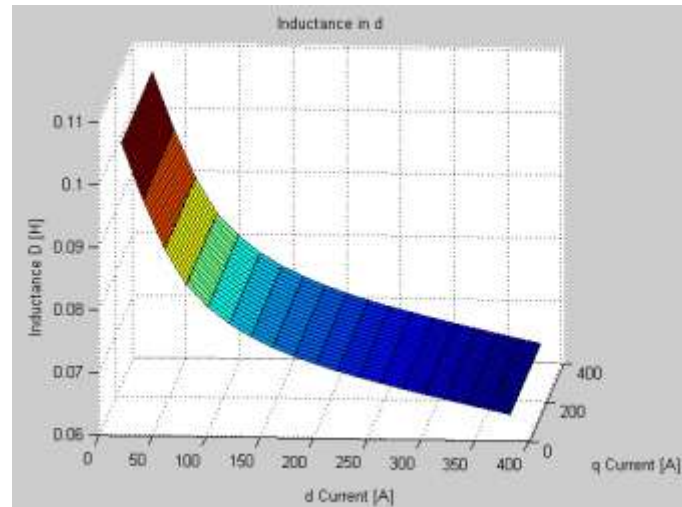
Figure 37: Direct Axis Non-Linear Inductance

The inductance data provided by the manufacturer provides d and q axis inductance as a function of the axis current and control angle. Control angle is the angle measured from the q axis of the resultant vector from summing the d and q current vectors. Therefore in the data provided by the manufacturer the inductance is a function of both d and q current. A data set equivalent to the ASM dataset can be generated by using the using only the 45° degree control angle data and projecting it along the orthogonal axis.
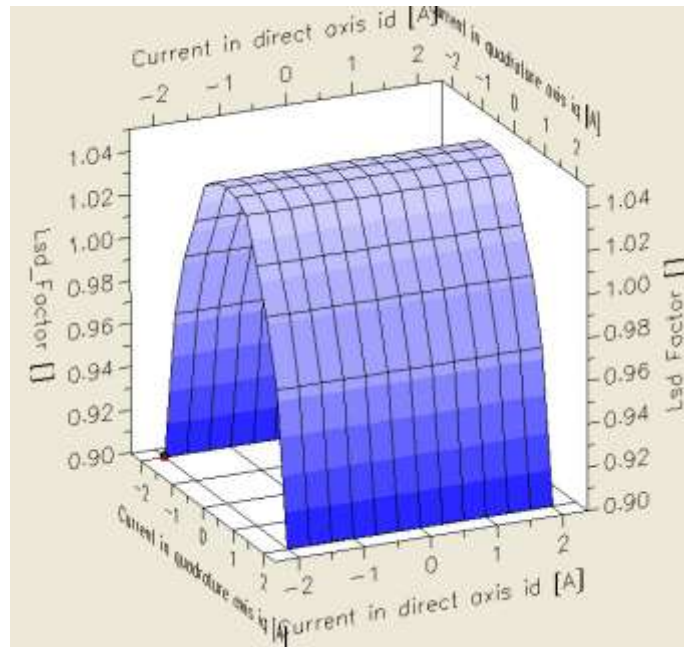
Figure 38: ASM Quadrature Axis Non-Linear Inductance

By comparing the data from the normalized ASM models, and the data created from the

manufacturer data it is clear that the trends are very different. Manufacturer data was not

provided for negative currents but if the inductances were mirrored in the negative

direction the inflections would not match the trends seen in the ASM data.
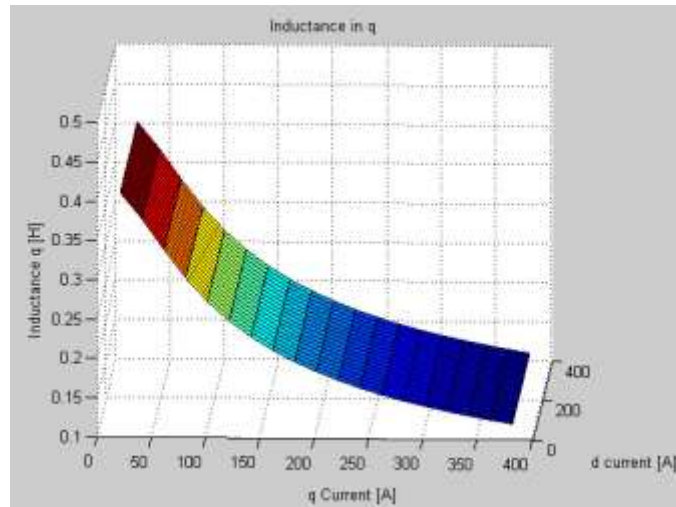
Figure 39: Quadrature Axis Non-Linear Inductance

This difference in inductance trends could be due to the difference in motor layouts. The

Remy motor is an interior permanent magnet structure while the ASM model data could

have been generated from an FEA analysis of a surface permanent magnet motor. Interior

permanent magnet motors have higher air gap flux densities than those of surface

permanent magnet designs (76). Due to these differences future improvements to the

model should use the non-linear inductance data provided by Remy. The ASM model

should be modified to include look up tables for q and d inductance based on q and d axis

current and control angle.

3.2.2 1.7 L Diesel Engine

The 1.7 L diesel engine model used was parameterized by GM and dSPACE and

provided as part of the EcoCAR competition. The model parameters were unmodified but

stand-alone tests were performed to evaluate the modeled engine performance. The

manufacturer did not provide empirical performance data for the engine, so the

parameterized model was used as a primary indication of engine performance. To

benchmark the engines performance simulated dynamometer tests were run. First a wide

open throttle (WOT) acceleration test was run to determine maximum engine torque and

powers. It was determined that the engine produced a maximum torque of 290 Nm, and

maximum power of 90 kW. The results from the WOT engine test can be seen in Figure

40.
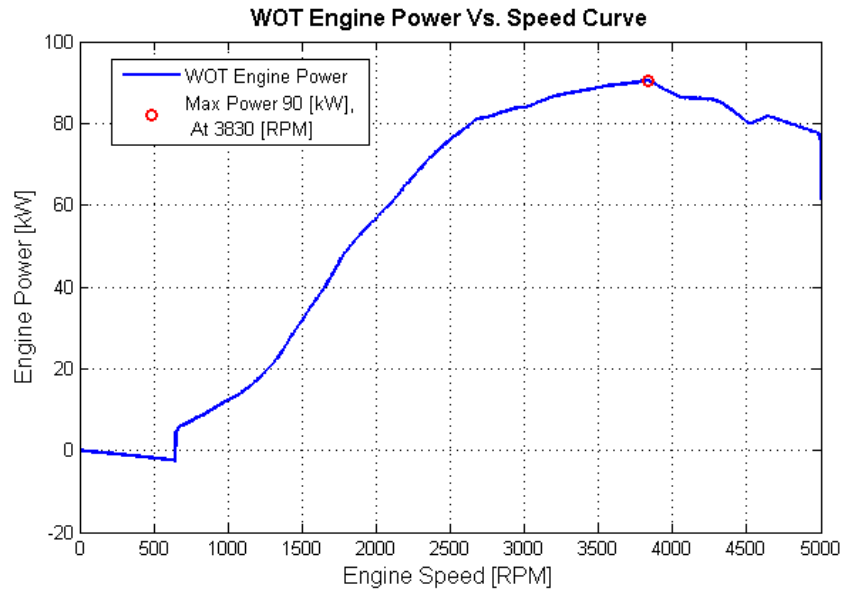
Figure 40: Wide Open Throttle Engine Power vs. Speed Curve

After the WOT test, additional simulated dynamometer tests were used to generate an

engine that spans the entire operating range. The simulated dynamometer tests were

conducted at 10% throttle and speeds ranging from 0 to 5,000 RPM. Torque, speed, and

fuel flow rates were recorded during each simulation. The simulated engine data was

used to generate a spline map, as can be seen in Figure 41.
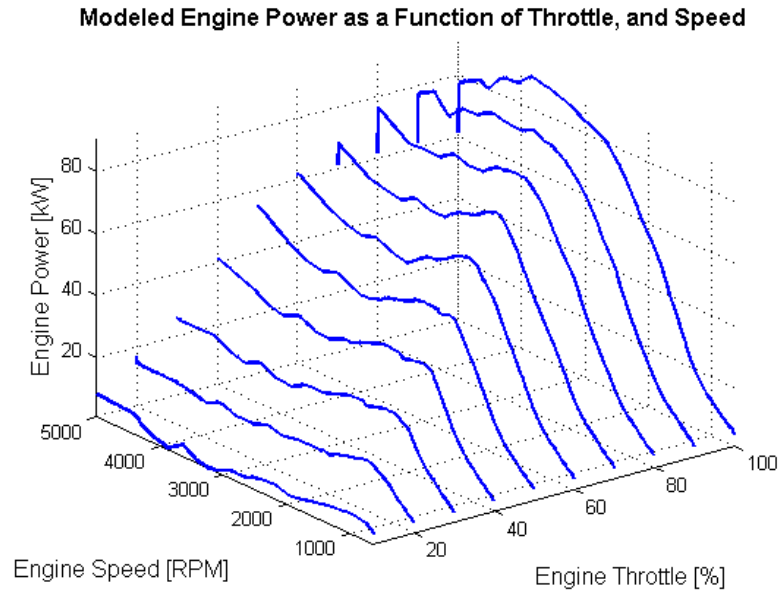
Figure 41: Simulated Engine Performance; Torque as a Function of Speed and Throttle

The engine data splines were then used to generate a three dimensional map on a specified grid of engine operating points. The map was generated using Matlab TriScatteredInterp function. This function performs a Delaunay triangulation of the scattered data which is then used for the interpolation on the input x,y grid (77). The engine power map generated using the TriScatteredInterp function can be seen in Figure 42.

Modeled Engine Power as a Function of Throttle, and Speed
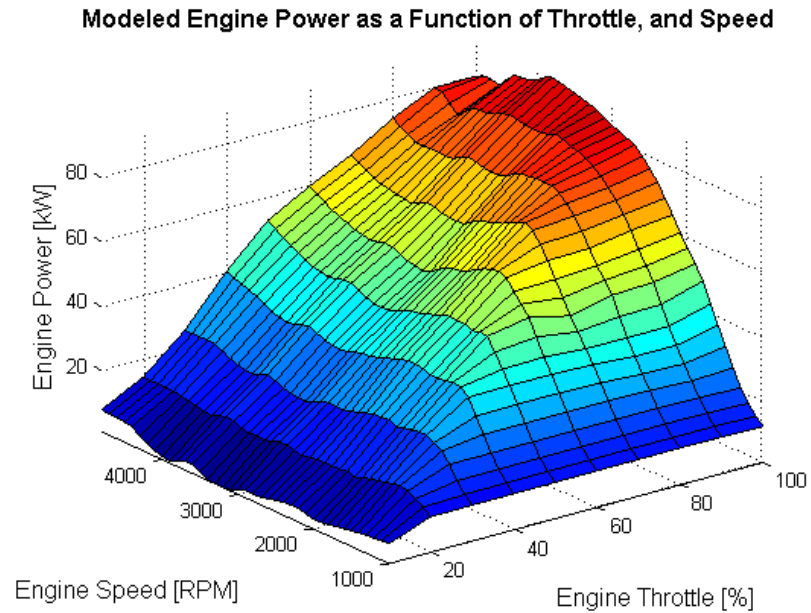
Figure 42: Simulated Engine Power Map as Function of Speed and Throttle

A brake specific fuel consumption (BSFC) map was also generated using the simualted engine data. BSFC is the inverse of efficiency, it is a measure of energy in / energy out. BSFC is measured in grams of fuel input divided by kwhr of energy out. The simulated BSFC map can be seen in Figure 43.

Brake Specific Fuel Consumption, as a Function of Throttle, and Speed

Figure 43: Model Generated BSFC map
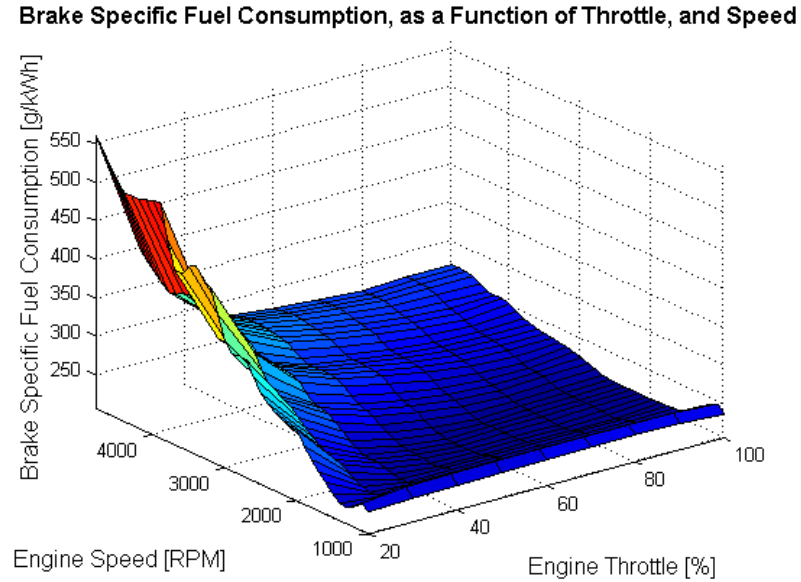
The engine power and BSFC maps were later used to develop charge sustaining control algorithms. The results of simulated engine performance tests are shown in Table 19.

Table 19 : Engine Performance Results

Performance Characteristic	Modeled at 292V DC Bus Voltage
Maximum Speed [RPM]	5000
Peak Torque [Nm] @ 2471 RPM	290
Peak Power [kW] @ 3830 RPM	90
Minimum BSFC [g/kWhr]	206.1606

3.2.3 Engine Generator Coupling

The engine and generator are directly coupled together. This connection was assumed to be rigid, therefore the speeds of the engine and generator are always equivalent. The angular velocity of the coupled engine and generator was calculated using Equation 18.

Equation 18

$$\omega = \int \frac{\tau_{gen} + \tau_{eng} + \tau_{massmod}}{I_{eng} + I_{gen}} dt$$

The angular velocity was found by integrating the angular acceleration, which was determined by summing the generator torque, engine torque, and mass modulated torque and dividing by sum of the engine and generator rotational inertias. The engine torque used to find the angular velocity also includes the torque from friction. The mass-modulated torque is implemented in the ASM engine model to capture the effect of the changing crankshaft mass moment of inertia. Future model improvements should include, a generator friction model, and a switch to decouple the engine and generator dynamics to better simulate a mechanical failure in the mechanical coupling.

3.2.4 A123 15S 3P X 6

The A123 battery model was parameterized and donated by dSPACE. The donated A123 model also included a battery control module, and contactor models. The A123 battery model was implemented directly into the PHEV model for testing. The currents from the traction motor and generator were summed at the input junction to the battery. Drive cycle simulations were used to compare the modeled voltage characteristics to the manufacturer specifications. The results from the US06 drive cycle can be seen in Figure 44.
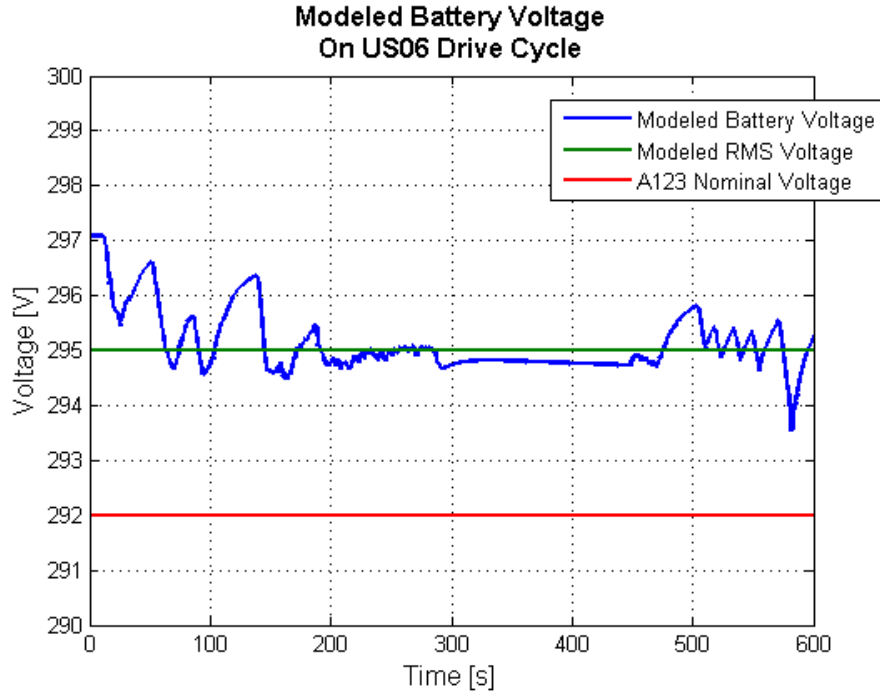
Figure 44: Simulated Nominal Battery Voltage

The RMS voltage was found to be 295 V over the US06 drive cycle when ran with an initial SOC of 80%. The model has only a 1% difference from the rated nominal voltages provided by A123. These simulated battery performance results are summarized in Table 20.

Table 20: Modeled Battery Results

Performance Characteristic	Modeled	A123	Percent Diff [%]
Nominal Voltage [V]	295	292	1.03

Additional battery characteristics that should be verified are, the total energy capacity, and the battery performance varying thermal loads.

3.2.5 Emissions and SCR Catalyst

An empirical model was used to generate the upstream pre-catalyst emissions. The

empirical map was created from dynamometer tests of similar GM diesel engine since no

test data was released for the 1.7L GM engine. A look-up table for the empirical

emissions data was added to the model. The look-up table interpolates parts per million

(ppm) of NOx as a function of engine speed, and throttle position. The table can be seen

in Figure 45. This look-up table can be updated to represent the 1.7 L GM engine when

dynamometer data is released.
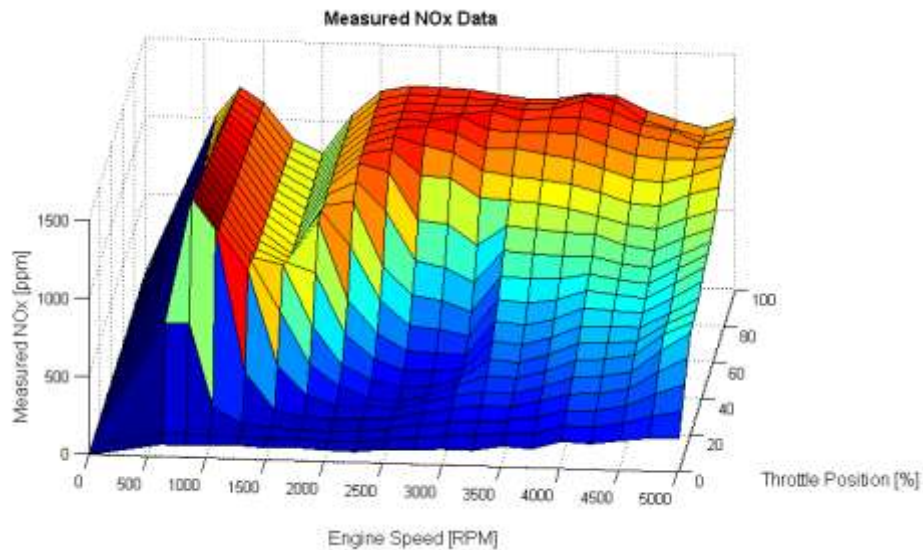
Figure 45: NOx Map for Upstream Sensor

In order to simulate the downstream NOx sensor a plant model for the catalyst was

created. The model was a non-linear single input single output (SISO) state space model

with three states. The three states are, gaseous NOx concentration (c_{NO}), gaseous NH3

concentration (c_{NH3}), and percent surface coverage (θ). A diagram of the catalyst model can be seen in Figure 46.
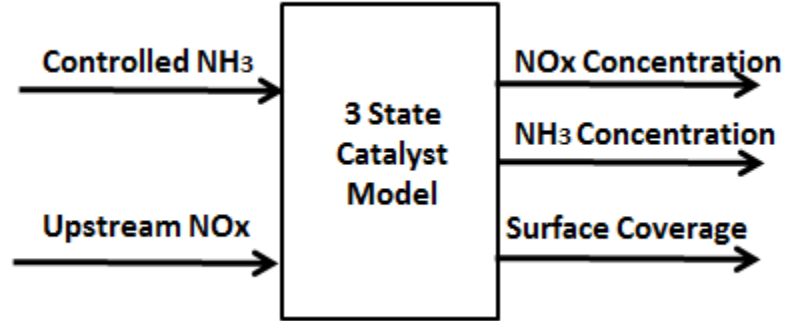
Figure 46: Catalyst Model Diagram

The catalyst model is based on research conducted by Devesh Upahyay, and Michiel Van Nieuwstadt and simulates the reactions of NOx and NH3 inside the catalyst. The catalyst reaction has four phases, absorption, reduction, desorption and oxidation (78). The rates of the four catalyst reactions are; $\bar{R}_{ads}, \bar{R}_{red}, \bar{R}_{des}$, and $\bar{R}_{ox}$ (78). The single control input is the gaseous concentration of NH3 (c_{NH3}) the upstream gaseous NOx concentration is treated as a disturbance. The non-linear state space representation of the catalyst can be seen in Equation 19, and Equation 20 (78).

Equation 19

$$\begin{bmatrix} \dot{C}_{NO} \\ \dot{\theta} \\ \dot{C}_{NH3} \end{bmatrix} = \begin{bmatrix} -C_{NO}\left(\Theta_{SC}\bar{R}_{red}\theta\frac{F}{V_{cat}}\right) + \bar{R}_{ox}\Theta_{SC}\theta \\ -\theta(\bar{R}_{ads}C_{NH3} + \bar{R}_{des} + \bar{R}_{red}C_{NO} + \bar{R}_{ox}) + \bar{R}_{ads}C_{NH3} \\ -C_{NH3}\left(\Theta_{SC}\bar{R}_{ads}(1-\theta) + \frac{F}{V_{cat}}\right) + \Theta_{SC}\bar{R}_{des}\theta \end{bmatrix} + \begin{bmatrix} 0 \\ 0 \\ \frac{F}{V_{cat}} \end{bmatrix} U + \begin{bmatrix} \frac{F}{V_{cat}} \\ 0 \\ 0 \end{bmatrix} d$$

Equation 20

$$Y = \begin{bmatrix} 1 & 0 & 0 \end{bmatrix} \begin{bmatrix} C_{NO} \\ \theta \\ C_{NH3} \end{bmatrix}$$

Unknown catalyst parameters were estimated using a parameter optimization script

written by Dr. Marc Compere. The non-linear state space model was implemented in

Simulink using the estimated catalyst parameters as shown in Figure 47.
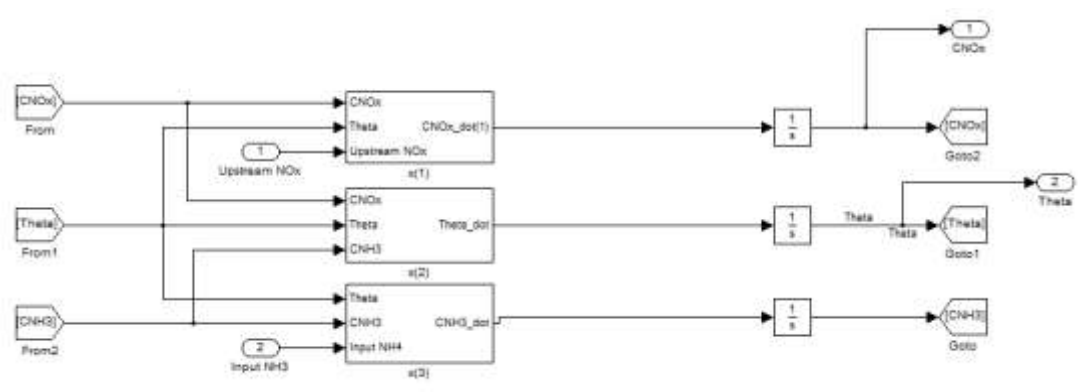
Figure 47: Down Stream Sensor Model

The catalyst model response to a step input of NH3 was validated against the results

documented in the Upahyay, and Van Nieuwstadt paper. A constant disturbance of 100

ppm NOx was input to the catalyst with a step input of 100 ppm NH3 added at 500

seconds. The catalyst response is shown in Figure 48.
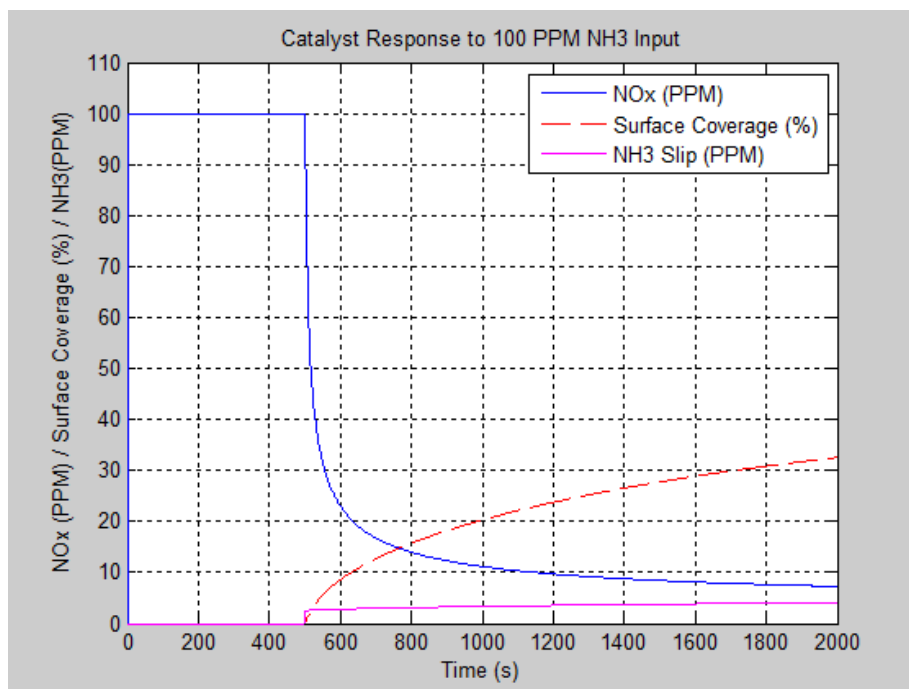
Figure 48: Catalyst Model Response to Step Input of Ammonia

The modeled NOx concentration took longer to reach 10 ppm than the reference material.

After the end of the 2000 second simulation the model also had over 30% percent surface

coverage, and 5 PPM of ammonia slip. The ammonia slip was negligible in the reference

material. The results from the catalyst model test can be seen in Table 21.

Table 21: SCR Catalyst Model Results

Performance Characteristic	Modeled	Reference	Percent Diff [%]
Response Time [s]	1100	800	37.5 %
Surface coverage [%] @ T = 2000 s	32	29	10.34
Ammonia Concentration [ppm] @ T = 2000 s	5	0	N/A

The difference between the modeled catalyst and the reference model is due to the

unknown catalyst parameters. Modeling the reaction rates for each phase of the catalyst

reaction could reduce the error between the catalyst model and the reference model. The reaction rates are governed by the Arrhenius equation shown in Equation 21 (79).

Equation 21

$$K = Ae^{\frac{-Ea}{RT}}$$

Adding the Arrhenius equation would capture the temperature based dynamics, and reduces the number of unknown parameters for the parameter optimization routine.

Accurately modeling engine emissions is difficult, but accurately predicting the total vehicle emissions is not required for initial exhaust emissions control algorithm development. Instead it is desirable captures general emission trends and catalyst dynamics with the plant model. Final controller calibrations can be done during vehicle testing.

3.2.6 Transaxle

The transmission model was modified to include the fixed gear ratio of 9.59:1. The transaxle model is used to sum traction motor torque, and equivalent road load torques.

The inertia equivalent to the vehicle mass is calculated using Equation 22.

Equation 22

$$I_v = \frac{m}{R_w^2}$$

The angular acceleration is calculated by dividing the sum of the torques by the sum of the driveline, rotor, and equivalent vehicle inertia as shown in Equation 23.

Equation 23

$$\alpha = \frac{T_m + T_{rr} + T_{aero}}{I_{car} + I_{dL}}$$

The angular acceleration is then integrated to calculate the linear vehicle speed and motor speed for the current time step.

3.3 Model Structure

Each component model was integrated into the full vehicle model to run in real-time on the HIL. The vehicle model was organized by powertrain components. In addition to powertrain components mentioned in the previous section, the vehicle model also includes subsystems for vehicle dynamics, environment, emissions and energy consumption (EEC), and Soft ECU. The vehicle dynamics, environment, and soft ECU subsystems, were included with the donated diesel model

The vehicle dynamics subsystem models the longitudinal vehicle dynamics used to calculate traction limits. The environment model contains the driver controller and ambient conditions. The Soft ECU subsystem contains the engine controller for the diesel. The energy consumption and emissions subsystem includes the catalyst model and run-time energy consumption calculations. The full vehicle model can be seen in Figure 49.
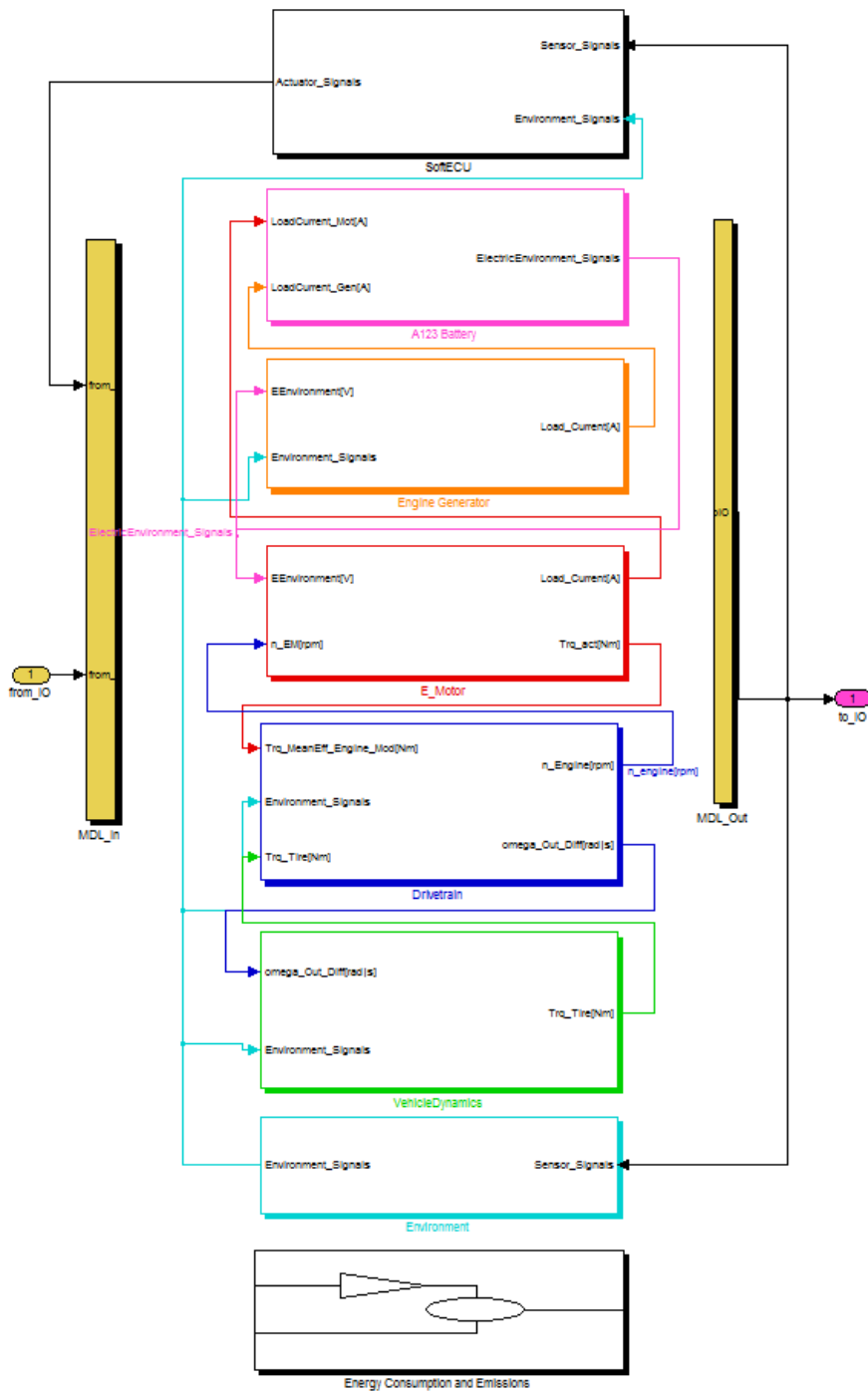
Figure 49: Plant Model Structure

3.4   Model Limitations & Tradeoffs

Computation time was sacrificed in order to achieve the desired fidelity for HIL

development using the ASM block set. The slow computation time limits the models

effectiveness for evaluating full drive cycle performance in a SIL environment. The

model could be inherently slow due to complexity and available computational resources,

or due to inefficient code structure. The Simulink model profiler could be used to

identify model elements that need to be optimized for computational time.

The motor models are limited in their ability to represent the Remy HVH 250 motors.

The model structure needs to be updated in order to accurately capture inductance

characteristics of the interior permanent magnet motor. Using the inductance tables

provided by Remy could increase motor top speed.

The battery model is limited in its ability to represent thermal effects, current limits, and

fuse dynamics. Heat rejection from the battery is not simulated. A unique phase change

cold plate will be implemented on the vehicle and should also be implemented in the HIL

model. This would allow for the development of diagnostic algorithms for the ESS

cooling system, and enable bench testing of cooling hardware. The battery has continuous

power limits that will limit the output current. These limits should be captured to

determine if the engine needs to be turned on during high power demands. The fuse

dynamics should be modeled to ensure that vehicle operation does not exceed current

limits. High risk situations for exceeding the fuses current limits include; charge

sustaining and aggressively regen-ing and attempting an engine start during high power

charge depleting operation.

3.5   Model I/O Structure

The model I/O was structured to facilitate the transition between SIL and HIL testing.

Output signals from the model are combined on a signal bus and passed to the I/O block.

All of the model outputs first go through the fault insertion subsystem. The fault insertion

subsystem allows for signals to be altered from the closed loop values before going to the

controller. This was used to validate controller fault diagnostics in both SIL and HIL

testing by injecting out of range values. The output signals then get converted from

engineering units into I/O units and are mapped to the correct hardware I/O. Hardware

inputs are first mapped from the hardware I/O and then converted into engineering units

to be used in the model. The I/O structure can be seen in Figure 50.
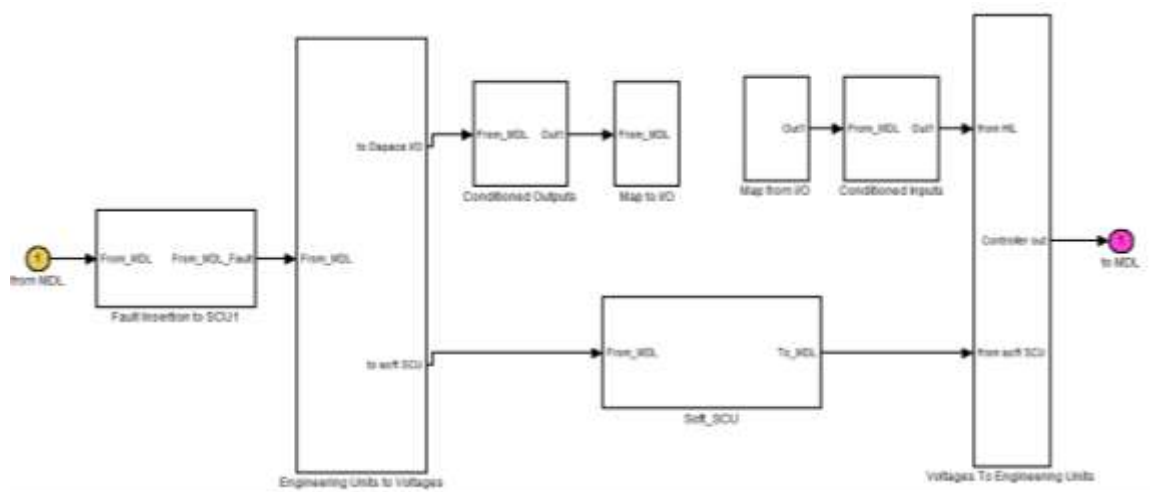
Figure 50: Model IO Structure

The input signals are routed through a SIL/HIL switch before going to the Model. This enables the model inputs to be switched between the soft SCU and hardware inputs from the physical controller during run time. The soft SCU is the SCU software contained inside the model for running SIL tests. The SIL/HIL switch allows for rapid transitions between SIL and HIL testing. The SIL/HIL switch can be seen in Figure 51.

Figure 51: Model SIL/HIL IO Switch

The I/O structure and SIL/HIL switch facilitated the development of a repeatable four step methodology for code validation. The four steps used in code validation are:

1. Algorithm unit test

    Algorithms are first evaluated in a unit test. Unit tests were used to validate algorithm functionality with open loop inputs. Unit tests were conducted in stand-alone Simulink and Matlab projects before being integrated into the SCU structure.

2. SIL test

    After an algorithm successfully completed the unit test it was incorporated into the soft SCU and ran in the SIL. SIL tests validated algorithms functionality while interacting with the close loop model dynamics.

3. Real Time SIL test

After the algorithm was tested in SIL the model was compiled and ran on the real
time system while the soft SCU was still used to control the model. Real time SIL
tests were used to validate that the code structure was real time capable, and to
validate hardware I/O before closing the loop with the physical controller.

4. HIL test

The final step in algorithm testing was the full HIL test. Full HIL tests validated
that the controller was real time capable and all hardware I/O was functional. The
SIL/HIL switch was used to transition the model inputs from the soft SCU values
to the values being reported by hardware inputs.

4 SCU Development

Safe and efficient operation of the ERAU Series PHEV powertrain is controlled by the

SCU. The SCU interprets driver commands and controls the interaction between

powertrain components through their individual control modules. To control the vehicles

powertrain the SCU sends analog, digital, and CAN signals to individual control

modules. The primary powertrain control modules that the SCU interacts with are; the

Engine Control Module (ECM), Battery Control Module (BCM), Transmission Control

Module (TCM), Motor Control Module (MCM), and Generator Control Module (GCM).

Individual powertrain control modules are responsible for the direct actuation of

powertrain hardware to achieve the SCU's inputs. The supervisory control diagram can

be seen in Figure 52.
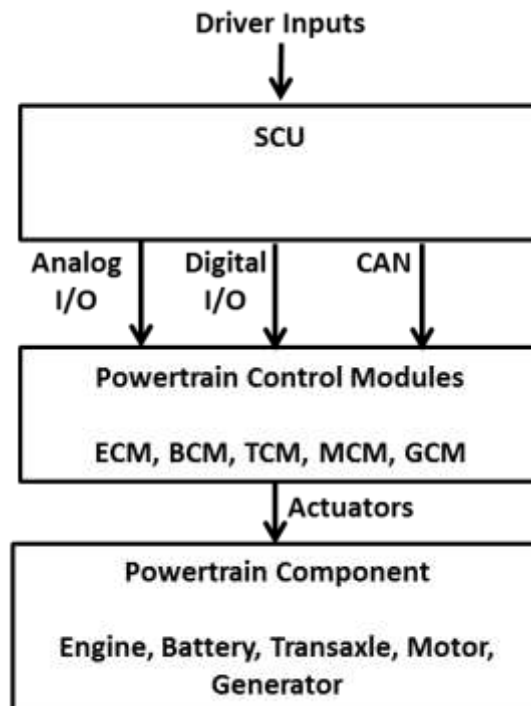
Figure 52: Supervisory Control Diagram

The SCU control structure was divided into three primary software modules; read, control, and write. This structure provides an intuitive layout that simplifies code expansion. The top-level controller structure can be seen in Figure 53.
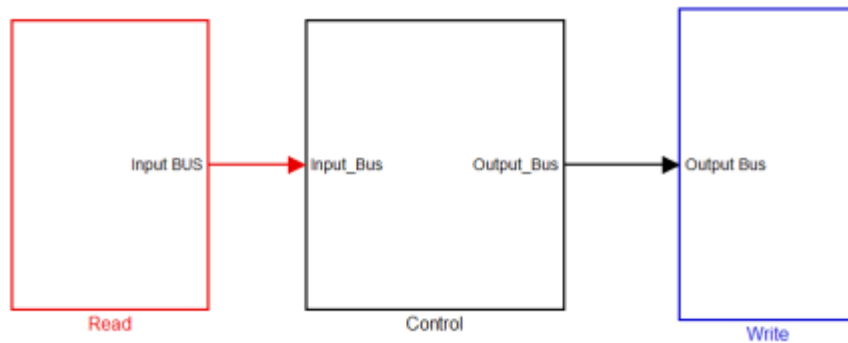
Figure 53: SCU Structure

The read module maps signals from hardware inputs and converts them to engineering units, organized by I/O type, for use in the control module. The write model first converts engineering units to I/O units and then maps each signal to the correct hardware I/O.

The control module was further subdivided into two additional software modules. These two software modules are the fault detection, and subsystem control modules. Figure 54 shows the control module structure. The control module structure was chosen to create a scalable and organized method for implementing fault detection and mitigation strategies. The control module structure can be seen in Figure 54.
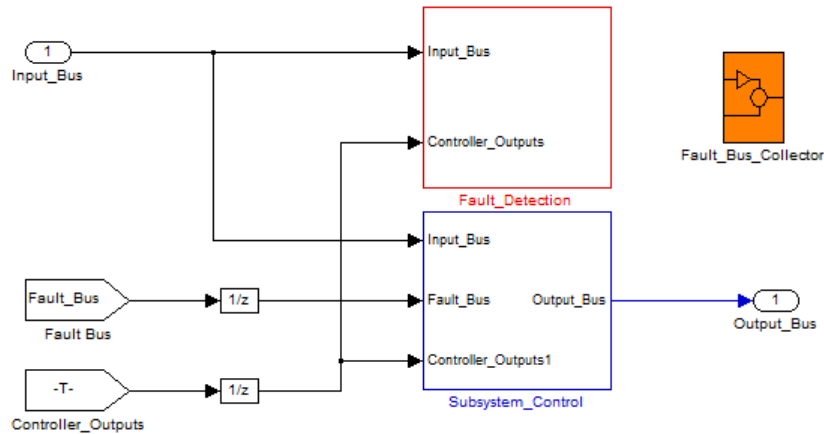
Figure 54: Fault Detection and Subsystem Control Modules

4.1   Fault Detection Module

The fault detection module contains diagnostic algorithms for safety critical systems.

Fault detection algorithms are used only for detection; these algorithms do not directly

control any powertrain components. The fault detection module receives inputs from the

hardware I/O and the control module outputs. The fault detection module is organized by

vehicle powertrain components and subsystems. Inside each component module are

subsystems for each fault, which contain the diagnostic algorithm. The fault detection

subsystem layout can be seen in Figure 55.
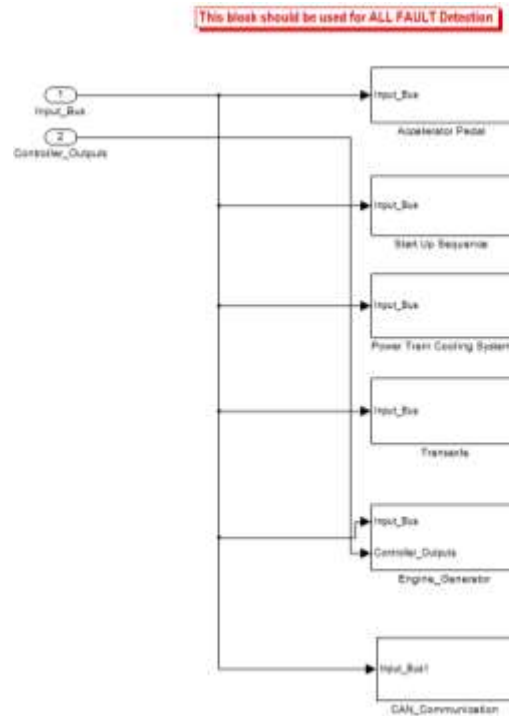
Figure 55: Fault Detection Module Structure

Fault diagnostic algorithms evaluate to Boolean to indicate the presence of a fault

condition. Each fault is then combined onto a signal bus that is sent to the control module

and to the write module. The control module uses fault signals to take remedial action,

and the write module broadcasts each fault over CAN as a Diagnostic Trouble Code

(DTC). The DTCs are used to identify faults during vehicle testing and alert the driver to

any changes in operating modes that occur in response to a fault.

4.1.1 Diagnostic Algorithms

Potential faults were identified using a Design Failure Mode and Effects Analysis

(DFMEA) and Fault Tree Analysis (FTA) techniques. DFMEA is a system engineering

tool used to identify potential failures and determine which faults are the most critical

(80). Using the DFMEA 45 faults were identified, an excerpt from the DFMEA is shown

in Table 22. FTA is a top down logic based approach to determine the root causes of a

potential failure (81). FTA analysis first identifies the undesired failure and then

determines the potential causes through Boolean logic (81).

Table 22: DFMEA Excerpt

CAN Bus Networks			Sev		Occ			Det		RPN	Criticality
	Overrun	Incorrect or Unexpected Controller Actions	7	Incorrect Time Steps / Bus at Maximum	4	Best Practices for Software Manipulation	Communication Time-Out with SCU	4	Y	112	28
	Timeout	Incorrect or Unexpected Controller Actions	7	Incorrect Time Steps / Bus at Maximum	4	Best Practices for Software Manipulation	Communication Time-Out with SCU	4	Y	112	28
	ARC Data Mis-Match	Incorrect or Unexpected Controller Actions	7	Incorrect Controller Code / Delayed Processes	4	Best Practices for Software Manipulation	Communication Time-Out with SCU	4	Y	112	28
High Voltage Interlock Loop (HVIL)											
	Shorted to 12v power	Inability to Open Contactors	10	Poor Electrical Routing / Misrouted Wire	3	Best Practices for Electrical Routing	Loss of Communication\ Inability to Close Contactors\ SCU HVIL Sensor	7	Y	210	30

The DFMEA excerpt shown in Table 22 lists four potential faults, the first three are

failures that can occur in CAN communications, and the fourth is a failure of the high

voltage interlock loop. Each potential failure is rated based on the severity, occurrence,

and detectability. Each metric was assessed on a 0-10 scale, with 10 being the worst case.

Using the severity, occurrence, and detectability scores a Risk Priority Number (RPN)

and a Criticality level were assigned to each fault. The RPN is the product of severity,

occurrence and detectability while, criticality is the product of only the severity and

occurrence (82). The criticality score is used in conjunction with the RPN to focus on

potentially dangerous failure modes regardless of their detectability.

4.1.2 Faults Validated on the HIL

The FTA was used to design diagnostic algorithms and the test cases to validate those algorithms. Ten different fault cases were fully validated through HIL testing. These fault cases belong to six unique failure types. The six tested failure types are:

1. Accelerator Pedal Mismatch: Accelerator pedal mismatch occurs when the redundant analog accelerator pedal signals from the driver do not match. The controller disables the powertrain when an accelerator pedal mismatch occurs.

2. Unintended Acceleration: An unintended acceleration is detected when the driver's foot is on the brake pedal while the controller is receiving a non-zero accelerator pedal signal. The controller shuts down the powertrain to prevent unintended accelerations.

3. Unsafe Start-Up Procedure: Start up procedure requires the driver to have the vehicle in park and their foot on the brake before the powertrain will be enabled. I

4. Loss of Component CAN Communication: Alive Rolling Counters (ARC) are used as software watchdogs to determine if a component is still communicating on the CAN network. Faults that occur include overruns, timeouts, and data mismatch. An overrun occurs when the component is sending ARC data faster than the specified rate. Timeouts occur when no ARC data is received from a component. Data mismatch occurs when the ARC sent by the component do not match the ARC expected by the SCU. The severity of the mitigation action depends directly on the component that loses CAN communication.

5. Loss of CAN BUS: Loss of an entire CAN BUS occurs when all of the components on a BUS have faults. Loss of a CAN BUS results in a vehicle shut down.

6. Input Shaft Failure: An input shaft failure occurs when the coupling between the engine and generator, or traction motor and transmission fail. When an input shaft failure occurs the powertrain components associated with the fault are disabled.

4.1.2.1 CAN Fault Example

A CAN BUS fault is presented as an example of the testing that was conducted on the HIL. A fault was injected by changing the period of the ARC being transmitted by the powertrain components on the ERAU BUS. The fault is injected at 60 seconds (figure time scales are in ms) into the drive cycle. The change in the ARC signal can be seen in Figure 56.
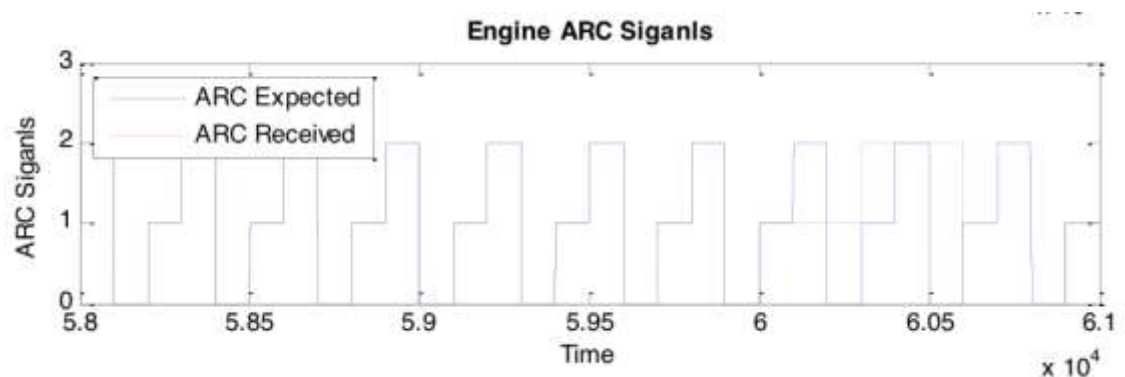
Figure 56: Engine ARC Fault Insertion

After the fault is injected the ARC received no longer matches the ARC expected by the

SCU. A timeout fault and mismatch fault are triggered because the data is transmitted

slower than expected and does not match the expected value. When the fault is detected

the fault flag is set to one, and the mitigation action is taken. The mitigating action for the

engine is to disable the fuel pump relay as can be seen in Figure 57.
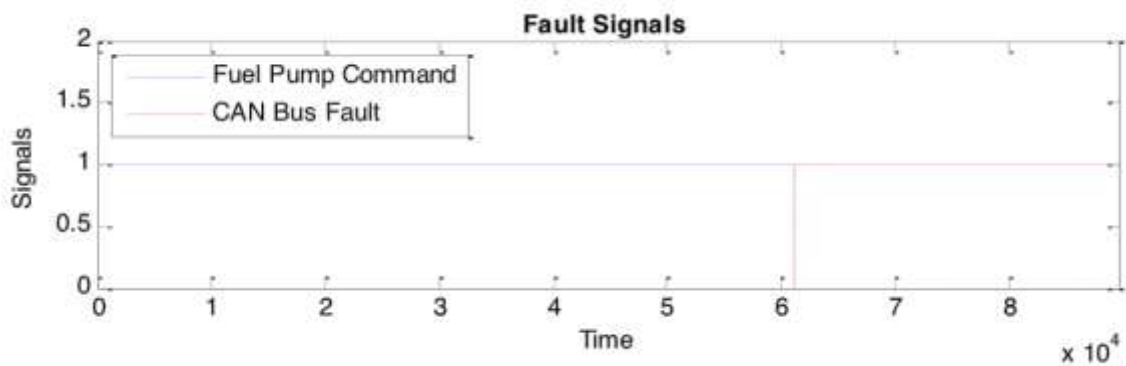
Figure 57: Fault Detection and Mitigation

The loss of the ERAU CAN bus causes a shutdown of all powertrain components. This

causes the vehicle to drop off the drive cycle as can be seen in Figure 58.
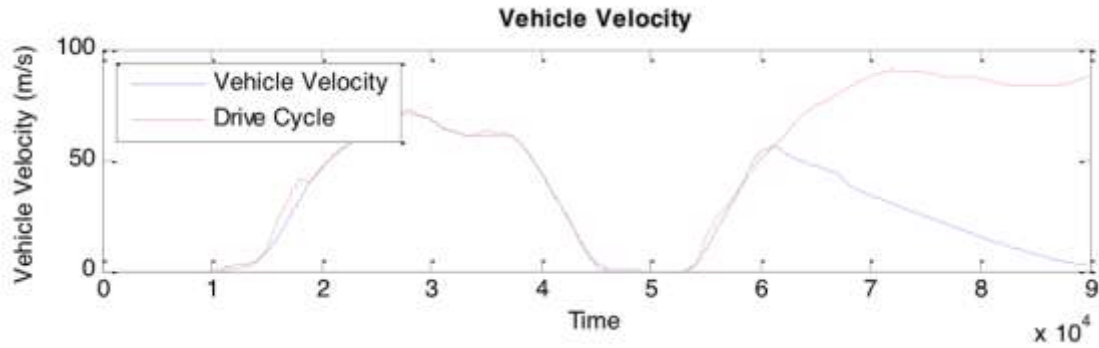
Figure 58: Vehicle Shutdown as a Result of Fault Mitigation

4.2   Control Module

The control module contains all powertrain control and fault mitigation algorithms. The control module receives inputs from the hardware I/O, the fault bus, and previous control outputs. The control module uses signals from the fault bus to take remedial action if a fault occurs. Control module outputs are sent to the write module where they are mapped to hardware I/O to send control commands to powertrain components. The control module is also organized by vehicle powertrain components and vehicle subsystems. The control module structure can be seen in Figure 59.
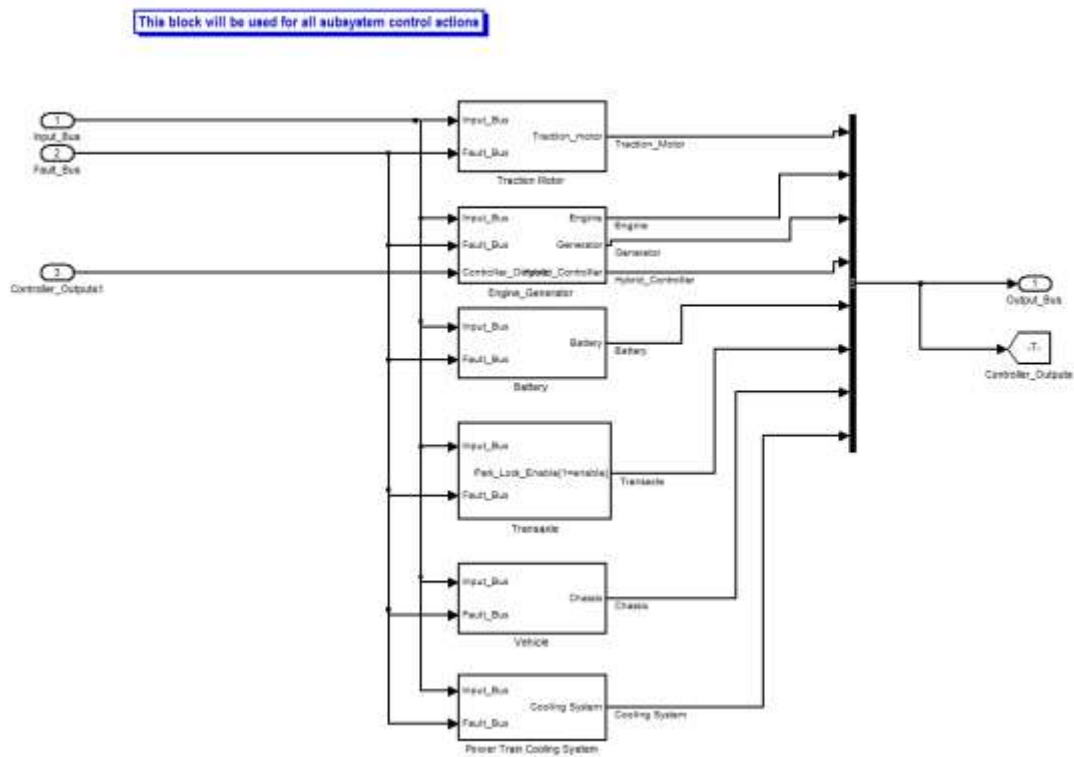
Figure 59: Subsystem Control Module Structure

 Each subsystem is responsible for controlling a specific part of the vehicle. The control subsystems enable and disable vehicle components through relay signals. In order to enable vehicle operation the SCU interprets driver pedal commands and controls several primary signals to each powertrain components. These primary signals are used to control vehicle torques and are shown in Figure 60.
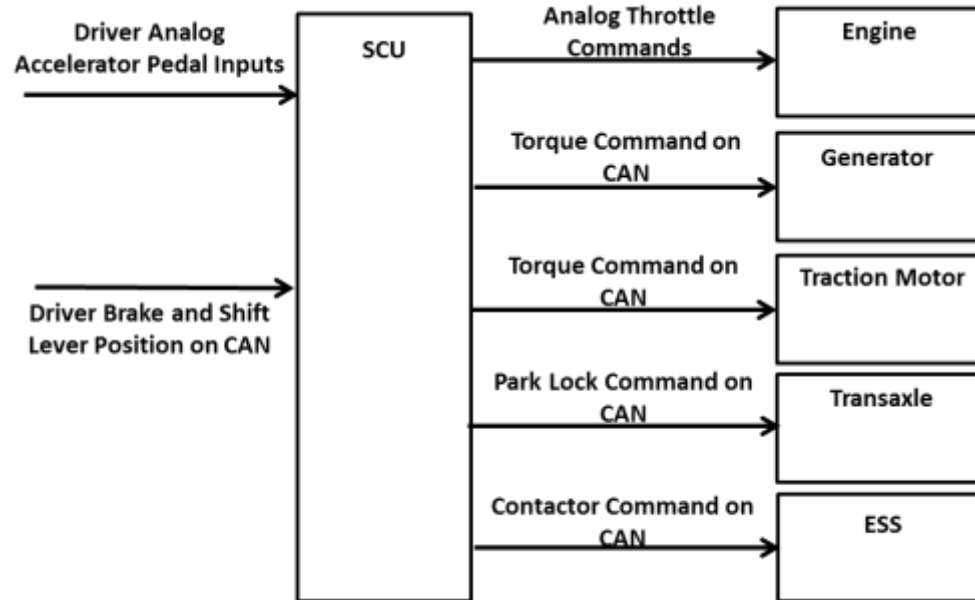
Figure 60: Primary Control Signals

Vehicle operating modes are controlled through two state machines. The first state machine controls the traction motor states, and the second state machine controls the engine/generator states.

4.2.1 Traction Motor Control

The traction motor subsystem is used to determine the toque command sent to the RMS inverter over CAN. The RMS inverter interprets the torque command from the SCU to control switching devices that actuate the motor. Drive modes were controlled through a state machine implemented using Simulink and Stateflow. The traction motor has two states drive and regenerative braking (regen) as shown in Figure 61.
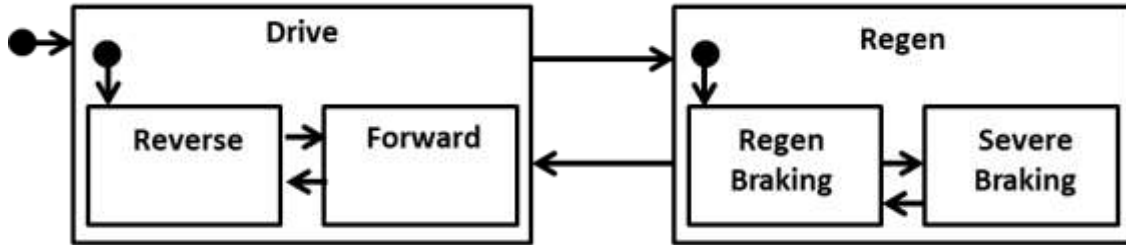
Figure 61: Traction Motor State Machine

The drive state is used for torques applied in the same direction as the rotor's angular velocity, and the regen state is for torques applied in the opposite direction of the rotor's angular velocity. The state machine is entered in the drive state. The drive state has a forward and reverse state. The drive state is entered into the reverse state because the shift lever must pass through reverse before drive using the PRNDL standard. The forward and reverse states map accelerator pedal input to a torque command. The current torque map is a linear function relating maximum accelerator pedal position to peak motor torque regardless of vehicle speed.   If the driver lifts completely from the accelerator pedal a regen torque is applied to slow the vehicle down. Pressing the brake pedal linearly increases the amount of regen applied. When the brake pedal position exceeds 50% the severe braking mode is entered and the regen torque is reduced to avoid interference with ABS.

4.2.2 Engine/Generator Control

The vehicles hybrid modes are controlled through the engine/generator subsystem. The engine/generator subsystem contains a state machine to control transitions between charge depleting and charge sustaining operation. The state machine was implemented using Simulink Stateflow and the state diagram can be seen in Figure 62.
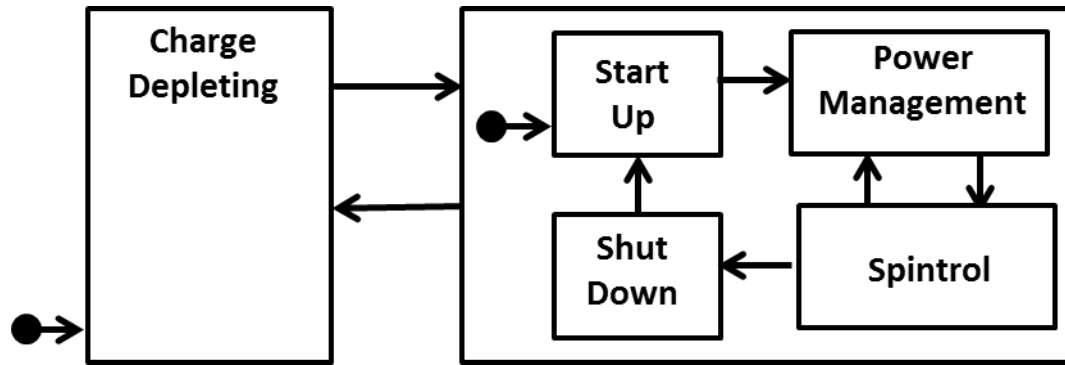
Figure 62: Engine/Generator State Machine

The state machine is entered in the charge depleting state to allow all electric driving when the vehicle is first started. If the vehicle is enabled and the SOC is below 30% the vehicle enters into the charge sustaining state. The charge sustaining state is separated into four states. The four charge sustaining states are engine start-up, Power-tracking, spintrol, and shutdown. The charge sustaining state is entered in engine start up. The engine start up state allows for the engine to be brought to idle speed for one second before entering the power-tracking controller. The engine start-up period can be used to ensure that the engine has started successfully. The engine start-up state can also be used warm the engine up at an operating point that reduces cold start emissions.

If the engine start-up is successful the vehicle enters the power management state. The power management state controls engine operating points to maintain the batteries SOC. The power management strategy is discussed in Chapter 5.

 If the vehicle velocity is below 20 km/hr and the driver is braking the spintrol state is entered. The spintrol state was added to enable engine start/stops. The engine start/stops

were implemented to reduce energy consumption during idle time on urban drive cycles. During spintrol the engine is brought to idle speed and defueled. This is done so that the engine can be shut down smoothly or it can be restarted immediately if the driver requests high power. If vehicle velocity has not reached zero within ten seconds the power-tracking controller is re-entered. Tuning the spintrol parameters on the vehicle will require trade-offs between energy consumption and consumer acceptability. Spintrol costs energy to maintain the engines idle speed but reduces NVH during engine shut downs. Simulations showed that idling the defueled engine costs 1.46 kW, which would result in an energy consumption of .0041 kWh during a full 10 second timeout. The energy required for spintrol is dependent on the engine friction model. The spintrol energy cost could be offset during regen, as 1.96 kW was generated during light braking.

\

5 Power Management Strategy

PHEV energy consumption is highly sensitive to the choice of control algorithms. This sensitivity is greatest during charge sustaining operation while the engine is being utilized to extend the vehicles range beyond its all-electric capabilities. The SCU must control the engine and generator to supply power for the traction motor.

The goal of the power management strategy is to minimize the vehicles energy consumption over a given drive cycle. Energy consumption is the measure of total energy used over the distance traveled as shown in Equation 24.

Equation 24

$$E_c = \frac{Energy}{distance}$$

The total energy consumed over a given drive cycle is the sum of the road load energy required to move the vehicle and the powertrain losses as shown in Equation 25.

Equation 25

$$E_c = \frac{E_{rr} + E_{mass} + E_{aero} + E_{grade} + E_{PTlosses}}{Distance}$$

The road load energy required to move a vehicle over a predetermined drive cycle is fixed for constant vehicle parameters. Therefore the power management controller can reduce energy consumption over a given drive cycle by minimizing powertrain losses.

The powertrain losses are the sum of the engine, generator, motor, and battery losses as shown in Equation 26.

Equation 26

$$Pt_{losses} = losses_{mot} + losses_{eng} + losses_{gen} + losses_{bat}$$

For the series PHEV with a single speed transmission the motor losses are assumed to be fixed for a given drive cycle. Traction motor efficiency could be tuned for certain operating ranges but that is outside of the scope of this project. Since motor losses are fixed the control objective then becomes to reduce the engine, generator, and battery losses over a given drive cycle. The engine is the largest source of powertrain losses. The traction motor has a peak efficiency of 94% (83). In contrast the engine has a peak efficiency of only 40% as can be seen in Figure 64.
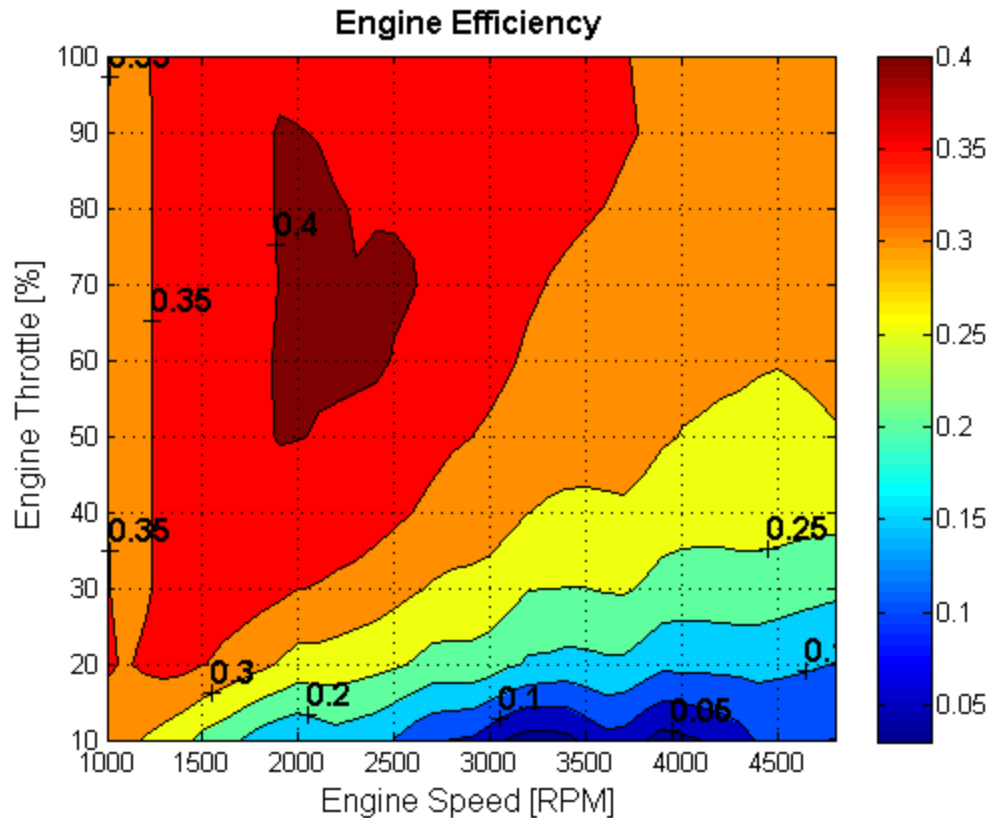
Figure 63: Engine Efficiency Map

Even at its peak efficiency the engine is wasting more energy than is being used to power

the vehicle, therefore controlling the engine operating points is critical to reducing losses

during charge sustaining operation. Engine operating points can be controlled on the

Series PHEV architecture because the engine is decoupled from the road. Decoupling the

engine from the road allows for two degrees of freedom in engine control. Engine torque

and speed can be controlled independently to reduce engine losses.

5.1 Speed Control

The first step in developing the power management controller was to develop a robust

speed controller. The speed controller was designed to regulate the angular velocity of the

coupled engine/generator system to the desired reference value. The speed controller was also designed to be able to compensate for input disturbances in the form of varying engine torques. To achieve these design goals a set of requirements were generated for the speed controller.

5.1.1 Speed Controller Requirements

1. The speed controller shall rise to 1100 RPM in less than .5 s

2. The speed controller shall have less than 15 overshoot during

3. The speed controller shall settle in less than 2 seconds

4. The speed controller shall have less than 5% steady state error

5. The speed controller shall maintain stability in response to 50% changes in engine throttle position

5.1.2 Speed Controller Structure

A Proportional Integral Derivative (PID) algorithm was chosen for the speed controller. PID control is a common form of feedback control that uses a set of gains operating on the error between a measured quantity and a reference value to produce the control signal. The PID gains operate on the error signal, the derivative of the error signal, and the integral of the error signal as shown Equation 27.

Equation 27

$$U(t) = K_p e(t) + K_i \int_o^t e(t) dT + K_d \frac{d}{dt} e(t)$$

The speed controller is being executed on the MABX in real time and requires the

discrete implementation. The discrete PID method chosen uses a forward Euler

integration method as shown in Equation 28 (84) .

Equation 28

$$u(t) = K_p e(t) + K_i \sum e(t)T_s + K_d \frac{e(t) - e(t-1)}{T_s}$$

The difference between the commanded generator speed and the measured generator

speed is used to calculate the error signal. The generator speed is sent to the SCU from

the motor controller over CAN. The generator speed signal was chosen because it has a

higher resolution than the engine speed signal, and it has safer failure modes. The RMS

determines the generator speed using a high resolution resolver mounted on the

generator. Using the generator signal is safer in the event of a communication failure with

the ECU, or an input-shaft failure. The control signal generated by the PID controller is a

torque command to the generator. The torque command is sent to the generator over

CAN. The speed controller diagram can be seen in Figure 64.
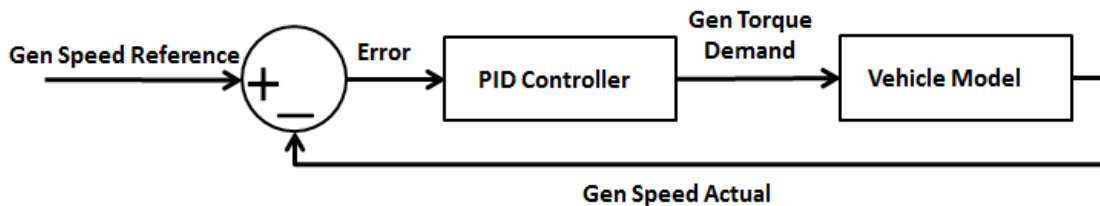
Figure 64: Engine Speed Control Diagram

Due to the complexity of the model dynamics the PID gains could not be solved for analytically. The Kp, Ki, and Kd gains were initially determined iteratively using the Simulink design optimization toolbox. The gains were then hand tuned to achieve the desired response. The Kp was chosen to achieve the desired rise time. In order to reduce overshoot caused by integrator wind up the Simulink integrator clamping circuit was used. The clamping circuit limits the integrator contribution to the control signal during rise time. Once overshoot was reduced the Kd term was tuned to reduce the settling time, and the Ki term was tuned to reduce steady state error.

The torque mass-modulation term causes steady state oscillations in engine torque. Engine torque oscillations cause the engine/generator speed to oscillate. The speed oscillations are fed back to the controller which caused 100 Amp oscillations in DC bus current as the controller attempted to control the oscillations. The oscillations had a magnitude of 5 RPM and a frequency of approximately 60 Hz. To reduce these oscillations in the error signal the generator speed signal was filtered. The engine oscillations occur at a higher frequency than the control dynamics so a low pass filter was implemented. A moving average filter was chosen for its simplicity and the speed with which it could be implemented. A moving average filter is a type of discrete low pass filter that takes a time average of a measured signal for the duration of the measurement buffer (85). The moving average filter can be seen in Equation 29.

Equation 29

$$u(t) = \frac{y(t) + y(t-1) \cdots y(t-n)}{n}$$

A buffer length of 18 samples was chosen because it is the length of one period of engine oscillations. The filter was first tested on post-processed simulation data, and the results can be seen in Figure 65.
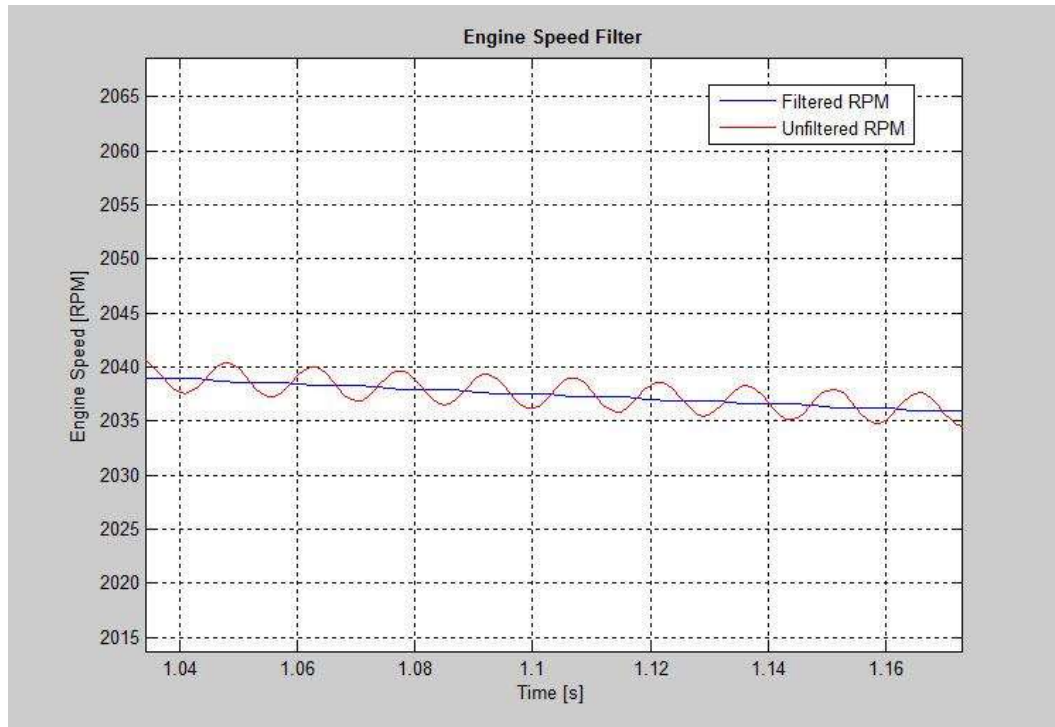
Figure 65: Post Processed Engine RPM Moving Average Filter Results

The moving average filter successfully removed the oscillations from the post-processed RPM signal, but the delay caused significant instability when it was implemented in the model.

The filter was removed and the controller output was rate limited instead. The rate limit saturates the output signal by limiting the first derivative of the input signal using Equation 30.

Equation 30

$$u(t) = (y(t-1) + R_L)C_i + y(t)0^{c_i} \quad \begin{cases} \dfrac{y(t) - y(t-1)}{t_s} > R_L \ C_i = 1 \\ \dfrac{y(t) - y(t-1)}{t_s} > R_L \ C_i = 0 \end{cases}$$

The rate limit successfully removed the oscillations in DC bus current, without compromising controller stability or performance. The effect of the rate limit on the controller output can be seen in Figure 66**.**
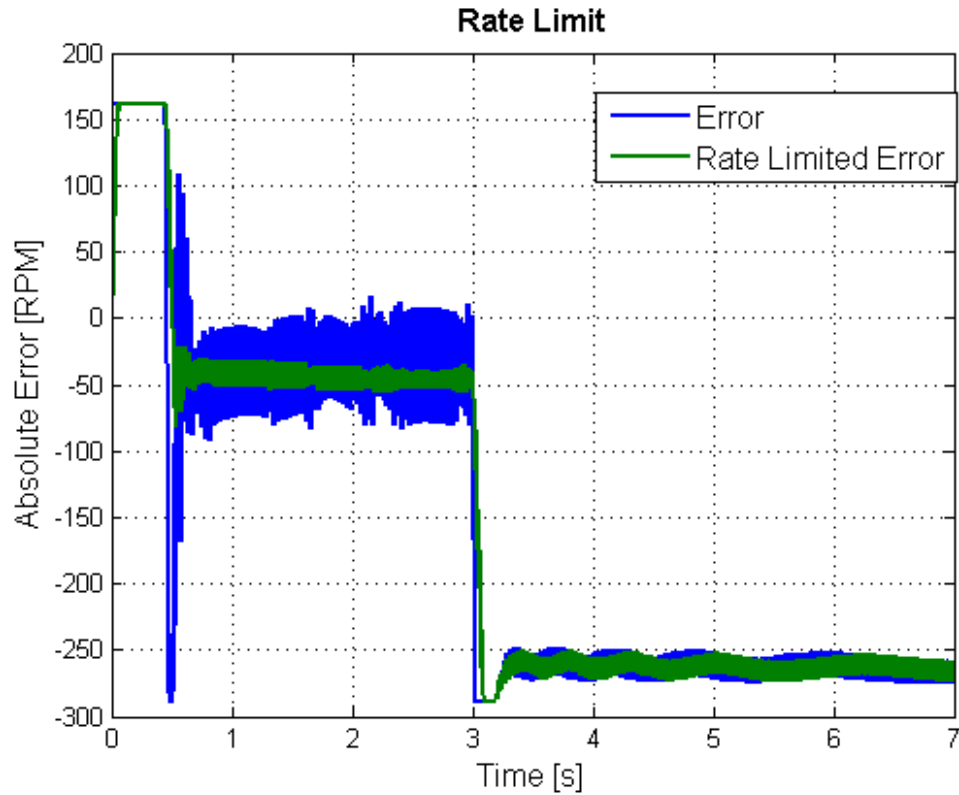
Figure 66: Rate limited Speed Error

5.1.3 Speed Controller Validation

After the rate limits were implemented the speed control algorithm was tested in both SIL and HIL. Communcation delays in the HIL tests did not cause system instabilities or loss of performance. The speed controller response was tested with step changes in speed reference and step changes in engine throttle position. The step response tests used steps from 0-1500 RPM and 0-2000 RPM. The results from the 1500 RPM step response test can be seen in Figure 67.
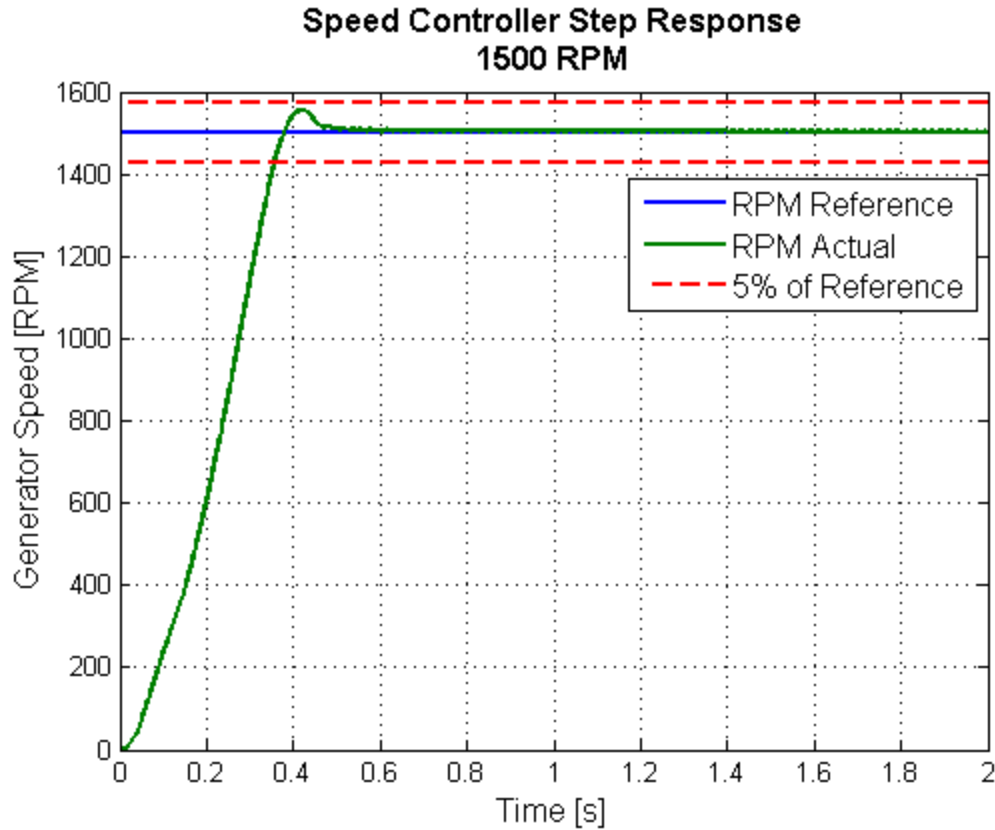
Figure 67: Speed Controller response to 1500 RPM Change in Reference Command

The speed controller has less than 55 RPM of overshoot and settles In less than 0.5 s for 1500 RPM step changes in target speed. The control inputs for the 1500 RPM step response can be seen in Figure 68. The speed controllers torque command is well under the 300 Nm max torque the motor can provide.
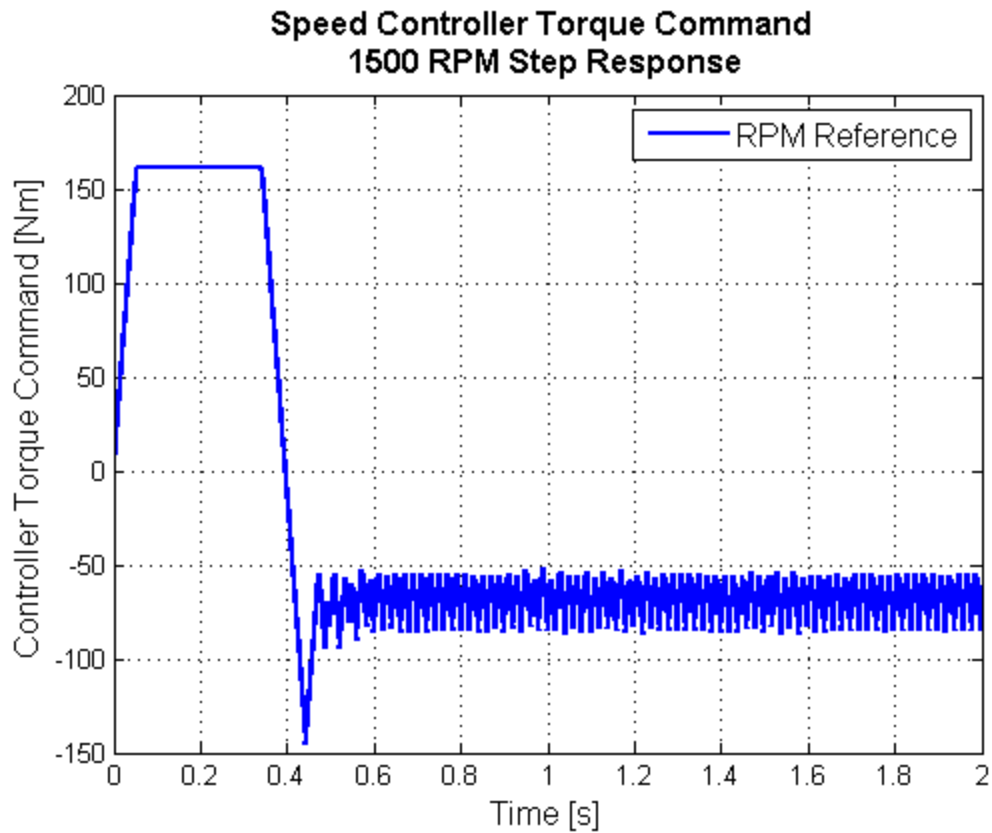
Figure 68: Speed Controller Torque Command Response to 1500 RPM Step Change

The speed controller's response to disturbances was also tested. A step change in engine

throttle position was commanded while the motor speed reference remained constant. The

speed controller's response to a 50% change in throttle at 1500 RPM can be seen in

Figure 69.
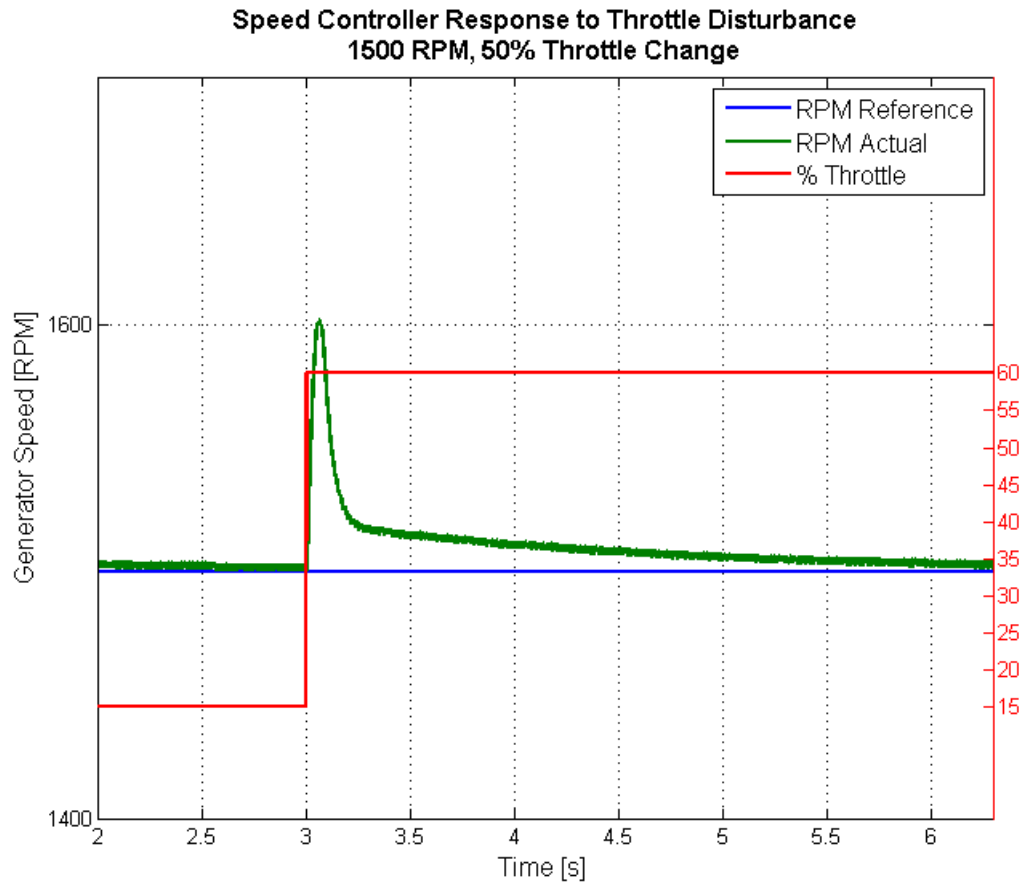
Figure 69: Speed Controller Response to 50% Change in Engine Throttle

The speed controller was able to successfully recover from a 50% change in engine throttle. The engine/generator RPM error increased by over 100 RPM before returning to less than 75 RPM (5%) error in under .5 seconds. It should be noted that the actual change in disturbance torque is limited by the engine dynamics, therefore a step change in throttle is not necessarily a step change in torque. The speed controllers torque requests during the step change in engine throttle can be seen in Figure 70.
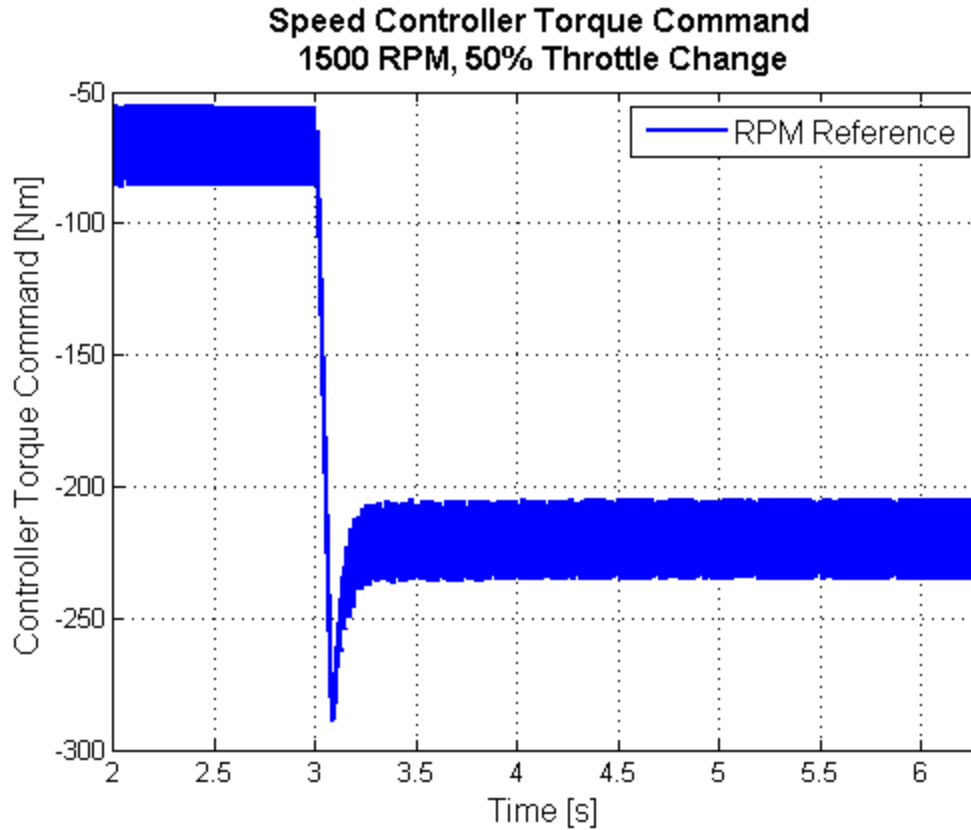
Figure 70: Speed Controller Torque Command for 50% Change in Engine Throttle

Oscillations are still present in the torque command signal even though the rate limit reduced their magnitude. The frequency of these oscillations could exceed the frequency with which the inverter can command torque changes. A more robust low-pass filter could be added to the error input signal to reduce these oscillations.

The speed controller successfully satisfied all requirements. The results of the speed controller testing are summarized in Table 23.

Table 23: Speed Controller Results

	Rise Time [s]	Overshoot [%]	Settling Time [s]	Stability
Required	.5	15	2	50% throttle
Modeled	.38	<5	.5	50% throttle

5.2 Bang-Bang Controller

After stable speed control was achieved a charging sustaining strategy and engine operating points needed to be determined. The first charging strategy developed utilized a simple bang-bang controller. A bang-bang controller is a controller that has two states, always on or always off (86). The bang-bang controller was designed to operate the engine at the minimum BSFC point. The minimum BSFC point is the engine operating point where the least amount of fuel is being consumed to achieve the highest output of mechanical power. The BSFC map shown in Figure 71 was used to evaluate the most efficient engine operating points.
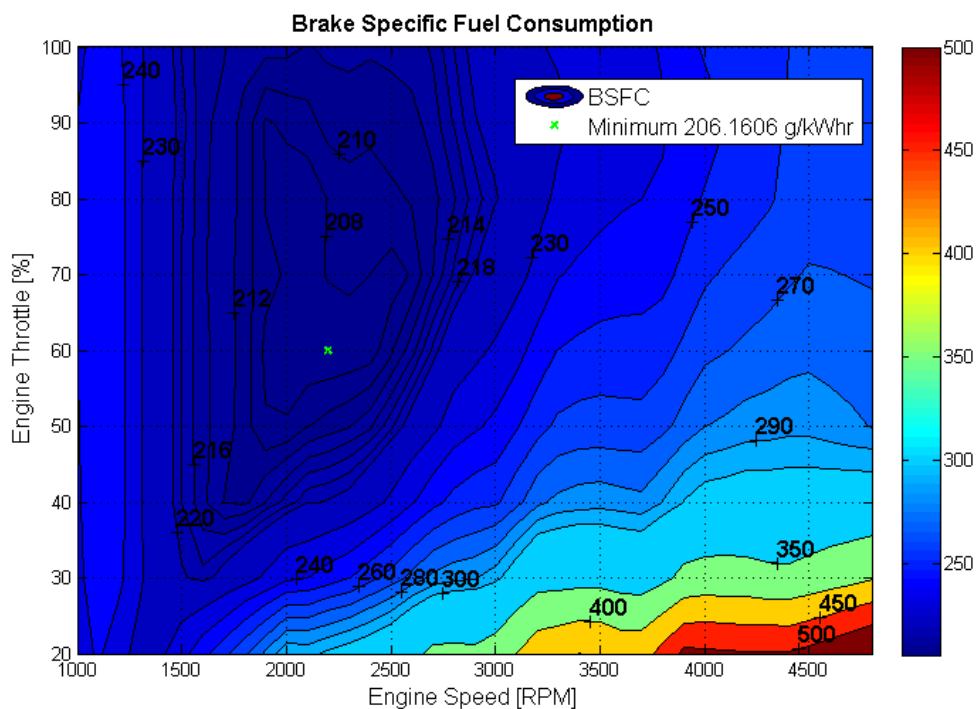
Figure 71: BSFC Map with Minimum BSFC Operating Point

From the map it was determined that the global minimum BSFC operating point was located at 2200 RPM and 60% throttle as can be seen in Table 24.

Table 24: Minimum BSFC Operating Point

Optimal Engine Speed [RPM]	Optimal Throttle Position [%]	Power [kw]
2200	60	59

The bang-bang controller was enabled when the SOC was below 30%. The bang-bang controller used the optimal engine speed as the reference value for the speed controller. The engine throttle position was set to a constant 60%. The engine throttle position was controlled through the two analog accelerator pedal signals for the ECM. This bang-bang

controller was used as the baseline control strategy to evaluate vehicle energy consumption.

5.2.1 Bang-Bang Controller Testing

The bang-bang controller was tested in both SIL and HIL drive cycle simulations. A trace from the US06 drive cycle can be seen in Figure 72.
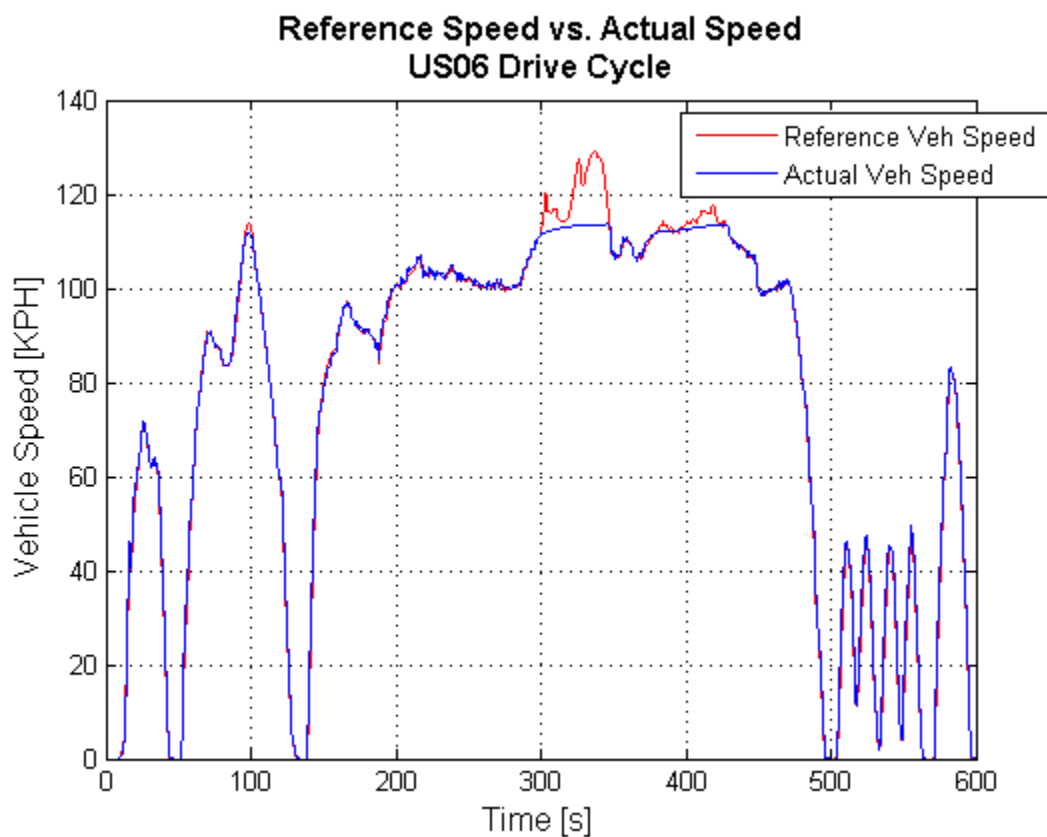
Figure 72: US06 Drive Cycle Velocity Trace

The Series PHEV was unable to follow the US06 velocity trace due to motor model limitations. The drive cycle was started at an initial SOC of 30.5%. The battery SOC increases to 42% over the course of the US06 drive cycle.
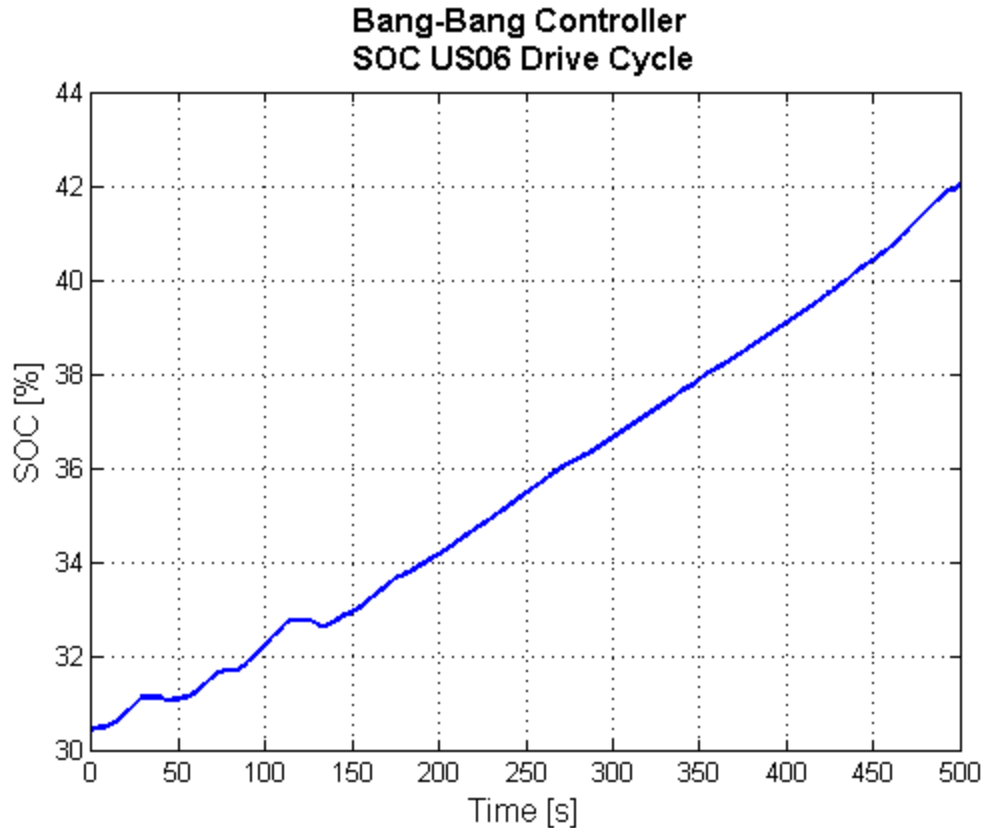
Figure 73: US06 SOC Using Base-line Control Algorithm

The battery SOC increases over the drive cycle because of the power produced by the engine at its minimum BSFC point is greater than the power requires on the drive cycle. The engine generates 59 kW at the minimum BSFC point while the average power demand of US06 the drive cycle is only 23 kW.

The minimum BSFC operating point was successfully maintained throughout the US06 drive cycle. Figure 74 shows the engine operating points are all contained within the minimum BSFC region (The BSFC map shown will be discussed in detail in section 5.3). The points outside of the minimum BSFC region occur during engine/start stops.
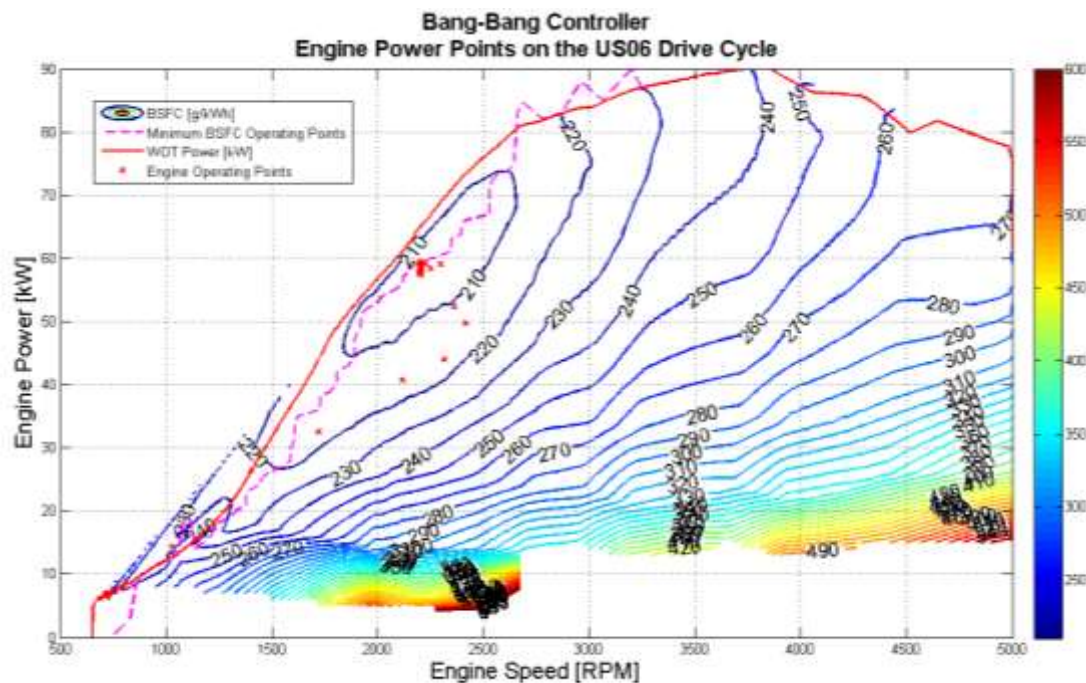
Figure 74: Bang-Bang Controller Operating Points on US06 Drive Cycle

The speed controller successfully maintained the target speed throughout the entire US06

drive cycle. The minimum BSFC speed of 2200 RPM at all non-idling times as can be

seen in Figure 75.
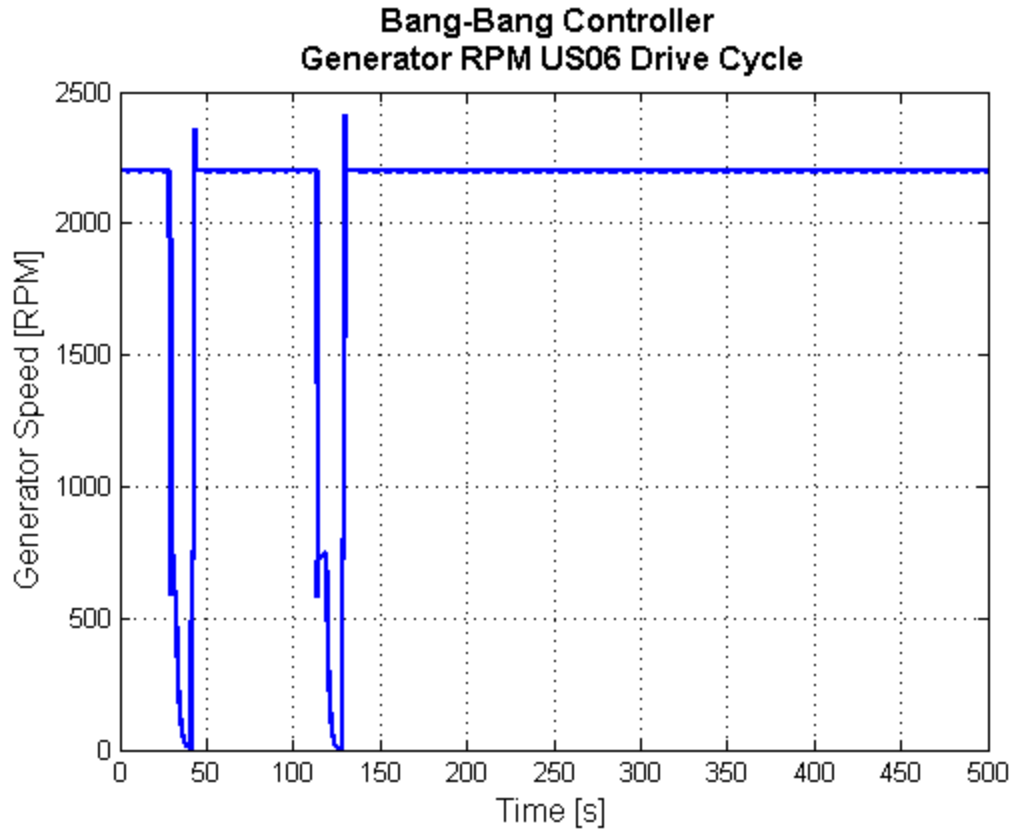
Figure 75: Engine Speed during the US06 Drive Cycle

The engine speed is brought to zero two times during the drive cycle to reduce idle

losses. The engine RPM reduction shows the successful implementation of the engine

start/stops and the spintrol states. The engine torque is also reduced during idle time as

shown in Figure 76
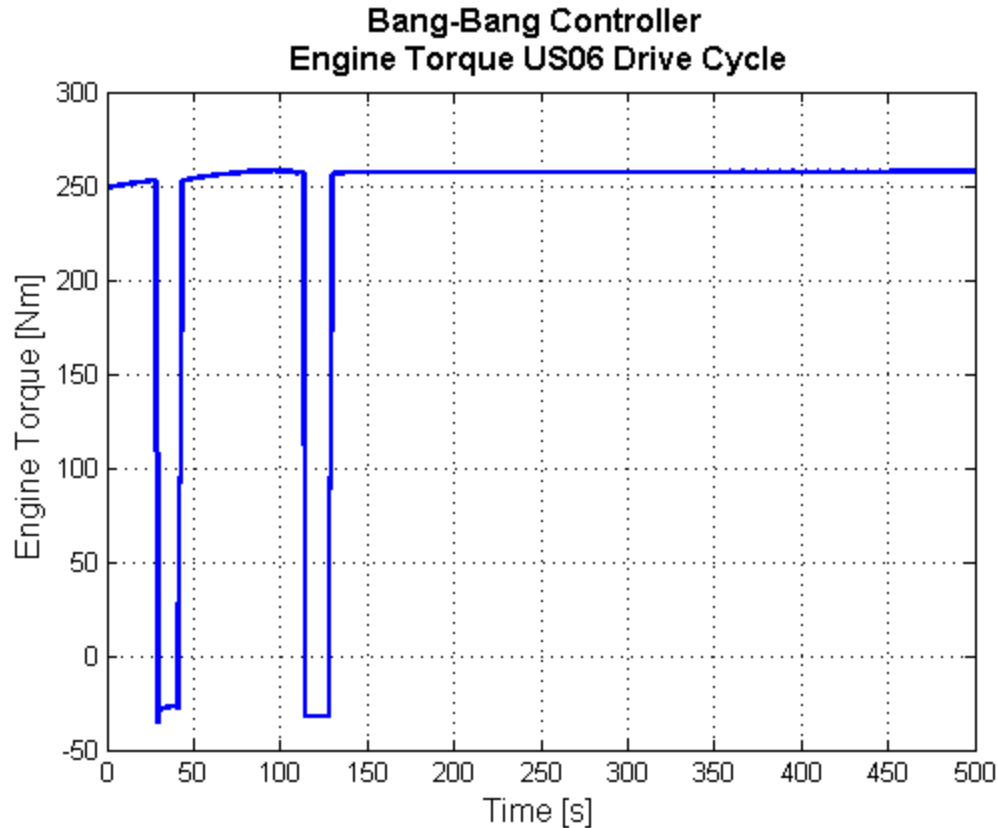
Figure 76: Engine Torque during US06 drive cycle

The engine torque increases slightly over the first 100 seconds of the drive cycle. This is caused by the changes in the engine friction model as the engine warms up. The engine reports negative torque while in spintrol.

5.3 Power-tracking Controller

The bang-bang controller successfully targeted the global minimum BSFC point. However this operating point is not always desirable. During charge sustaining operation the engine is producing a constant 59 kW. The engine produces 35 kW more than the average power required by the US06 drive cycle. The excess power is being used to charge the battery, however the ESS is limited to 18 kW during charging.

Since the Bang-Bang controller produces more power than is required to meet the drive cycle it also suffers from additional conversion losses to store energy in the battery as shown in Equation 31.

Equation 31

$$pt_{losses} = losses_{eng} + losses_{gen} + losses_{bat}$$

A power-tracking controller was developed to operate within the charging limits of the ESS, and to reduce battery losses. The power-tracking control objective is to use the engine and generator to produce a power equal to the current power demand at the road. Furthermore the engine operating points should be chosen so that the power demand is met while minimizing losses. By not producing more power than is needed to drive the vehicle the losses through the battery are also minimized. Total powertrain losses would then only be a function of engine and generator losses as shown in Equation 32.

Equation 32

$$pt_{losses} = losses_{eng} + losses_{gen}$$

5.3.1 Determining Engine Operating Points for Power-Tracking

In order to reduce engine losses during power-tracking the BSFC map was further analyzed. BSFC as a function of engine power and speed was first determined using the BSFC map taken from the simulated dynamometer tests.

Then the minimum BSFC as a function of power and speed was found for the full 0-90 kW power range. The minimum BSFC curve was then projected onto the WOT power

curves with BSFC contours as shown in Figure 77. The pink line is the minimum BSFC

for any given power demand and the red line is the WOT power curve.
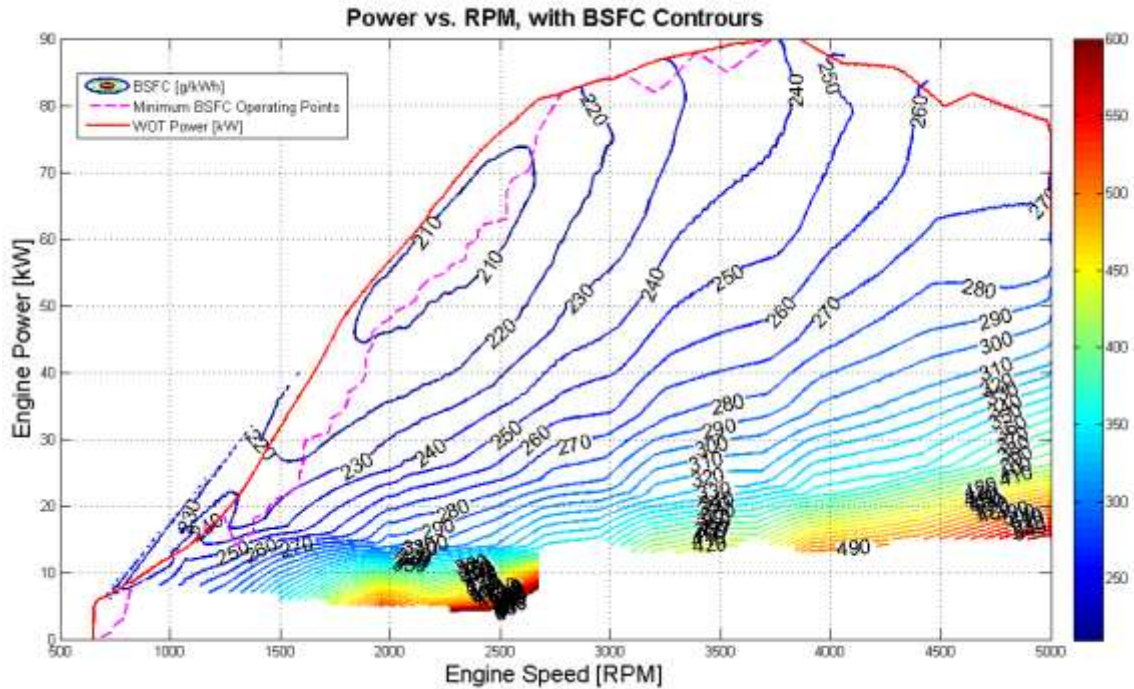
Figure 77: Minimum BSFC

It should be noted that some BSFC data exists outside of the WOT power curve. BSFC

data exists beyond the WOT power curve due to variations in engine temperature during

simulated dynamometer tests. The engine temperature effects the engine friction model

and alters the WOT torque. In order to improve the map new simulation data could be

generated with the engine fully warmed up.

5.3.2 Power Tracking Controller Implementation

The primary input to the power-tracking controller is the current driver power demand. The driver's power demand was calculated using the drivers interpreted torque request at the current angular velocity of the traction motor as shown in Equation 33.

Equation 33

$$P_{dmd} = W_{mot} \cdot T_{driver}$$

To meet the drivers power demand both engine torque and engine speed needed to be controlled. Speed was controlled using the previously mentioned speed controller but a torque controller needed to be developed. Open loop control was first attempted by interpolating the simulated engine dynamometer data to find throttle position as a function of torque and speed. The engine throttle position was not unique for all torques and speeds and the map could not be used to solve for throttle position. After trying open loop control a closed loop method was adopted. In order to control engine torque a second PID controller with a clamping anti-windup circuit was implemented as shown in Figure 78.
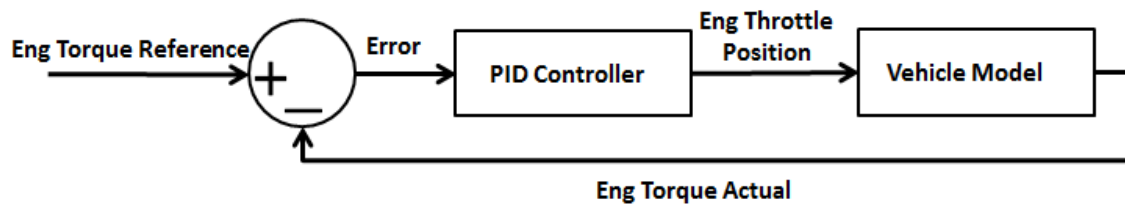
Figure 78: Engine Torque Controller Diagram

The error signal was calculated by finding the difference between the reference torque and the torque produced by the engine. The engine torque is estimated by the ECU and transmitted over CAN to the SCU. Engine throttle position was used as the primary control input. Engine throttle position was controlled through two analog accelerator pedal signals to the ECU.

The minimum BSFC was transposed to output speed as a function of power. The BSFC function was used to determine the reference values for the torque and speed controllers as shown in Figure 79.
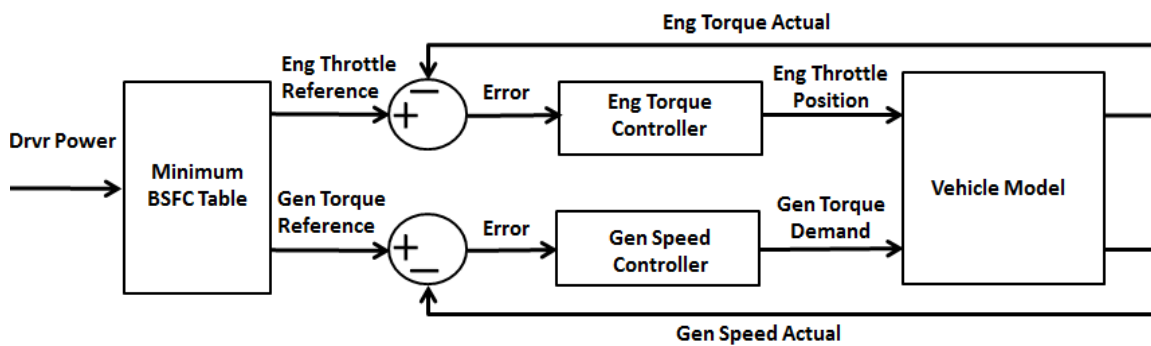
Figure 79: Power-Tracking Controller Diagram

The minimum BSFC function was implemented in a 1D look up table to determine the optimal RPM to meet the current power demand. The RPM output from the minimum BSFC function is used as the reference value for the speed controller. To determine the torque reference the engine torque was back calculated from the engine speed reference and the drivers power demand. The power-tracking controller was implemented on the MABX. The power-tracking controller was added as an embedded function inside the

power management state of the hybrid state machine. The Simulink implementation of

the power-tracking controller can be seen in Figure 80.
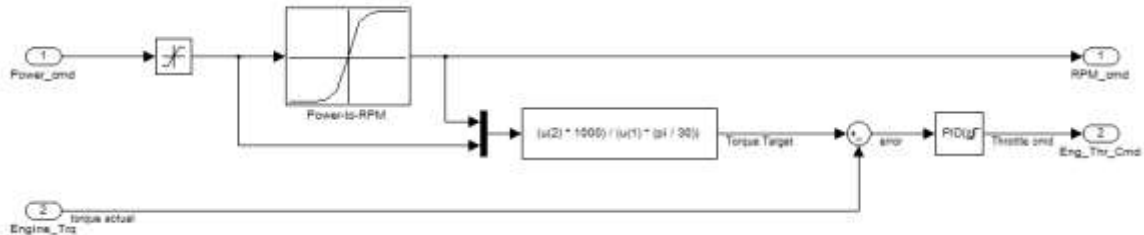
Figure 80: Power Command to Torque and RPM Reference

The power-tracking controller was also designed to work with the Intelligent Driver

Efficiency Assistant (IDEA). IDEA is a predictive controller that supplements the SCU.

IDEA looks at upcoming terrain and driving conditions to suggest modes of operation for

the vehicle. A switch was added to changes the power command for the power-tracking

controller from the instantaneous driver command to the power command suggested by

IDEA. The Simulink implementation of the IDEA power command switch can be seen in

Figure 81.
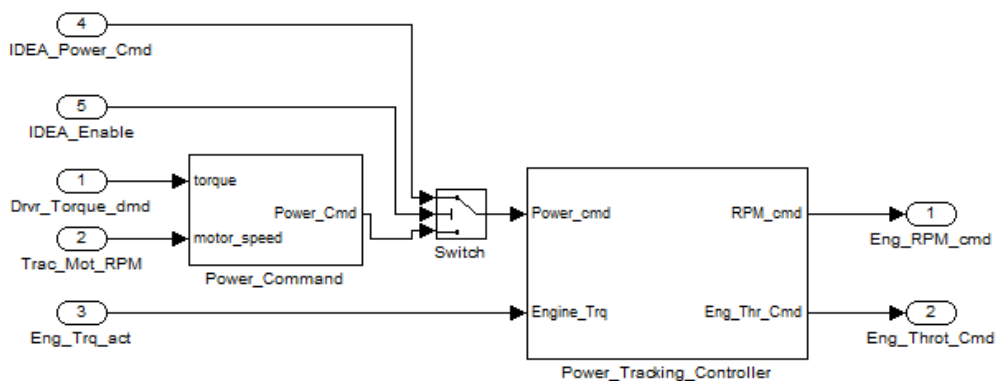
Figure 81: Power Tracking Controller with Idea Compatability

IDEA can look at upcoming driving situations and use predictive logic based on driver history to suggest long term average power demands to the SCU. A reduction in energy consumption from this implementation would likely be minimal; however this strategy does have the potential to drastically reduce emissions while also minimizing energy consumption.

5.3.3 Power-Tracking Controller Testing

The power-tracking controller was tested in both SIL and HIL tests. The power-tracking controller's response to step changes in power demand was first tested before it was tested on drive cycle simulations. The step response tested both positive and negative steps in power demand. The results of the step response tests can be seen in Figure 82.
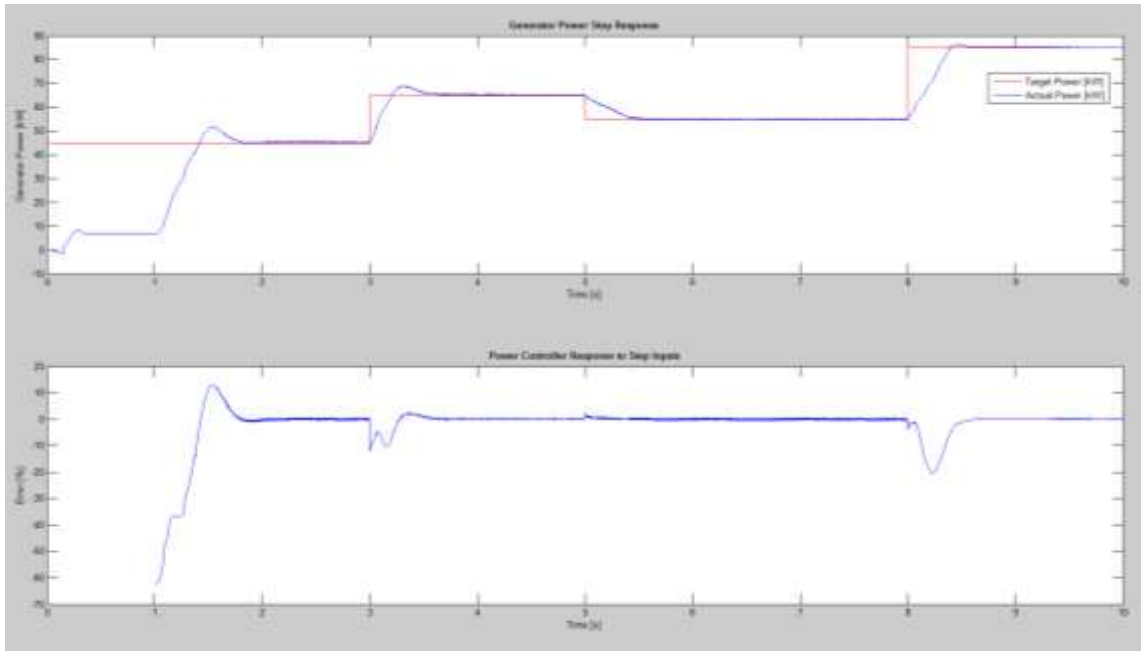
Figure 82: Power Controller Step Response

The power controller achieves the desired power with in .75 s with a maximum overshoot of 12% during large step responses and had minimal steady state error. The error at time less than one second is caused by the warm up state in the hybrid state machine. The engine is operated at idle conditions for one second before transitioning to the power-tracking state. During the power tests the speed controller and throttle controller responses were also examined. The speed controller response can be seen in Figure 83.
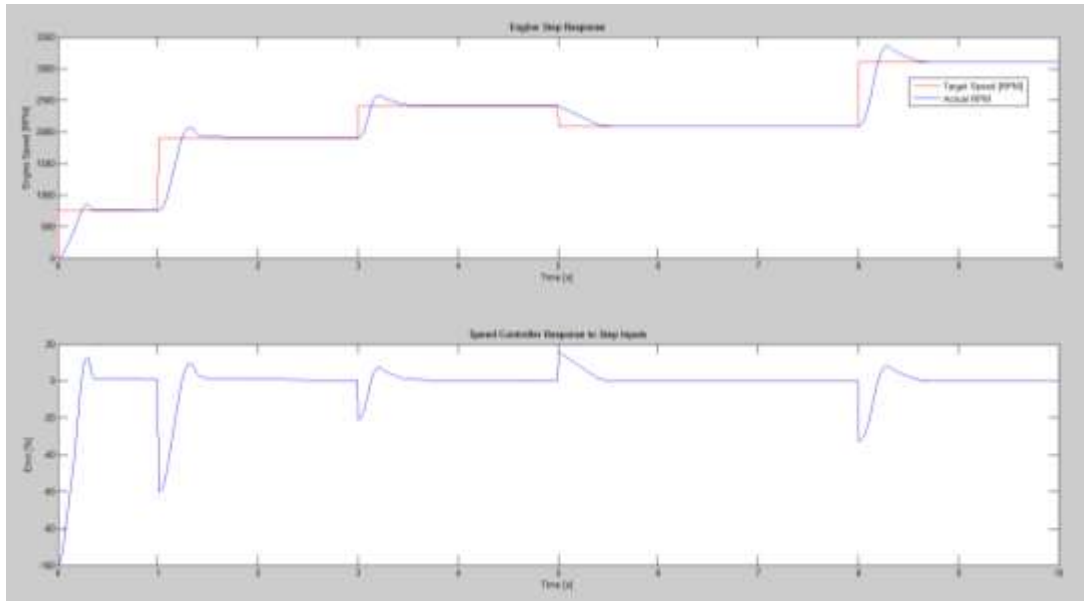
Figure 83: Speed Controller Step Response While Power-Tracking

The throttle controller also successfully tracked changes in torque reference. The settling time of the torque controller is affected by the changing speed. Once the speed controller settles the throttle controller also quickly settles. The results of the engine torque controller response to step inputs from changes in power demand can be seen in Figure 84.
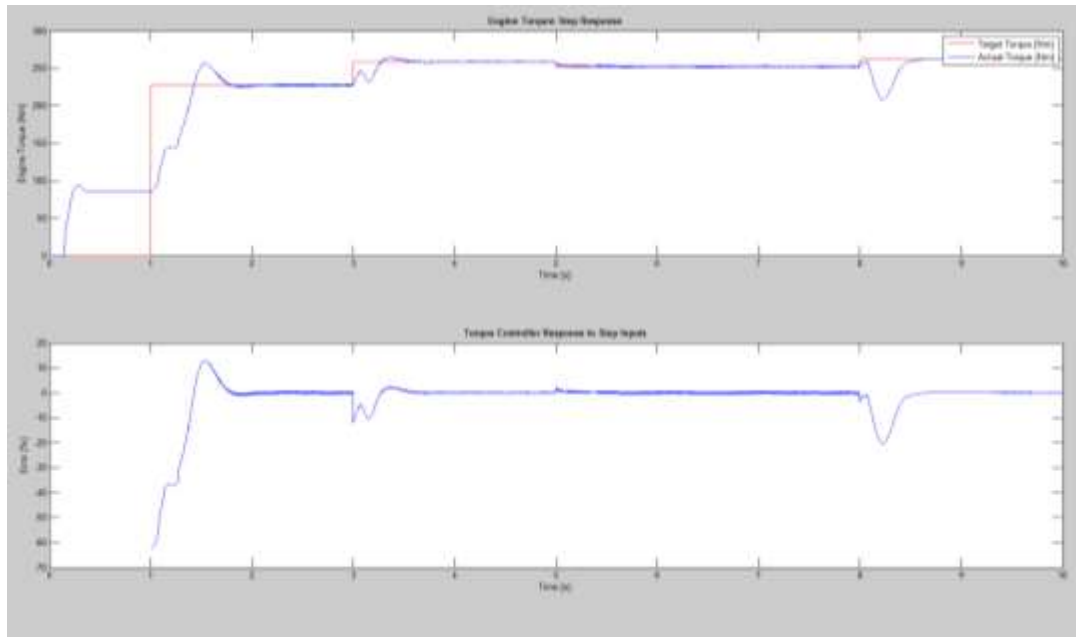
Figure 84: Torque Controller Step Response While Power-Tracking

After the successful validation of the power-tracking controller's response to step inputs, the controller was then tested on SIL and HIL drive cycle simulations. Initial drive cycle tests showed that the power-tracking controller was unable to successfully operate along the minimum BSFC line. The engine operating points were scattered across the map rather than being confined to the minimum BSFC line. The error in operating points during the drive cycle simulations was caused by the constant changes in power demand. The power demand from the driver was changing faster than the power-tracking controller could settle on the reference power. The high frequency power demands caused the controller to be stuck in transient states where engine operating points are not constrained to the minimum BSFC line.

In order to correct the large operating point error during drive cycle simulations the driver's power demand was filtered. Low frequency changes in power demand were desired to allow the power-tracking controller enough time to settle along the minimum BSFC line. To filter out high frequency power demands a moving average filter was applied to the driver's power demand. The moving average filter averaged incoming power demands over 2.1 seconds.

Drive cycle simulations were re-run with the moving average filter in place. The results from the power-tracking controller on the US06 drive cycle can be seen in Figure 85.
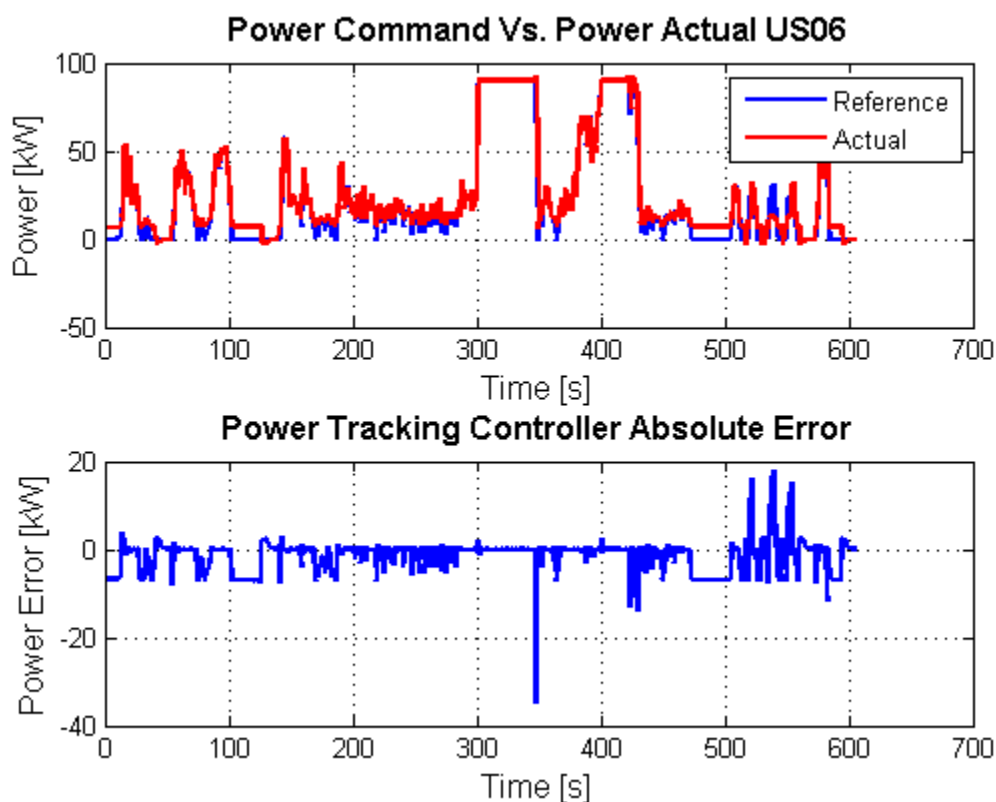
Figure 85: Power Command, Power Actual, Error, Vs. Time on the US06 Drive Cycle

The power tracking controller successfully tracked the driver's power demand during the drive cycle. The power-tracking controller had a mean absolute error of 1.73 kW over the US06 drive cycle. The largest sections of error occur during idle time and very low power demands, when the engine is idling before being shut down. Other large errors are the result of the filtered power demands. The power-tracking error could be reduced by modifying the filter design to track higher frequency signals while still being able to settle on the power reference.

The driver's filtered power demand was tracked successfully while operating along the minimum BSFC line. Figure 86 shows the engine operating points over the US06 drive cycle.
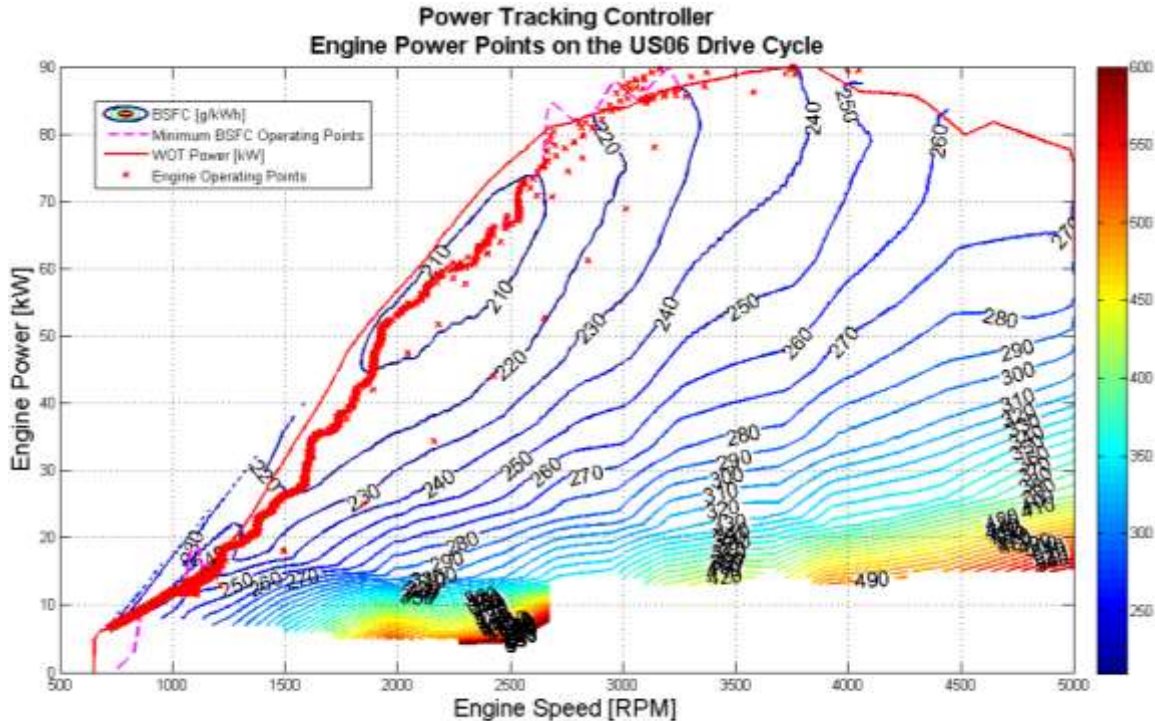
Figure 86: Power-Tracking Engine Operating Points on the US06 Drive Cycle with

Filtered Driver Power Demand

The engine operating points (indicated by a red x) are largely concentrated over the

minimum BSFC line. However some operating points are not along the minimum BSFC

curve and some are even located above the WOT curve. The points that are not along the

minimum BSFC curve occur during engine start/stops and some transient conditions. As

stated previously, the points located above the WOT torque curve are from the changes in

the engine friction model.

The power-tracking controller was able to successfully track the power demand along the

minimum BSFC line however; the SOC was not well maintained over the course of the

drive cycle. The state of charge increases by 4% over the course of the drive cycle as shown in Figure 87 .
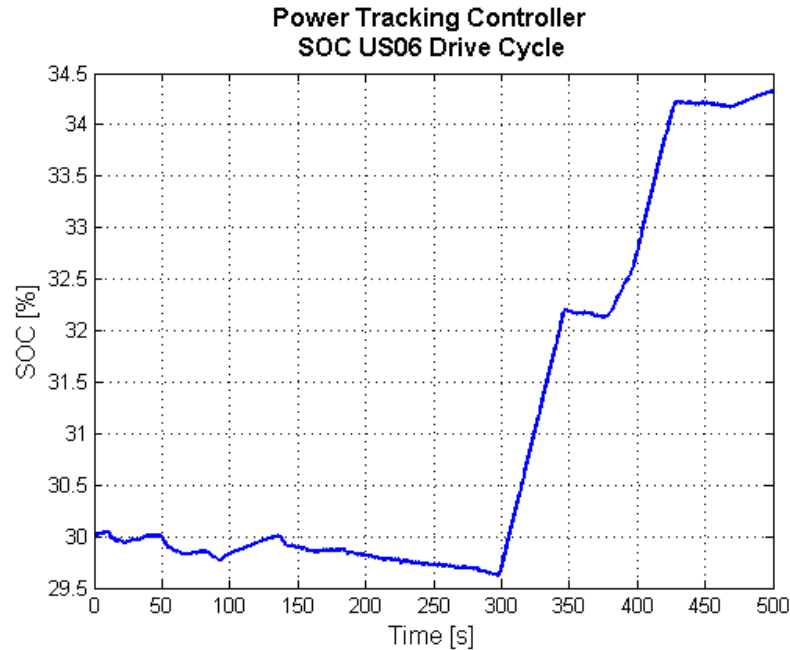
Figure 87: SOC on the US06 Drive Cycle with Power-Tracking Controller

ESS charging occurs during the high-speed sections of the drive cycle when the vehicle model cannot track the velocity trace. The error in the vehicle velocity causes the drivers PI controller to request maximum torque. The power-tracking controller uses this driver demand to generate the power reference. The power-tracking controller successfully tracks the driver's power demand but the power demand during errors in vehicle velocity is much higher than the power being used. Adding a dynamic saturation on the torque requests that are based off of the motor capabilities would remedy the charging problem. If this section is ignored, the SOC actually depletes slightly over the drive cycle. This is because the power reference does not compensate for generator and motor losses.

6   Conclusions

A SCU for a series PHEV was successfully created with an intuitive structure that enabled fault diagnostics for safety critical systems. In order to reduce the vehicles energy consumption a power-tracking control strategy was implemented. A power tracking control strategy was implemented to operate the engine along the minimum BSFC line during charge sustaining operation. This controller achieved an almost 50% reduction in fuel losses during the EPA drive cycle when compared to the initial bang-bang controller. The reason the power-tracking controller was more effective than the bang-bang controller at reducing energy consumption can be seen by analyzing the engine losses map Figure 88.
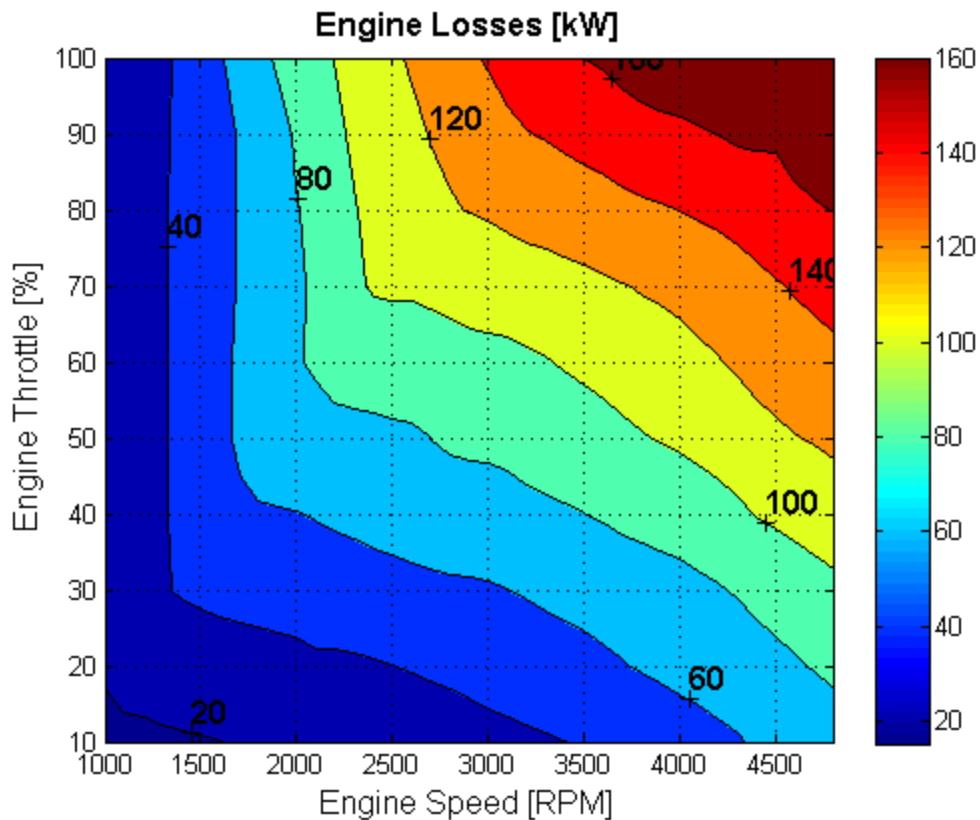
Figure 88: Engine Losses Map

Even though the bang-bang controller operates the engine at the global minimum BSFC point it has higher losses than the power-tracking controller. Global efficiency is not as relevant when the power can be chosen. At the minimum BSFC operating point the engine has over 80 kW of losses. Therefore operating at a less efficient point could have fewer engine losses and result in a higher vehicle level efficiency.

7 Future Work

The work presented in this thesis is from year 1 of the EcoCar2 competition. In order to have a successful vehicle at competition future work must be done to the vehicle architecture, the plant models, and the SCU.

7.1 Vehicle Architecture

Future improvements to the vehicle architecture are limited by competition rules. However the vehicle performance would benefit from the addition of a two speed gear box for the traction motor. This could be used to allow the vehicle to reach higher top speeds and increase vehicle performance the motors corner speed. A geared coupling between the engine and generator would allow the generator to control the engine continuously. Engine peak torque can be sustained indefinitely; however the electric motor becomes thermally limited under peak power demands.

7.2 Plant Model

The Remy motor models, the catalyst model and the ESS model need to be expanded over the following year. The plant model CAN bus structure also needs to be updated to completely mimic the CAN structure in the donated vehicle.

The Remy motor model needs to include the non-linear inductance tables achieve more accurate performance at high speed. The catalyst model needs be modified to include temperature effects using the Arrhenius equation. The CAN communication network needs to be increased to fully represent that of the cars.

7.3 SCU

The SCU will require continual development to achieve substantial reductions in energy consumption and emissions. A regenerative braking strategy needs to be implemented. The regen strategy should be able to accomplish all braking on the EPA drive cycles with just regen. The current regen strategy is just a linear adjustment based on the driver brake signal. A regen profile should be created to achieve target decelerations at different vehicle velocities.

The generator and engine losses maps should be combined to find the lowest system losses to meet the driver's power demand. The stability of the power-tracking controller needs to be quantified.

The power-tracking controller should address the trade-offs between energy consumption and emissions. Operating points that are chosen to reduce energy consumption are typically worse for emissions. The tradeoff between energy consumption and emissions can be seen by examining the engines BSFC map and the NOx map shown in Figure 89.
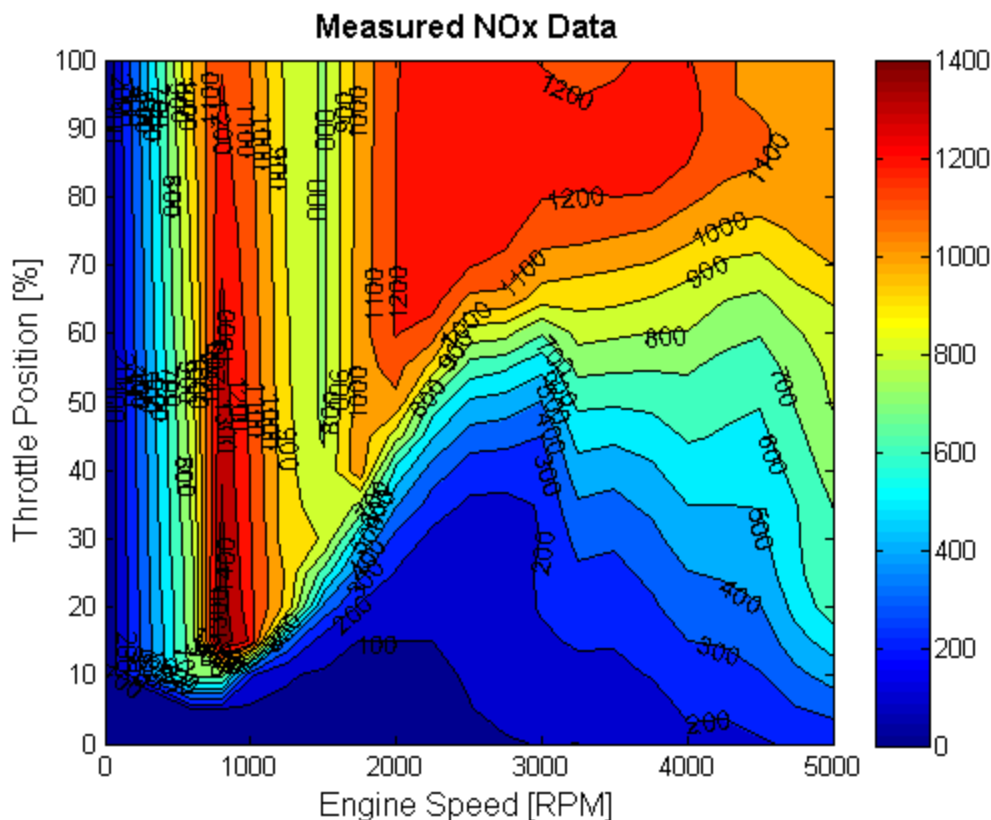
Figure 89: NOx Contour Map

The minimum BSFC operating point is at 2200 RPM and 60% throttle, this operating

point is located in one of the highest emissions regions. A Selective Catalytic Converter

(SCR) system is being developed to reduce the engines emissions in the exhaust stream.

The main limiting factor to the emissions reduction achieved by the SCR system during

drive cycle simulations is the surface coverage fraction. If the catalyst becomes over

saturated there are no longer free sites available for the reaction to take place. The

catalyst can easily become over saturated during a drive cycle due to the very slow

catalyst dynamics. In order to reduce both energy consumption and emissions the time

constants for the power-tracking controller could be matched with the time constants for

the catalyst. This would allow the catalyst enough time to reduce the downstream

emissions before the engine/generator operating points are changed. IDEA could also be used to generate long term power averages for the trip. The long term average power could be used for the power tracking controller during these steady state operations the engine emissions could be reduced drastically.

Works Cited

1. **Infoplease.** Licensed Drivers and Vehicle Registrations. *Infoplease.* [Online]

infoplease, 2004. http://www.infoplease.com/ipa/A0908125.html.

2. **Sousanis, John.** World Vehicle Population Tops 1 Billion Units. *Wards Auto.* [Online]

August 15, 2011. wardsauto.com/ar/world_vehicle_population_110815.

3. **Unger, Nadine.** Transportation Pollution and Globarl Warming. *NASA Goddard*

Institute for Space Studies. [Online] June 2009.

www.giss.nasa.gov/research/briefs/unger_02.

4. **American Petroleum Institute .** *The Economic IMpacts of the Oil and Natural Gas*

Industry on the U.S. Economy: Emplyment, Labor, Income and Value Added. s.l. : Price

Water House Coopers, 2009.

5. **Parra, Fransisco.** *Oil Politics, a modern history of petroleum.* NY, NY : I.B. Tauris &

CO. Ltd, 2004.

6. **Energy Information Administration.** *International Energy Outlook, 2008.* s.l. : US

Department of Energy, 2008.

7. **Environmental Protectiona Agency.** EPA.gov. *Climate Change .* [Online] EPA,

2012. http://epa.gov/climatechange/ghgemissions/usinventoryreport.html.

8. **The New York Times.** The New York Times. *Science; Environment Space &*

Cosmos. [Online] September 20, 2012.

9. **National Resources Defense Council.** Global Warmin Puts the ARctic on Thin Ice.

Natural Resources Defense Council the Earths Best Defense. [Online] National

Resources Defense Council, November 2005.

10. **National Research Council.** *Advancing the Science of Climate Change.* Washington DC : NRC, 2010.

11. **U.S. Energy Information Administration.** *Anual Energy Outlook 2012.* s.l. : U.S. EIA, 2012.

12. **U.S. Department of Energy.** *Transportation Energy Data Book.* s.l. : U.S. DOE, 2012.

13. **Flintoff, Corey.** Where Does America Get Oil? You May Be Surprised. *NPR.* [Online] April 2012. www.npr.org/2012/04/11/150444802/where-does-america-get-oil-you-may-be-surprised.

14. **OPEC.** Member Countries. *Organization of the Petroleum Exporting Countries.* [Online] OPEC, September 2012. http://www.opec.org/opec_web/en/about_us/25.htm.

15. **Organization of Petroleum Exporting Countries.** *World Oil Outlook.* s.l. : Organizatino of Petroleum Exporting Countries, 2012.

16. **Krisher, Tom.** Fuel Efficiency Standards: Obama Administration Finalizes New Regulations For Cars And Trucks. *Huffinton Post.* [Online] Washington Associated Press, 08 28, 2012.

17. **Wakefield, Ernest H.** *History of the Electric Automobile, Battery-Only Powered Cars.* Warrendale : SAE, 1994.

18. **Voelcker, John.** CA Passes Landmark Laq Requiring Many More Zero-Emission Vehicles. *The Car Connection.* [Online] High Gear Media, January 30, 2012.

19. *The CO2 Benefits of Electrification E-REVs, PHEVs and Charging Scenarios.* **Tate, E.D. and Savagian, Peter J. .** s.l. : SAE, 2009. 2009-01-1311.

20. **Galbraith, Jad Mouawad and Kate.** Study Says Big Impact of the plug-in hybrid will be decades away. *The New York Times.* 2009.

21. *Surface Vehicle Information Report.* **SAE International.** s.l. : SAE International, 2008. J-1715.

22. *The Electrification of the AUtomobile: From Conventional Hybrid, to Plug-in Hybrids, to Extended-RAnge Electric Vehicles.* **Tate, E.D., Harpster, Michael O. and Savagian, Peter J.** s.l. : SAE International, 2008. 2008-01-0458.

23. **Hess, Alexander and Sauter, Michael.** The 20 Best-Selling Hybrid Cars. *Fox Business.* [Online] September 28, 2012.

24. **Hirsch, Jerry.** Toyota Prius is best selling car in California; domestics lag. *Los Angeles Times.* 2012.

25. **Lyons, Dan.** Prius Expands the Brand:2012 Toyota Prisu C. *Times Union.* [Online] Times Union, April 06, 2012. http://www.timesunion.com/news/article/Prius-Expands-the-Brand-2012-Toyota-Prius-c-3386045.php.

26. **Green Car Congress.** Toyotal Sells One-Millionth Prius in the US. *Green Car Congress.* [Online] April 2011. http://www.greencarcongress.com/2011/04/prii-20110406.html#more.

27. **Nevers, Chris.** Fuel Economy Labeling of Advanced Technologies. *EPA.* s.l. : SAE, 2009.

28. **Stenquist, Paul.** How Green Are Electric Cars? Depends on Where you Plug In. *The New York Times.* [Online] April 13, 2012.

29. *Sutdy on the Potential Venefits of Plug-in Hybrid Systems.* **Komatsu, Masayuki, et al., et al.** s.l. : SAE International, 2008. 2008-01-0456.

30. **US Department of Energy.** Find a Car. *Fuel Economy.gov.* [Online] U.S. DOE.

www.fueleconomy.gov.

31. **EPA Office of Transportation and Air Quality.** Electric Vehicles.

fueleconomy.gov. [Online] U.S. DOE, 2012.

www.fueleconomy.gov/feg/evtech.shtml#end-notes.

32. **Brinkman, Norman, et al., et al.** *Well-to-Wheels Analysis of Advanced Fuel/Vehicle*

Systems - A North American Study of Energy Use, Greenhouse Gas emisssions, and

Criteria Pollutant Emissions. s.l. : U.S. DOE, 2005.

33. **Just-auto.** Electric Vehicles market research, news, statistics, data and forecasts.

Just-auto. [Online] www.just-auto.com/electricvehicles.

34. **Miller, John M.** *Propulsion Systems for Hybrid Vehicles.*

35. **Ehsani, Mehrdad, Gao, Yimin and Emadi, Ali.** *Modern Electric, Hybrid Electric,*

and Fuel Cell vehicles. Fundamentals, Theory, and Design Second Edition. Boca Raton :

Taylor and Francis Group, 2010.

36. **Ramadhas, Arumugam S.** *Alternative Fuels For Transportation.* Boca Raton : CRC

Press, 2011.

37. **Elgowainy, A., et al., et al.** *Well-to-Wheels Energy Use and Greenhouse Gas*

Emissions Analysis of Plug-in Hybrid Electric Vehicles. s.l. : ANL U.S. DOE, 2009.

38. **Jegarajah, Sri.** Surging US Corn PRices SPark Food Versus Fuel Debate. *CNBC*

Energy. [Online] August 3, 2012.

www.cnbc.com/id/48477352/Surging_US_Corn_Prices_Spark_Food_Versus_Fuel_Deba

te%C2%A0.

39. **Gardner, Timothy and Abbot, Charles.** Analysis: In food vs fuel debate, U.S.

resolute on ethanol. *Reuters.* [Online] February 14, 2011.

www.reuters.com/article/2011/02/us-usa-ethanol-suppport-idUSTRE7D0UR20110214.

40. **US DOE.** Ethanol Fueling Station Locations. *Alternative Fuels Data Center.* [Online]

U.S. DOE, November 5, 2012. www.afdc.energy.gov/fuels/ethanol_locations.html.

41. **E85 Prices.** E85 Prices. *E85Prices.* [Online] E85 Prices, December 2012.

42. **US DOE.** Biodiesel Fuel Basics. *Alternative Fuels Data Center.* [Online] US DOE,

November 5, 2012. http://www.afdc.energy.gov/fuels/biodiesel_basics.html.

43. **Alternative Fuels Data Center.** Biodiesel Blends. *Alternative Fuels Data Center.*

[Online] U.S. DOE, November 5, 2012.

http://www.afdc.energy.gov/fuels/biodiesel_blends.html.

44. —. Alternative Fuels Data Center. *Alternative Fuels Data Center.* [Online] U.S.

DOE, November 5, 2012. http://www.afdc.energy.gov/fuels/biodiesel_benefits.html.

45. **Clean Cities.** *Clean Cities Alternative Fuel PRice Report.* s.l. : January, 2011.

46. **Alternative Fuels Data Center.** Biodiesel Fueling Station Locations. *Alternative

Fuels Data Center.* [Online] U.S. DOE, November 5, 2012.

http://www.afdc.energy.gov/fuels/biodiesel_locations.html.

47. **Alternative Fules Data Center.** Hydrogen Basics. *Alternative Fuels Data Center.*

[Online] U.S. DOE, November 5, 2012.

http://www.afdc.energy.gov/fuels/hydrogen_basics.html.

48. **Fuel Economy.gov.** How Fuel Cells Work. *Fueleconomy.gov.* [Online] U.S. DOE,

November 30, 2012. http://www.fueleconomy.gov/feg/fcv_pem.shtml.

49. **Department of Energy.** Hydrogen, Fuel Cells and Infrastrucutre Technologies

Program. *U.S. Department of Energy Energy Efficiency and Renewable Energy.* [Online]

DOE. http://www.fueleconomy.gov/feg/animation/swfs/fuelcellframe.html.

50. **DOE.** Types of Fuel Cells. *Fuel Cells.* [Online] U.S. DOE, March 8, 2011.

http://www1.eere.energy.gov/hydrogenandfuelcells/fuelcells/fc_types.html.

51. **Alternative Fuels Data Center.** Electricity PRoduction and Distribution. *Alternative*

Fuels Data Center. [Online] DOE, July 30, 2012.

http://www.afdc.energy.gov/fuels/electricity_production.html.

52. —. Emissions From Hybrid and Plug-in Electric Vehicles. *Alternative Fuels Data*

Center. [Online] DOE, July 30, 2012.

http://www.afdc.energy.gov/vehicles/electric_emissions.php.

53. *Hybrid Vehicle Battery Technology - The Transition from NiMH to Li-ion.* **Snyder,**

Kent, Guant, Xiao and Ted J. s.l. : SAE, 2008. 2008-01-1-005.

54. **Bunkley, Nick.** Batteries in Electric Cars Examined After Chevy Volt Fire. *The New*

York Times. [Online] November 11, 2011.

http://www.nytimes.com/2011/11/12/business/energy-environment/regulators-examine-

electric-car-batteries-after-fire.html.

55. *Theraml Response and flammability of Li-ion Cells for HEV and PHEV Applications.*

Roth, Peter. s.l. : SAE, 2008. 2008-01-0400.

56. *Evaluation of Cold Temperature Performance of JCS-VL41M PHEV Battery Using*

Battery HIL. **Shidore, Neeraj and Bohn, Theodore.** s.l. : SAE, 2008. 2008-01-1333.

57. **Tahil, William.** *The Trouble with LIthium Implications of Future PHEV Production*

for Lithium Demand. s.l. : Meridian International Research, 2007.

58. **Garthwaite, Josie.** How Ultracapcitors Work (and Why They Fall Short). *GigaOm.* [Online] July 2011. http://gigaom.com/cleantech/how-ultracapacitors-work-and-why-they-fall-short/.

59. **Coughlin, Chrissy.** Ultracapcitors: The next big thing in energy storage? *Green Biz.* [Online] June 10, 2012. http://www.greenbiz.com/blog/2012/06/10/ultracapacitors-next-big-thing-energy-storage.

60. **Schindall, Joel.** The Charge of the Ultra - Capacitors Nanotechnology takes energy storage beyond batteries. *IEEE Spectrum Inside Technology.* [Online] November 2007. http://spectrum.ieee.org/green-tech/advanced-cars/the-charge-of-the-ultra-capacitors.

61. *Spinning into control: High-tech reincarnations of an ancient way of storing energy.* **Davide, Castelvecchi.** 2007.

62. **Flybrid Systems.** Flybrid Systems Technology. *Flybrid Systems.* [Online] 2012. http://www.flybridsystems.com/F1System.html.

63. **SAE International.** *Chevrolet Volt Development Story of the Pioneering Electrified Vehicle.* Warrendale : SAE international, 2011.

64. *Electric, Hybrid, and Fuel-Cell Vehicles: Architectures and Modeling.* **Chan, C.C, Bouscayrol, A and Chen, K.** s.l. : IEE VehicularTechnology, 2010.

65. *Efficiency and suitability analyses of varied drive train architectures for plug-in hybrid electric vehicles (PHEV) applications.* **Xin, Li and Williamson, S.S.** s.l. : IEEE Power and Propulsion Conference, 2008. vol pp.106, 3-5.

66. *Effects of different PHEV control strategies on vehicle performance.* **Tulpule, P, Marano, V and Rizzoni, G.** s.l. : American Control Conference, 2009.

67. **Wang, M.Q.** *Transportaion Fuel Cycle Model, Volume 1: Methodology,*

development,USe and Results, Volume1. s.l. : Argonne National Laboratory, 1999.

68. **EPA.** Emissions Standard Driving Cycles. *EPA.gov.* [Online] EPA, 2012.

www.epa.gov/otaq/standards/light-duty.

69. **Miliken, William and Milliken, Douglas.** *Race Car Vehicle Dynamics.* Pa. :

Society of Automotive Engineers, 1995.

70. **Guzella, Lino and Sciarretta, Antonio.** *Vehicle Propulsion Systems: Introduction to*

Modeling and Optmization. Switzerland : s.n., 2007.

71. **SAE.** *Recommended practice for measuring the exhaust emissiions and fuel economy*

of hybrid electric vehicles, including plug-in Hybrid vehicles. s.l. : SAE, 2010. J1711.

72. *Utility Factor Definitions for Plug-in Hybrid Electric Vehicles Using Travel Survey*

Data. **SAE.** s.l. : SAE, 2010, Vol. J2841.

73. *Hybrid electric vehicle propulsion system architectures of the e-CVT type.* **Miller,**

J.M. s.l. : IEEE Power Electronics, 2006. Vol.21 no.3 pp756-767.

74. **Hyatt, Townsend.** Powertrain Renders. Daytona Beach : ERAU EcoCAR, 2012.

75. **Remy Motors.** Motor Modeling. 2012.

76. *Calculation of the airgap flux density of PM synchronous motors with buried magnets*

including axial leakage and teeth saturation. **Thelin, P and Nee, H-P.** Canterbury :

EMD, 1999. http://www.ee.kth.se/php/modules/publications/reports/1999/IR-EE-

EME_1999_009.pdf.

77. **The Mathworks.** TriScatteredInterp. *MathWorks Documentation Center.* [Online]

The Mathworks, 2012.

http://www.mathworks.com/help/matlab/ref/triscatteredinterp.html.

78. *MOdeling of a Urea SCR Catalyst with Automotive Applications.* **Upadhyay, Devesh and Nieuwstadt, Michiel.** s.l. : ASME, 2002.

79. **Department of Chemistry The University of North Carolina at Chapel Hill.** The Arrhenius equation. *Schodor.* [Online] Schodor, 2008.

http://www.shodor.org/unchem/advanced/kin/arrhenius.html.

80. **iSixSigma.** DFMEA. *iSixSigma.* [Online]

http://www.isixsigma.com/dictionary/dfmea/.

81. *Fault Tree Analysis- A History.* **Clifton, Ericson.** s.l. : International Systems Safety Conference, 1999.

82. **Department of Defense.** *Proceduers forPErforming a Failure Mode Effects and Criticality Analysis.* Washington D.C. : DOD, 1998. MIL-STD-1629A.

83. **Remy.** HVH 250. *Remy HVH 250.* 20112.

84. **The Mathworks.** PID. *Matlab.* [Online] The Mathworks, 2012.

http://www.mathworks.com/help/simulink/slref/pidcontroller.html.

85. **Smith, Steven.** *The Scientist and Engineer's Guide to Digital Signal Processing.* 1997.

86. *Bang-bang controller suing pulse-duration modulatino to provide a central linear region.* **Atkinson, P, Daey, R.L. and Fellgett.** s.l. : IEEE. Volume 4 Issue 6.

87. *Modeling of a Urea SCR Catalyst with Automotive Applications.* **Nieuwstadt, Van and Upadhyay, D.** New Orleans : ASME International Mechanical Engineering Congress and Exposition, 2002. IMECE2002-32104.

88. *A Survey on Electric/Hybrid Vehicles.* **Ribeiro, Bernardo, Brito, Francisco and Martins, Jorge.** s.l. : SAE International, 2010. 2010-01-0856.

89. *Comparison of Powertrain Configuration for Plug-in HEV's From a Fuel Economy Perspective.* **Freyermuth, Vincent, Fallas, ERic and Rousseau, Aymeric.** s.l. : SAE International, 2008. 2008-01-0461.